MATHEMATICAL MODELING OF COUPLED ION AND WATER TRANSPORT IN BIOLOGICAL TISSUES

YI ZHU

A DISSERTATION SUBMITTED TO THE FACULTY OF GRADUATE STUDIES
IN PARTIAL FULFILMENT OF THE REQUIREMENTS
FOR THE DEGREE OF
DOCTOR OF PHILOSOPHY

GRADUATE PROGRAM IN MATHEMATICS AND STATISTICS
YORK UNIVERSITY
TORONTO, ONTARIO

JULY 2021

Abstract

The coupling of ion and water transport has been recognized as an important subject of research in modern physiology, but much less attention has been paid to its mathematical modelling and analysis. In this thesis, we focus on mathematical modelling of the coupled ion and water transport in the lens of the eye and optic nerve. The choice of these two important parts of the vision system is made based on the fact that their physiology has been well studied and there is a large amount of experimental data.

For the lens of the eye, we introduce a general non-electroneutral (full) model to study microcirculation in the lens driven by its flows through ion channels and transporters. Through the numerical simulations, we show the full model can match with the experiment studying the effect of connexins on hydrostatic pressure very well. Furthermore, we obtain a simplified model based on physiological data and compare results with those in the literature. The simplified model can be reduced further to the first-generation models and provides a good approximation of the full model with a deeper understanding of the physiological process.

For optic nerve, our research focuses on potassium clearance in the narrow extracellular space outside nerve cells, a classical subject of biophysics research. Through a tridomain mathematical model, we capture general properties by which the central nervous system controls potassium concentration in the narrow extracellular space. We calibrate our full model (including water) with experiments in the literature and compare our full model with the corresponding electro-diffusion (without water) model. We explore how the magnitude of potassium clearance changes during and after neural stimulation and how the water flow generated by osmosis plays an important role in glial buffering.

Acknowledgements

I would like to express my sincere gratitude to my supervisor, Professor Huaxiong Huang, for his patience, guidance, and support during my Ph.D. study. Through numerous weekly meetings and discussions, Professor Huang has taught and shown me a systematic way to conduct interdisciplinary research. I have learned a lot from him about a complete applied mathematician.

I am very grateful for the guidance and assistance from Professor Bob Eisenberg at Rush University. His pioneer work on the electric property of lens has been the inspiration and guidance for my thesis research and my overall thinking in the subject area. His enthusiasm and knowledge have introduced me to modern physiology and bio-mathematical modeling.

I appreciate very much Professor Shixin Xu at Duke Kunshan University for continuing discussions and support. His knowledge in the subject areas and his dedication to research has influenced me significantly.

I also want to thank Professor Liu Chun at the Illinois Institute of Technology (IIT) for funding my conference trips to Banff, and for inviting and hosting my visit to IIT when I benefited a lot from discussions with him closely. I would also like to thank Dr. Xiulei Cao and Professor Zilong Song, for many fruitful discussions and advice.

Table of Contents

List of Tables

List of Figures

Chapter 1

Introduction

1.1 Lens of the eye: an overview

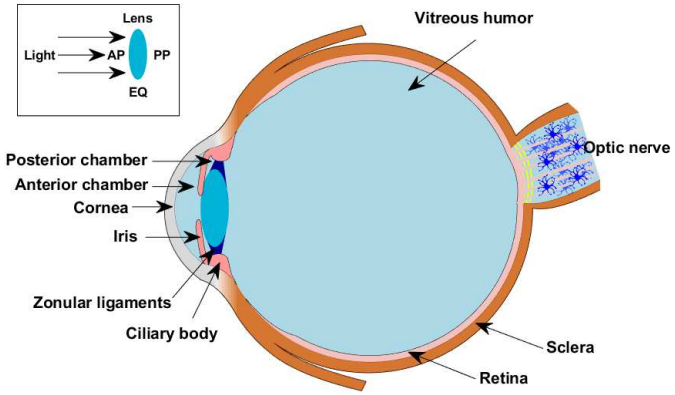

Figure 1.1: Schematic figure of eye showing its main components.

The lens of the eye is located behind the iris and suspended between the aqueous humor and vitreous humor by the zonular ligaments (see Figure 1.1). The lens consists of two types of cells: epithelial cells and fiber cells. On the lens's anterior surface is a layer of the epithelial cells. The epithelial cells differentiate into fiber cells at the equator of the lens (EQ) and the fiber cells are elongated towards the anterior pole (AP) and posterior pole (PP) of the lens as shown in Figure 1.2a. Fiber cells are tightly packed with very narrow extracellular space and filled with high concentrations of crystallin proteins. During the differentiation of fiber cells, nuclei and other major organelles gradually disappear, so that the mature lens fibers in the central region of the lens do not have organelles or nuclei [7, 8].

The lens of the eye is an asymmetrical electrical syncytium in which all fiber cells are electrically coupled one to another. At the same time, the lens is also a special syncytial tissue that contains no blood vessels. Usually, the circulatory system of blood vessels continuously

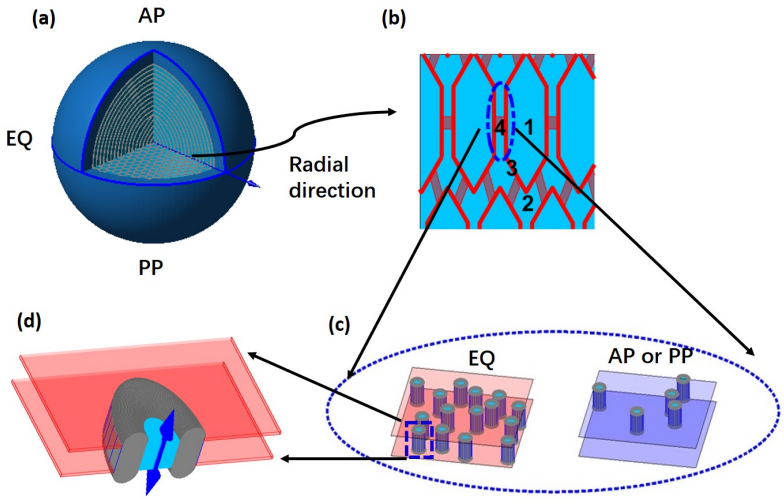

Figure 1.2: Schematic figure of the lens. a: the sphere of the lens with three landmarks: anterior pole (AP), posterior pole (PP), and the equator (EQ); b: the microstructure of the lens: 1. intracellular region 2. extracellular region 3. cell membrane 4. gap junctions (connexins); c: distribution of the gap junctions between the cell membrane at EQ or AP and PP; d: a single gap junction which allows water flow and ions to flow.

carries a supply of energy and inputs of mass into the tissues where the flow to and across cell membranes by diffusion is adequate. Nevertheless, in the lens, even small capillaries can seriously interfere with its transparency. It is well-known that age-related diseases, such as cataracts, are due to insufficient nutrients supply to repair oxidative damage in the cells and the oxidative damage leads to the lens's opacification [9, 10].

1.2 Optic nerve: an overview

The optic nerve belongs to the central nervous system (CNS) and it is divided into four main regions [11, 12]: (1) the intraocular nerve head, (2) the intraorbital region, (3) the intracanalicular, and (4) intracranial. This thesis focuses on the intraorbital region, which occupies more than half of the optic nerve.

In the optic nerve, glial cells wrap around bundles of nerve fiber, producing a narrow cleft of extracellular space between the nerve fibers and glia (see Figure 1.3b). Sometimes the central retinal blood vessels are found in the optic nerve bundle center in the intraorbital region. Here we consider a case where blood vessels are not present, as in the optic nerve of mud puppy, an amphibian salamander Necturus used in the experiments of Orkand et al. [4, 13]. Glial cells are connected through connexin proteins and form an electrical syncytium, in which the current flow in one cell spreads into another with little additional resistance.

The optic nerve is surrounded by the meningeal sheath, which consists of dura mater, arachnoid mater and pia mater, and cerebrospinal fluid (CSF) in the subarachnoid space

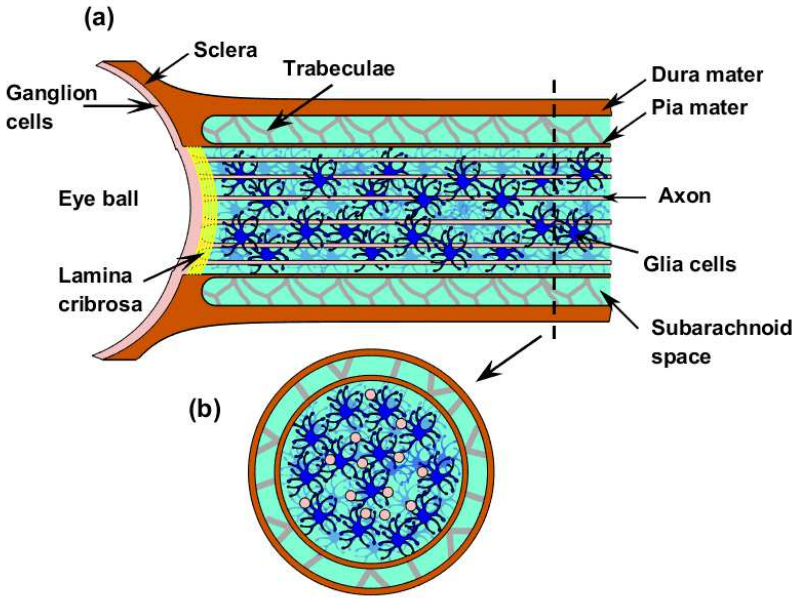

Figure 1.3: Optic nerve structure. a: Key features of the optic nerve region and subarachnoid space (SAS); b: Cross-section of the optic nerve.

(SAS) [12, 14] (see Figure 1.3a). The dura mater contains lymphatic vessels that drain CSF from the SAS (see [15, 16, 17, 18]) and the pia mater forms a macroscopic semipermeable membrane, consisting of many cells. Filipidis et.al.[19] have written a very useful review that identifies similar leptomeningeal structures important in physiology.

1.3 Research motivation

This thesis is inspired and motivated by experimental observations [3, 4, 13, 20, 21, 22]. With the developments of modern experimental studies, we have been able to gain a deeper understanding of the physiological properties of a biological system and the information required for mathematical modelling. Computable mathematical models are becoming a useful tool for understanding systems with complex structures studied in necessarily specialized experimental setups [23, 24]. The models help develop understanding of the biophysical underpinnings of function.

In our first case study, the lens of the eye has an avascular microcirculation to sufficiently deliver the nutrients to the center of the lens. The avascular microcirculation helps to maintain its well-organized structure, because the lens is a large organ, far beyond the length scale at which diffusion itself is efficient. Presumably, the avascular microcirculation is driven by an 'electro-osmotic pump' on its surface that generates water flow to carry nutrients into the lens and rinses wastes out of it. The lens modeling work is expected to help us to have better understand the physiological functions of the lens through its ion fluxes and water

transport. Through our study on the lens, we carefully validated that the fundamental field equations are consistent and appropriately approximated. This validated mathematical model provides a powerful tool to understand the general physiological properties of syncytial tissues (such as smooth muscle, glial cells, and the heart), which are large compared to most single cells, and connected in space [3].

Many other tissues have much more complex structures and are of clinical interest than the lens. As part of an extended study of the lens, we explore the optic nerve, a part of the central nervous system, to generalize our model and analyses. Experiments have been done on this well-defined system. The Kuffler group at Harvard [4, 13, 22] studied the optic nerve in some detail, looking at the potassium clearance in the narrow extracellular space and the effect of glia, following the pioneering work of Frankenhaeuser and Hodgkin [25]. The accumulation and clearance of potassium in the narrow space outside nerve cells is a classical subject of biophysics, to which much attention has been paid recently. The extraordinarily dense packing of neurons in the central nervous system raises questions about how the signal in one nerve fiber is kept separated from the signal in another, and how the central nervous system maintains concentrations in its narrow cleft between cells. The smooth signal processing function of the axon is highly dependent on the ion concentration in the extracellular space, especially on the potassium concentration. Because potassium in the extracellular space plays a vital role in modulating the resting membrane potential and the threshold and shape of action potentials [26, 27]. The clearance of potassium ions in the extracellular space is of great interest because several action potentials are likely to dramatically change the potassium concentration in this narrow extracellular space. If this excessive amount of potassium is not removed in a timely manner, it may lead to pathological conditions known as cortical spreading depolarization (CSD). Quantitative analysis is likely to help evaluate potassium clearance from the extracellular space after a train of action potentials. Recent experimental studies [28] suggest that transport in the central nervous system during sleep plays a critical role in maintaining the health of brain tissue.

1.4 Literature review

Early research and modelling focused primarily on the electrical properties of lens. An equivalent circuit model [20, 29] was introduced to study transportation of the ion fluxes in different electrical components. The electric field theory develops models considering the structure by analyzing the spectroscopic data of impedance measurements using field theory. It verifies that the parameters change appropriately when the composition and concentration of extracellular solutions change. These models provide fundamental support to the general understanding of syncytial tissues. Recently Mathias et al. [3, 30] combined the circuit model with fluid transport and proposed microcirculation in the lens. Following Mathias's pioneer work, many computational models in the lens were performed taking into account the angular circulation of ion and fluid in the lens [31, 32, 33]. It is assumed that the microcirculation system in the lens is generated by spatial differences of sodium-potassium

pump's distribution on the surface [34, 35] and the transport properties of the ion and water on the membrane. The simulation results show that the circulating sodium flux can form an osmotic gradient in the lens, which can generate water circulation [3, 29, 32]. In addition, there are various experimental confirmations of the fluid velocity on the surface of the lens [1, 36, 37, 38]. At the same time, the lens model was extended to simulate age-related changes in the lens and a variety of physiological processes [39, 40]. Reviews of current research on the microcirculation in the lens are most helpful [41, 42].

The lens of the eye has an essentially bidomain structure (intracellular and extracellular spaces), while the optic nerve (or more general regions of the central nervous system), contains nerve fibers and glia separated by a narrow extracellular space. Various mathematical models have been proposed for modelling the optic nerve [43, 44, 45]. Most of them are focused on the optic nerve head. Band et al. [46] proposed a mechanical model for the whole nerve fiber bundle, where only the water flow in the axon is considered. A cable-type model [47] focusing on the electrical properties of the optic nerve was presented in [48]. The interactions between neuronal cells and glial cells have been included in models of the important phenomenon of spreading depression [49, 50], which is widely believed to be associated with epilepsy and migraine. Some two-compartment models for potassium clearance (or spatial buffering) include interactions between neuronal cells and extracellular space [51] or interactions between glial cells and extracellular space [52, 53]. Sibille [54] introduced a three-compartment model of ordinary differential equations (ODEs) to study the role of K_{ir4} channels. This shows that water flows play an important role in the central nervous system [55] through the influx and efflux routes, helping to remove waste. Some models, including water flow but not electrodiffusion, were introduced to study the effect of pressure on the flow direction [18, 56]. Mori [57] proposed a multidomain model for cortical spreading depression, where ionic electrodiffusion and osmosis between different compartment are considered. We extend those results and present some general conclusions based on the analysis of a specific set of experiments (Orkand et al [4, 13]) using a model of ionic electrodiffusion and osmosis, which has proven to be quite helpful in dealing with the substantial literature on electrodiffusion of the lens of the eye [58].

1.5 Thesis outline

This thesis is organized as follows. In Chapter 2, we set up the fundamental field equations to the lens for its ion and water microcirculation. We show how the Mathias group's model can be extended to fit a wide range of experimental data. We also present a simplified model to reflect the most intrinsic underlying relations. Most of the material presented in Chapter 2 has been published in Biophysical Journal [58]. In Chapter 3, we extend our model to the optic nerve and adapt the work of the Harvard group [4]. In Chapter 4, we study water circulation in the optic nerve. We find that the water circulation generated by osmosis enhances potassium transport in the glial compartment compared to the electro-diffusion model. Most of the material presented in Chapter 3 and 4 has been published in Physics

of Fluids [59]. In Chapter 5, we study potassium clearance using various simulations by changing stimulus patterns for the axon. We find that both extracellular space and glial cells play important roles and we further study the effect of NKCC on the glial membrane and non-selective pathways on the pia boundary. Most of the material in Chapter 5 has been published in Biophysical Journal [60].

Chapter 2

Microcirculation in the lens

In this chapter, we introduce a coupled ion-water transport model (the full model) to study the microcirculation in the lens of the eye. The full model is introduced in Section 2.1. In Section 2.2, we obtain the leading order model by identifying small parameters in the full model. Based on boundary conditions and analysis based on the governing equations, a simplified version of the leading order model is proposed and compared with the existing model. In Section 2.3, the full model is calibrated by predicting the effects of gap junctions (connexins) in experiments [1, 2]. At the same time, our simplified model captures the main features of the full model and provides an explanation of simulation results on the effects of gap junctions.

2.1 Water circulation and ion transport in the lens

In this section, we propose a bidomain model with non-electroneutral condition to study the microcirculation of lens. In the literature, the most of lens research study [3, 31, 32, 33, 42] haven't included the effect of cell membrane into the models for the lens microcirculation. We include a capacitor in the representation of cell membrane and so our model is consistent with classical electrodynamics. This membrane capacitance is due to the fact that the plasma membrane acts as a capacitor: the lipid bilayer separates two electrolytic regions, the extracellular space and the intracellular space. In this way, it consistently produces a linear correction term in the classical charge neutrality equation.

The model deals with two types of flow: the circulation of water (hydrodynamics) and the circulation of ions (electrodynamics), generalizing previous bidomain models that deal only with electrodynamics. The model is derived by using the conservation laws of ions and water to consider the exchange between intracellular and extracellular spaces through cell membranes. We note that a similar approach is useful in other tissues with narrow extracellular space, such as the heart, cardiac muscle, and the central nervous system.

In the following, we first introduce the definition of the terms listed in the Glossary below, where $i = \mathrm{Na}^+, \mathrm{K}^+, \mathrm{Cl}^-$ for ion spices, $l = ex, in$ for extracellular and intracellular regions.

GLOSSARY

c_l^i: Ion i concentration in the l region,
ϕ_l: Electric potential in l region,
p_l: Hydrostatic pressure in l region,
η_{in}: Volume fraction of intracellular region,
O_l: Osmotic concentration in l region,
$\mathbf{u}_l$: Fluid velocity inside of the l region,
$\mathbf{j}_l^i$: Ion i flux inside of l region,
U_m: Fluid transmembrane velocity on cell membrane,
J_m^i: Ion i transmembrane flux on cell membrane,
J_s^i: Ion i transmembrane flux on surface membrane,
J_p^i: Na/K pump flux on surface membrane,
$I_{max,1}$: Max current of α_1- Na/K pump on surface,
$I_{max,2}$: Max current of α_2- Na/K pump on surface,
A_{in}: Negative charged protein density in intracellular region,
$\mathcal{M}_l$: Area ratio of l region,
$\mathcal{M}_v$: Membrane area in per unit control volume,
κ_l: Water permeability of l region,
μ: Fluid viscosity,
L_m: Hydrostatic permeability of cell membrane,
L_s: Hydrostatic permeability of surface membrane,
g^i: Conductance of cell membrane for ion i,
G^i: Conductance of surface membrane for ion i,
C_m: Cell membrane capacitance,
τ_{ex}: Tortuosity in extracellular region,
D_l^i: Diffusion coefficient of i ion in l region,
T: Temperature,
k_B: Boltzmann constant,
e: Electron charge,
z^i: Valence of the ion i.

Water circulation

We make the following assumptions for the water circulation

- the loss or gain of intracellular water is only through cell membranes flowing into the extracellular space, vice versa [20].
- the transmembrane water flux is proportional to the intracellular/extracellular hydrostatic pressure and osmotic pressure differences, i.e., Starling's law on the membrane [61]. In a system like non-ideal ionic solutions in which, 'everything interacts with everything else' [62, 63], this statement needs derivation as well as an assertion. A complete and rigorous derivation can be found in [64].

Then we obtain the following system for intracellular and extracellular velocities in domain $\Omega = [0, R]$

$$\frac{1}{r^2}\frac{d}{dr}\left(r^2\mathcal{M}_{ex}u_{ex}\right) = \mathcal{M}_v U_m, \tag{2.1a}$$

$$\frac{1}{r^2}\frac{d}{dr}\left(r^2(\mathcal{M}_{ex}u_{ex} + \mathcal{M}_{in}u_{in})\right) = 0, \tag{2.1b}$$

where u_l with $l = in, ex$ is the velocity in the intracellular space and extracellular space, respectively. The transmembrane velocity U_m is defined as

$$U_m = L_m\left(p_{in} - p_{ex} + \gamma_m k_B T\left(O_{ex} - O_{in}\right)\right),$$

where the p_l and O_l, with $l = in, ex$, are the hydrostatic pressure and the molar concentration of solute with definition

$$O_{ex} = \sum_i c_{ex}^i, \qquad O_{in} = \sum_i c_{in}^i + A_{in}.$$

The c_l^i is the concentration of ith ion species in l space and A_{in} is the density of the permanent negatively charged protein in the intracellular space. In this work, we assume the permanent negatively charged protein is uniformly distributed within the intracellular space with valence of z^{in}.

Here $\mathcal{M}_l$ is the ratio of intracellular area ($l = in$) and extracellular area ($l = ex$), $\mathcal{M}_v$ is the cell membrane area per volume unit, γ_m is the cell membrane reflectance, a ratio between the observed osmotic pressure and theoretical osmotic pressure, inside of the lens. L_m is the cell membrane hydraulic permeability inside of the lens, k_B is Boltzmann constant and T is temperature.

As we mentioned before, the intracellular space is a connected space, where water can flow from cell to cell through connexins on the membranes between cells, and the extracellular space is narrow with a high tortuosity. The intracellular velocity depends on the gradients of hydrostatic pressure and osmotic pressure [3, 32, 64], and the extracellular velocity is determined by the gradients of hydrostatic pressure and electric potential [32, 65],

$$u_{ex} = -\frac{\kappa_{ex}}{\mu}\tau_{ex}\frac{d}{dr}p_{ex} - k_e\tau_{ex}\frac{d}{dr}\phi_{ex}, \tag{2.2a}$$

$$u_{in} = -\frac{\kappa_{in}}{\mu}\left(\frac{d}{dr}p_{in} - \gamma_m k_B T\frac{d}{dr}O_{in}\right), \tag{2.2b}$$

where ϕ_l is the electric potential in the l space, τ_{ex} is the tortuosity of extracellular region and μ is the viscosity of water, k_e is introduced to describe the effect of electro-osmotic flow, κ_l is the permeability of intracellular space ($l = in$) and extracellular space ($l = ex$), respectively.

By using Equation (2.2), Equation (2.1) is treated as the equation of hydraulic pressure. Due to the axis symmetry condition, homogeneous Neumann boundary conditions are used for hydrostatic pressure at $r = 0$. At the surface of lens ($r = R$), we set the extracellular hydrostatic pressure to be zero, and the intracellular velocity is consistent with Equation (2.2)

$$\begin{cases} \dfrac{\partial p_{ex}}{\partial r} = \dfrac{\partial p_{in}}{\partial r} = 0, & \text{at } r = 0, \\ p_{ex} = 0, & \text{at } r = R, \\ -\dfrac{\kappa_{in}}{\mu}\left(\dfrac{d}{dr}p_{in} - \gamma_m k_B T\dfrac{d}{dr}O_{in}\right) = L_s\left(p_{in} - p_{ex} - \gamma_s k_B T\left(O_{in} - O_{ex}\right)\right), & \text{at } r = R, \end{cases} \tag{2.3}$$

where γ_s and L_s are the membrane reflectance and membrane hydraulic permeability at the surface of the lens, respectively.

Ion transport

In this work, we consider three types of ions: Na^+, K^+ and Cl^-. With similar assumptions, the conservation of ions yields the following ion flux system for $i = Na^+, K^+, Cl^-$

$$\frac{1}{r^2}\frac{d}{dr}(r^2\mathcal{M}_{ex}j^i_{ex}) = \mathcal{M}_v J^i_m, \tag{2.4a}$$

$$\frac{1}{r^2}\frac{d}{dr}(r^2(\mathcal{M}_{ex}j^i_{ex} + \mathcal{M}_{in}j^i_{in})) = 0. \tag{2.4b}$$

For the ith ion species, its intracellular flux j^i_{in} and extracellular flux j^i_{ex} are defined as follows

$$j^i_{ex} = c^i_{ex}u_{ex} - D^i_{ex}\tau_{ex}\frac{d}{dr}c^i_{ex} - D^i_{ex}\tau_{ex}\frac{z^i e}{k_B T}c^i_{ex}\frac{d}{dr}\phi_{ex}, \tag{2.5a}$$

$$j^i_{in} = c^i_{in}u_{in} - D^i_{in}\frac{d}{dr}c^i_{in} - D^i_{in}\frac{z^i e}{k_B T}c^i_{in}\frac{d}{dr}\phi_{in}, \tag{2.5b}$$

where D^i_l is the diffusion coefficient of the ith ion species in the l space. The conductance formulation is used to describe the transmembrane flux of ions across the membrane inside of the lens and the surface membrane of the lens as

$$J^i_m = \frac{g^i}{z^i e}\left(\phi_{in} - \phi_{ex} - E^i\right), \tag{2.6a}$$

$$J^i_s = \frac{G^i}{z^i e}\left(\phi_{in} - \phi_{ex} - E^i\right), \tag{2.6b}$$

where $E^i = \frac{k_B T}{z^i e}\log\left(\frac{c^i_{ex}}{c^i_{in}}\right)$ is the Nernst potential (an expression of the difference of chemical potential) of ith ion species.

In Equation (2.6), the ion conductance g^i and surface ion conductance G^i depends on the ion channel distribution in the membrane (see Figure 2.1). Based on previous work [3, 20, 32], we assume that

- Na^+ and Cl^- can leak between intracellular and extracellular regions through ion channels in the membrane inside of the lens,
- there is no transmembrane flux for K^+ between the extracellular and intracellular regions inside of the lens, i.e., $J^K_m = 0$.

For ion concentration system, similar to the hydrostatic pressure, homogeneous Neumann boundary conditions are used at $r = 0$. At the surface of the lens ($r = R$), the extracellular concentrations are fixed, and Robin boundary conditions are used for intracellular concentrations due to the transmembrane flux through the passive ion channel and active ion pump,

$$\begin{cases} \dfrac{\partial c^i_{ex}}{\partial r} = \dfrac{\partial c^i_{in}}{\partial r} = 0, & \text{at } r = 0, \\ c^i_{ex} = c^i_o, & \text{at } r = R, \\ j^i_{in} = J^i_s + J^i_p, & \text{at } r = R, \end{cases} \tag{2.7}$$

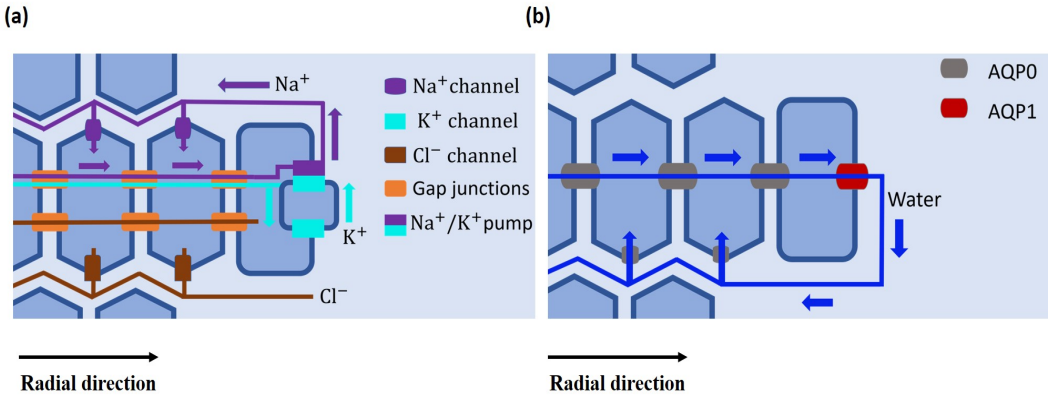

Figure 2.1: a: Schematic diagram of ion circulation and distributions of ion channels and pumps in the lens. The purple line represents the Na^+ flow, the light green represents the K^+ flow, and the brown line represents Cl^- flow. The surface epithelial cells (square) connect with the intracellular cells (hexagon) by the gap junctions (orange rectangle). Na^+ and Cl^- ion channels are located on the intercellular membrane, while the K^+ ion channel and Na/K pumps distribute only on the surface membrane. b: Schematic diagram of water circulation. Transmembrane water transport is through AQP0 and AQP1 gap junctions. APQ0 gap junctions are located at the intercellular membrane, and AQP1 is at the surface membrane.

where J_p^i is the active ion pump flux on the surface membrane of the lens. Here we only consider the Na/K pump on the surface membrane and the strength of the pump depends on the ion's concentration as in [32, 34],

$$J_p^{Na} = 3\frac{I_p}{e}, \quad J_p^K = -2\frac{I_p}{e}, \quad J_p^{Cl} = 0, \tag{2.8}$$

where

$$I_p = I_{max,1}\left(\frac{c_{in}^{Na}}{c_{in}^{Na}+K_{Na1}}\right)^3\left(\frac{c_o^K}{c_o^K+K_{K1}}\right)^2 + I_{max,2}\left(\frac{c_{in}^{Na}}{c_{in}^{Na}+K_{Na2}}\right)^3\left(\frac{c_o^K}{c_o^K+K_{K2}}\right)^2. \tag{2.9}$$

Due to the capacitance of cell membrane, we introduce a linear correction term [66, 57] instead of the charge neutrality condition in [3, 32] as

$$(1-\eta_{in})\left(\sum_i z^i e c_{ex}^i\right) = -\mathcal{M}_v C_m\left(\phi_{in}-\phi_{ex}\right), \tag{2.10a}$$

$$\eta_{in}\left(\sum_i z^i e c_{in}^i + z^{in} e A_{in}\right) = \mathcal{M}_v C_m\left(\phi_{in}-\phi_{ex}\right), \tag{2.10b}$$

where η_{in} is the porosity of the intracellular region and C_m is the capacitance per unit area. Multiplying each ion concentration equation in Equation (2.4) with $z^i e$ respectively, summing

up and using Equation (2.10), we have the following governing equations for ϕ_{ex} and ϕ_{in}

$$\frac{1}{r^2}\frac{d}{dr}\left(r^2\mathcal{M}_{ex}\left(\rho_{ex}u_{ex} - e\tau_{ex}\sum_i D^i_{ex}z^i\frac{d}{dr}c^i_{ex} - \sigma_{ex}\frac{d}{dr}\phi_{ex}\right)\right)$$
$$= \mathcal{M}_v\left(g^m\left(\phi_{in}-\phi_{ex}\right) - \sum_i g^i E^i\right), \tag{2.11a}$$

$$\frac{1}{r^2}\frac{d}{dr}\left(r^2\mathcal{M}_{in}\left(\rho_{in}u_{in} - e\sum_i D^i_{in}z^i\frac{d}{dr}c^i_{in} - \sigma_{in}\frac{d}{dr}\phi_{in}\right)\right)$$
$$= -\mathcal{M}_v\left(g^m\left(\phi_{in}-\phi_{ex}\right) - \sum_i g^i E^i\right), \tag{2.11b}$$

with boundary conditions

$$\begin{cases} \dfrac{d\phi_{ex}}{dr} = \dfrac{d\phi_{in}}{dr} = 0, & \text{at } r = 0, \\ \phi_{ex} = 0, & \text{at } r = R, \\ \rho_{in}u_{in} - e\displaystyle\sum_i D^i_{in}z^i\frac{d}{dr}c^i_{in} - \sigma_{in}\frac{d}{dr}\phi_{in} = G^s\phi_{in} - \sum_i G^i E^i + I^\phi_p, & \text{at } r = R, \end{cases}$$

where $\rho_{in} = \frac{\mathcal{M}_v C_m}{\eta_{in}}\left(\phi_{in}-\phi_{ex}\right) + e|z^{in}|A_{in}$ and $\rho_{ex} = \frac{\mathcal{M}_v C_m}{1-\eta_{in}}\left(\phi_{ex}-\phi_{in}\right)$,

$$g^m = \sum_i g^i, \quad G^s = \sum_i G^i, \quad I^\phi_p = e\sum_i z^i J^i_p.$$

In Equation (2.11), we define the intracellular conductance σ_{in} and extracellular conductance σ_{ex} as

$$\sigma_{ex} = \frac{\tau_{ex}e^2}{k_B T}\left(\sum_i D^i_{ex}(z^i)^2 c^i_{ex}\right), \quad \sigma_{in} = \frac{e^2}{k_B T}\left(\sum_i D^i_{in}(z^i)^2 c^i_{in}\right).$$

It is obvious that system (2.11) derived using Equation (2.4) and Equation (2.10). Therefore, we should drop one of the ion governing equation in Equation (2.4).

Non-dimensionalization

The Na/K pump distributed at the lens's surface serves as an osmotic device. It is the main driving force for the ion and water circulation in the lens. We choose the characteristic scale of velocity u^*_{in} related to the Na/K pump strength J^{Na*}_p at the surface of the lens (see Appendix A.1) as

$$u^*_{in} = \frac{J^{Na*}_p}{O^*}. \tag{2.12}$$

where $O^* = 2\left(c_o^{Na} + c_o^K\right)$ is the characteristic osmosis scale. Using Equation (2.1b), we obtain the scale of extracellular velocity u_{ex} as

$$u_{ex}^* = \delta_0^{-1} u_{in}^*, \tag{2.13}$$

where $\delta_0 = \frac{\mathcal{M}_{ex}}{\mathcal{M}_{in}}$.
With the characteristic scales for electric potential ϕ_l, hydrostatic pressure p_l and concentration c_l^i chosen as $\frac{k_B T}{e}$, $\frac{\mu R u_{ex}^*}{\kappa_{ex}\tau_{ex}}$ and $c_o^{Na} + c_o^K$, we obtain the dimensionless system for lens problem as follows (the detailed derivation is given in Appendix A.1)

$$u_{ex} = -\frac{d}{dr}p_{ex} - \delta_1 \frac{d}{dr}\phi_{ex}, \tag{2.14a}$$

$$\delta_2 u_{in} = -\delta_3 \frac{d}{dr}p_{in} + \frac{d}{dr}O_{in}, \tag{2.14b}$$

$$\delta_4 \frac{1}{r^2}\frac{d}{dr}\left(r^2 u_{in}\right) = \delta_3\left(p_{ex} - p_{in}\right) + \left(O_{in} - O_{ex}\right), \tag{2.14c}$$

$$u_{ex} = -u_{in}, \tag{2.14d}$$

$$\sum_i z^i c_{in}^i + z^{in} A_{in} = \delta_6\left(\phi_{in} - \phi_{ex}\right), \tag{2.14e}$$

$$\sum_i z^i c_{ex}^i = -\delta_7\left(\phi_{in} - \phi_{ex}\right), \tag{2.14f}$$

$$\frac{1}{r^2}\frac{d}{dr}\left(r^2 j_{ex}^{Cl}\right) = \frac{\mathcal{M}_v^{ex}}{z^{Cl}}\left(\phi_{in} - \phi_{ex} - E^{Cl}\right), \tag{2.14g}$$

$$\frac{1}{r^2}\frac{d}{dr}\left(r^2 j_{in}^{Cl}\right) = -\frac{\delta_8}{r^2}\frac{d}{dr}\left(r^2 j_{ex}^{Cl}\right), \tag{2.14h}$$

$$\frac{1}{r^2}\frac{d}{dr}\left(r^2 j_{ex}^{K}\right) = 0, \tag{2.14i}$$

$$\frac{1}{r^2}\frac{d}{dr}\left(r^2 j_{in}^{K}\right) = 0, \tag{2.14j}$$

$$\begin{aligned}&\frac{1}{r^2}\frac{d}{dr}\left(r^2\left(Pe_{ex}\rho_{ex}u_{ex} - \sum_i D_{ex}^i z^i \frac{d}{dr}c_{ex}^i - \sigma_{ex}\frac{d}{dr}\phi_{ex}\right)\right)\\ &= \mathcal{M}_v^{ex}\left(2\left(\phi_{in} - \phi_{ex}\right) - E^{Na} - E^{Cl}\right),\end{aligned} \tag{2.14k}$$

$$\begin{aligned}&\frac{1}{r^2}\frac{d}{dr}\left(r^2\left(Pe_{in}\rho_{in}u_{in} - \sum_i D_{in}^i z^i \frac{d}{dr}c_{in}^i - \sigma_{in}\frac{d}{dr}\phi_{in}\right)\right)\\ &= -\frac{\delta_8}{r^2}\frac{d}{dr}\left(r^2\left(Pe_{ex}\rho_{ex}u_{ex} - \sum_i D_{ex}^i z^i \frac{d}{dr}c_{ex}^i - \sigma_{ex}\frac{d}{dr}\phi_{ex}\right)\right).\end{aligned} \tag{2.14l}$$

In System (2.14), Equations (2.14k) and (2.14l) have already incorporated the governing equation of Na^+ by using Equations (2.14e) and (2.14f). For the boundary conditions of System (2.14), we propose homogeneous Neumann boundary conditions at $r = 0$ and follow-

ing boundary conditions at $r = 1$

$$\begin{cases} p_{ex} = 0, \\ \delta_5 u_{in} = \delta_3 p_{in} - (O_{in} - O_{ex}), \\ c_{ex}^K = c_o^K, \\ j_{in}^K = \dfrac{R_s}{z^K}\left(\phi_{in} - E^K\right) + J_p^K, \\ c_{ex}^{Cl} = c_o^{Na} + c_o^K + \delta_7\left(\phi_{in} - \phi_{ex}\right), \\ j_{in}^{Cl} = 0, \\ \phi_{ex} = 0, \\ Pe_{in}\rho_{in}u_{in} - \displaystyle\sum_i D_{in}^i z^i \frac{d}{dr} c_{in}^i - \sigma_{in}\frac{d}{dr}\phi_{in} = R_s\left(\phi_{in} - E^K\right) + I_p^\phi, \end{cases} \tag{2.15}$$

where

$$\begin{aligned} &\rho_{in} = \rho_0 + \delta_6\left(\phi_{in} - \phi_{ex}\right), && \rho_{ex} = \delta_7\left(\phi_{ex} - \phi_{in}\right), \\ &\rho_0 = |z^{in}|A_{in}, && \sigma_l = \sum_i D_l^i (z^i)^2 c_l^i, \\ &E^i = \frac{1}{z^i}\log\left(\frac{c_{ex}^i}{c_{in}^i}\right), && I_p^\phi = \frac{I_p R}{e D_{in}^* c^*}, \\ &j_l^i = Pe_l c_l^i u_l - D_l^i\left(\frac{d}{dr}c_l^i + z^i c_l^i \frac{d}{dr}\phi_l\right), && J_p^K = \frac{J_p^K R}{D_{in}^* c^*}, \\ &R_s = \frac{G^K k_B T R}{e^2 D_{in}^* c^*}, \end{aligned}$$

with $i = \mathrm{Na}^+, \mathrm{K}^+, \mathrm{Cl}^-,\ l = in, ex.$

2.2 Simplified model

System (2.14) with boundary conditions (2.15) is a coupled nonlinear system. In this section, we would like to present a simplified version of the full model, which could also capture the main feature of the lens circulation. We first obtain the leading order model by identifying the small parameters in the non-dimensionalization system. And then, by using boundary conditions and theoretical analysis, the leading order model is further simplified to only one PDE along with several algebraic equations.

According to those dimensionless parameters presented in Appendix A.4, we identify the scale of the parameters as follows.

$$\begin{aligned} &\{\delta_1, \delta_8\} \subset O(\epsilon), \quad \{\delta_0, \delta_3\} \subset O(\epsilon^2), \\ &\{\delta_2, \delta_4, \delta_5, \delta_6, \delta_7\} \subset o(\epsilon^2). \end{aligned} \tag{2.16}$$

If we denote $\delta_9 = D_l^{Cl} - D_l^K$ and $\delta_{10} = D_l^{Cl} - D_l^{Na}$, $l = in, ex$, it yields

$$\delta_9 = O(\epsilon^2), \quad \delta_{10} = O(\epsilon). \tag{2.17}$$

In domain $\Omega = [0, 1]$, the leading order approximation of system (2.14)-(2.15) is given by (see Appendix A.2)

$$u_{ex}^0 = -\frac{d}{dr} p_{ex}^0 - \delta_1 \frac{d}{dr} \phi_{ex}^0, \tag{2.18a}$$

$$\frac{d}{dr} O_{in}^0 = 0, \tag{2.18b}$$

$$O_{in}^0 - O_{ex}^0 = 0, \tag{2.18c}$$

$$u_{ex}^0 = -u_{in}^0, \tag{2.18d}$$

$$\sum_i z^i c_{in}^{i,0} + z^{in} A_{in} = 0, \tag{2.18e}$$

$$\sum_i z^i c_{ex}^{i,0} = 0, \tag{2.18f}$$

$$\frac{1}{r^2} \frac{d}{dr} \left(r^2 j_{in}^{K,0} \right) = 0, \tag{2.18g}$$

$$\frac{1}{r^2} \frac{d}{dr} \left(r^2 j_{ex}^{K,0} \right) = 0, \tag{2.18h}$$

$$\frac{1}{r^2} \frac{d}{dr} \left(r^2 j_{ex}^{Cl,0} \right) = \frac{\mathcal{M}_v^{ex}}{z^{Cl}} \left(\phi_{in}^0 - \phi_{ex}^0 - E^{Cl,0} \right), \tag{2.18i}$$

$$\frac{1}{r^2} \frac{d}{dr} \left(r^2 j_{in}^{Cl,0} \right) = -\frac{\delta_8}{r^2} \frac{d}{dr} \left(r^2 j_{ex}^{Cl,0} \right), \tag{2.18j}$$

$$\frac{d}{dr} \phi_{in}^0 = \frac{Pe_{in} \rho_0}{\sigma_{in}^0} u_{in}^0 - \frac{\delta_8 \sigma_{ex}^0}{\sigma_{in}^0} \frac{d}{dr} \phi_{ex}^0, \tag{2.18k}$$

$$-\frac{1}{r^2} \frac{d}{dr} \left(r^2 \left(\delta_{10} \frac{d}{dr} c_{ex}^{Na,0} + \sigma_{ex}^0 \frac{d}{dr} \phi_{ex}^0 \right) \right) = \mathcal{M}_v^{ex} \left(2 \left(\phi_{in}^0 - \phi_{ex}^0 \right) - E^{Na,0} - E^{Cl,0} \right), \tag{2.18l}$$

with homogeneous Neumann boundary conditions at $r = 0$ and boundary conditions at $r = 1$ as

$$\begin{cases} p_{ex}^0 = 0, \\ c_{ex}^{Cl,0} = c_o^{Na} + c_o^K, \\ c_{ex}^{K,0} = c_o^K, \\ j_{in}^{K,0} = \dfrac{R_s}{z^K} \left(\phi_{in}^0 - E^{K,0} \right) + J_p^K, \\ Pe_{in} \rho_0 u_{in}^0 + \delta_{10} \dfrac{d}{dr} c_{in}^{Na,0} - \sigma_{in} \dfrac{d}{dr} \phi_{in}^0 = R_s \left(\phi_{in}^0 - E^{K,0} \right) + I_p^\phi, \\ \phi_{ex}^0 = 0. \end{cases} \tag{2.19}$$

In the following, we will further simplify Equations (2.18) - (2.19) and obtain the relationships between ϕ_{ex}^0 and other leading order variables by using assumptions concerning the boundary conditions.

Relation between ϕ_{in}^0 and ϕ_{ex}^0

By using Equation (2.18a) and Equation (2.18d), integrating Equation (2.18k) over the domain $[r, 1]$ yields the relation among ϕ_{in}^0, ϕ_{ex}^0 and p_{ex}^0 in $\Omega = [0, 1]$,as

$$\phi_{in}^0(r) = \left(\frac{Pe_{in}\rho_0\delta_1}{\sigma_{in}^0} - \frac{\delta_8\sigma_{ex}^0}{\sigma_{in}^0} \right) \phi_{ex}^0(r) + \frac{Pe_{in}\rho_0}{\sigma_{in}^0} p_{ex}^0(r) + \phi_{in}^0(1), \tag{2.20}$$

where we used the boundary conditions $\phi_{ex}^0(1) = p_{ex}^0(1) = 0$.

Relation between p_{ex}^0 and ϕ_{ex}^0

By the homogeneous Neumann boundary condition on $r = 0$ for $c_l^{Cl,0}$ in both intracellular ($l = in$) and extracellular ($l = ex$) space and Equation (2.18j), we have the following Cl^- flux relation in domain $\Omega = [0, 1]$

$$j_{in}^{Cl,0} + \delta_8 j_{ex}^{Cl,0} = 0. \tag{2.21}$$

By divided $c_{ex}^{Cl,0}$ in both side in Equation (2.21) and using Equation (A.34b), we obtain

$$\left(Pe_{in} \frac{c_{in}^{Cl,0}}{c_{ex}^{Cl,0}} u_{in}^0 - D_{in}^{Cl} z^{Cl} \frac{c_{in}^{Cl,0}}{c_{ex}^{Cl,0}} \frac{d\phi_{in}^0}{dr} \right) + \delta_8 \left(Pe_{ex} u_{ex}^0 - D_{ex}^{Cl} z^{Cl} \frac{d\phi_{ex}^0}{dr} \right) = 0. \tag{2.22}$$

Based on the charge neutrality Equation (A.33) and parameters in Appendix A.4, we denote δ_{11} as

$$\delta_{11} = \frac{c_{in}^{Cl,0}}{c_{ex}^{Cl,0}} = \frac{c_o^{Na} + c_o^K - \frac{1+|z^{in}|}{2} A_{in}}{c_o^{Cl,0}} = O(\epsilon). \tag{2.23}$$

Then combining Equation (2.23), Equation (A.40) and the fact that $Pe_{in} = O(\epsilon)$, Equation (2.22) yields the following equation by omitting the higher order terms

$$Pe_{ex} u_{ex}^0 + D_{ex}^{Cl} \frac{d\phi_{ex}^0}{dr} = 0. \tag{2.24}$$

Finally, by integrating Equation (2.24) over $[0, r]$ and using the homogeneous Neumann boundary condition for the hydrostatic pressure p_{ex}^0 on $r = 0$, we obtain the relation between leading order of extracellular pressure (p_{ex}^0) and electric potential (ϕ_{ex}^0) in Ω as

$$p_{ex}^0 = \frac{D_{ex}^{Cl} - Pe_{ex}\delta_1}{Pe_{ex}} \phi_{ex}^0. \tag{2.25}$$

Expression of E^{Na}

Based on potassium equation in Equation (2.18g)-(2.18h) and corresponding boundary conditions, combining the relations in Equation (2.20) and Equation (2.25), we have expressions for c_{in}^K and c_{ex}^K in domain Ω as

$$c_{ex}^{K,0} = c_o^K \exp\left(-\left(1+\frac{D_{ex}^{Cl}}{D_{ex}^K}\right)\phi_{ex}^0\right), \tag{2.26a}$$

$$c_{in}^{K,0} = c_{in}^{K,0}(1)\exp\left(\left(\frac{Pe_{in}D_{ex}^{Cl}}{Pe_{ex}D_{in}^K} - \frac{Pe_{in}D_{ex}^{Cl}\rho_0}{Pe_{ex}\sigma_{in}^0}\right)\phi_{ex}^0\right)\exp\left(\left(\frac{\delta_9\sigma_{ex}^0}{\sigma_{in}^0}\right)\phi_{ex}^0\right), \tag{2.26b}$$

where

$$c_{in}^{K,0}(1) = c_o^{K,0}\exp\left(-\frac{J_p^K}{R_s} - \phi_{in}(1)\right). \tag{2.27}$$

In addition, based on the charge neutrality Equation (A.33), we can write the leading order of the Na^+ Nernst potential in the domain Ω as

$$E^{Na,0} = \frac{1}{z^{Na}}\log\left(\frac{c_{ex}^{Na,0}}{c_{in}^{Na,0}}\right) = \frac{1}{z^{Na}}\log\left(\frac{c_{ex}^{Cl,0} - c_{ex}^{K,0}}{c_{in}^{Cl,0} + |z^{in}|A_{in} - c_{in}^{K,0}}\right).$$

Extracellular electric potential system

Substituting Equation (2.25) into Equation (2.20) yields ϕ_{in}

$$\phi_{in}^0(r) = \left(\frac{D_{ex}^{Cl}Pe_{in}\rho_0}{\sigma_{in}^0 Pe_{ex}} - \frac{\delta_9\sigma_{ex}^0}{\sigma_{in}^0}\right)\phi_{ex}^0(r) + \phi_{in}^0(1). \tag{2.28}$$

The value $\phi_{in}^0(1)$ is determined by the boundary condition of ϕ_{in}^0 in Equation (2.19), where

$$-\mathcal{M}_v^{in}\int_0^1 \left(2\left(\phi_{in}^0 - \phi_{ex}^0\right) - E^{Na,0} - E^{Cl,0}\right)s^2 ds = z^{Na}J_p^{Na}. \tag{2.29}$$

where we use

$$z^{Na}J_p^{Na} = -z^K J_p^K + I_p^\phi, \qquad \frac{R_s}{z^K}\left(\phi_{in} - E^K\right) = -J_p^K.$$

To summarize, we obtained the simplified model of system (2.18)-(2.19) as follows

$$-\frac{1}{r^2}\frac{d}{dr}\left(r^2\left(\delta_{10}\frac{d}{dr}c_{ex}^{Na,0} + \sigma_{ex}^0\frac{d}{dr}\phi_{ex}^0\right)\right) = \mathcal{M}_v^{ex}\left(2\left(\phi_{in}^0 - \phi_{ex}^0\right) - E^{Na,0} - E^{Cl,0}\right), \tag{2.30a}$$

$$\phi_{in}^0(r) = \left(\frac{D_{ex}^{Cl}Pe_{in}\rho_0}{\sigma_{in}^0 Pe_{ex}} - \frac{\delta_9\sigma_{ex}^0}{\sigma_{in}^0}\right)\phi_{ex}^0(r) + \phi_{in}^0(1), \tag{2.30b}$$

$$u_{ex}^0 = -\frac{d}{dr}p_{ex}^0 - \delta_1\frac{d}{dr}\phi_{ex}^0, \tag{2.30c}$$

$$u_{in}^0 = -u_{ex}^0 \tag{2.30d}$$

$$c_{ex}^{K,0} = c_0^{K,0} \exp\left(-\left(1 + \frac{D_{ex}^{Cl}}{D_{ex}^K}\right)\phi_{ex}^0\right), \tag{2.30e}$$

$$c_{in}^{K,0} = c_{in}^{K,0}(1) \exp\left(\left(\frac{Pe_{in}D_{ex}^{Cl}}{Pe_{ex}D_{in}^K} - \frac{Pe_{in}D_{ex}^{Cl}\rho_0}{Pe_{ex}\sigma_{in}^0}\right)\phi_{ex}^0\right) \exp\left(\left(\frac{\delta_9\sigma_{ex}^0}{\sigma_{in}^0}\right)\phi_{ex}^0\right), \tag{2.30f}$$

$$c_{ex}^{Na,0} = c_{ex}^{Cl,0} - c_{ex}^{K,0}, \tag{2.30g}$$

$$c_{in}^{Na,0} = c_{in}^{Cl,0} + z^{in}A_{in} - c_{in}^{K,0}, \tag{2.30h}$$

$$c_{in}^{Cl,0} = c_o^{Na,0} + c_o^{K,0} - \frac{1 + |z^{in}|}{2}A_{in}, \tag{2.30i}$$

$$c_{ex}^{Cl,0} = c_o^{Na,0} + c_o^{K,0}, \tag{2.30j}$$

$$p_{ex}^0 = \frac{D_{ex}^{Cl} - Pe_{ex}\delta_1}{Pe_{ex}}\phi_{ex}^0. \tag{2.30k}$$

with boundary conditions

$$\begin{cases} \dfrac{d\phi_{ex}^0}{dr} = 0, & \text{at } r = 0, \\ \phi_{ex}^0 = 0, & \text{at } r = 1. \end{cases} \tag{2.31}$$

Under the same assumptions as in [3], for example, uniform diffusion constants for all ions, constant Nernst potential, our simplified model (2.30) recovers the model proposed by Mathias. The main new contribution here is that we remove the assumptions that Nernst potentials and effective conductance should be constants in space. Using the relationships between ions concentrations and external potential, we obtain the space-dependent Nernst potential, which yields a much better approximation to the full model (see Figure 2.3).

2.3 Results and discussion

In this section, we present numerical simulations by using both the full and simplified models. The full model captures experimental observations in [1, 2] and simplified model provides us an explanation of our full model simulation results. In addition, our simplified model has lifted some restrictions compared to Mathias's model in [3] and we make a numerical comparison for those models.

2.3.1 Model calibration: membrane conductance effects intracellular hydrostatic pressure

In this section, we study the effect of connexins (gap junction) on intracellular hydrostatic pressure (p_{in}). We show the predictive power of the full model by comparing simulation results with the experimental observations.

The intracellular hydrostatic pressure is an important physiological quantity [67] and the connexins (gap junctions) conductance play an important role in the microcirculation of the

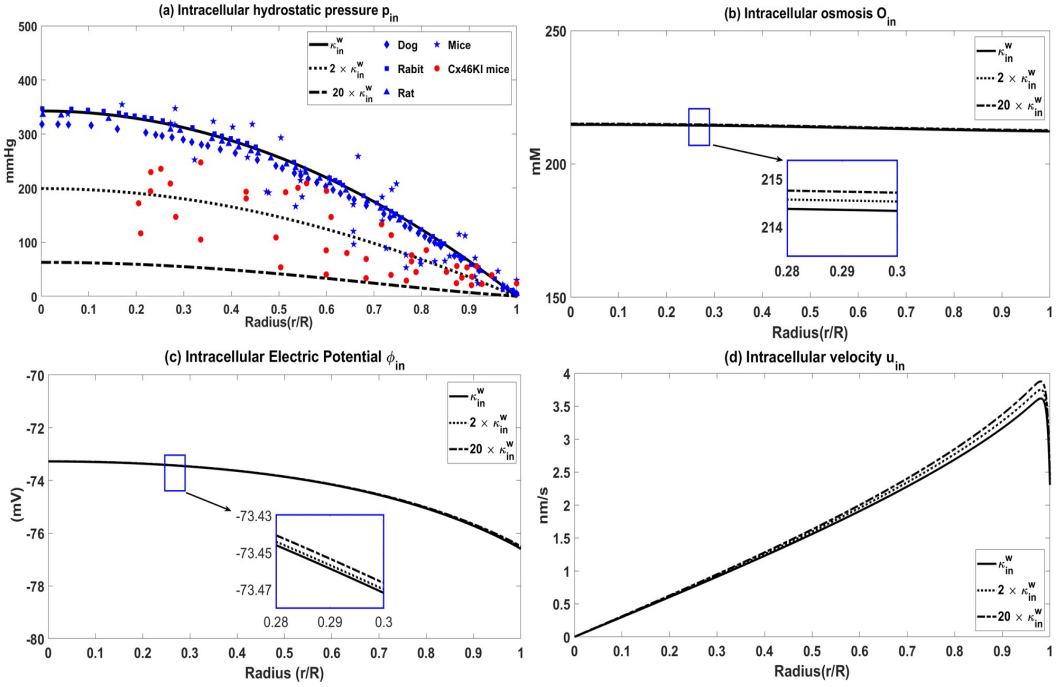

Figure 2.2: Comparison between different κ_{in}. The experimental data of dog, rabbit, rat come from paper [1]. Mice and Cx46 KI mice come from paper [2]. According to paper [2], the Cx46 KI mice lens has twice as many lens gap junction channels (lens connexins) compared with mice (the radius has been dimensionless for different species).

lens. In the experiment[1, 2], the intracellular hydrostatic pressure in Cx46 KI mice lens is compared with its in the normal lens. The Cx46 KI mice lens has doubled the number of connexins connected to fiber cells and provides more pathways for water transport between the fiber cells in comparison to the normal lens. It shows that this change of connexins has a dramatic effect on the intracellular hydrostatic pressure, which is shown in Figure 2.2a. If the conductivity of the connexins in the lens is approximately doubled, the hydrostatic pressure gradient in the lens should become approximately half of the original one.

This increased number of connexins should be captured by an increment in the water permeability in intracellular space in our lens model. We choose the value of intracellular conductance ($\frac{\kappa_{in}}{\mu_{in}}$) which correctly calculates the experimental result in the [1, 2]. In Figure 2.2a, the value $\kappa_{in}^{w} = 4.683 \times 10^{-20}/\mathrm{m}^2$ (black line) gives a good approximation to the experimental data (blue makers). When the conductivity of the connexins is doubled, to parameter value κ_{in} to be $2\kappa_{in}^{w}$ (the Cx46 KI mice lens as in the experiments [1, 2]), our model (black dot) can also match the experimental data (red markers): the intracellular hydrostatic pressure drops by half.

The numerical simulation in Figure 2.2a shows our full model successfully captures the intrinsic change in the intracellular hydrostatic pressure when the conductance of connexins changes. Interestingly, panels b-d in Figure 2.2 show that other intracellular quantities and

extracellular ones (see Appendix A.3) are insensitive to increases in the membrane permeability. This result can be explained by using our simplified system (2.30). If the variation of intracellular conductance still keeps δ_2 as a small quantity in the dimensionless system (2.14), our simplified model is still valid. In the simplified model, all quantities except for the intracellular hydrostatic pressure are independent of the number of connexins, i.e., of the intracellular effective conductance. All quantities except the intracellular hydrostatic potential are associated with the extracellular electric potential (ϕ_{ex}). However, the extracellular electric potential will not be affected by the change of the intracellular conductance, since Equation (2.30a) does not involve intracellular conductance or the number density of connexins (i.e., gap junctions).

2.3.2 Full model vs simplified model

In this section, we compare the full model (2.14)-(2.15) with the simplified model (2.30) and Mathias's model in [3]. Numerical results of the full model (Black lines) in Figure 2.3a-c suggest that the variations of the intracellular electric potential (ϕ_{in}), extracellular conductance (σ_{ex}), and Nernst potential of Cl^- (E^{Cl}) are rather small. The assumption of constant values for those variables in Mathias's model (shown as red dash-dot lines) is reasonable. However, the Nernst potentials of Na^+ and K^+ (Figure 2.3d-e) have large variations because of the sodium-potassium pump source on the surface of the lens. Our simplified model (blue dash lines) describes these variations with small errors. Comparisons for extracellular pressure, velocity, and potential (Figure 2.3 f-h) confirm that our simplified model yields good approximations to the full model.

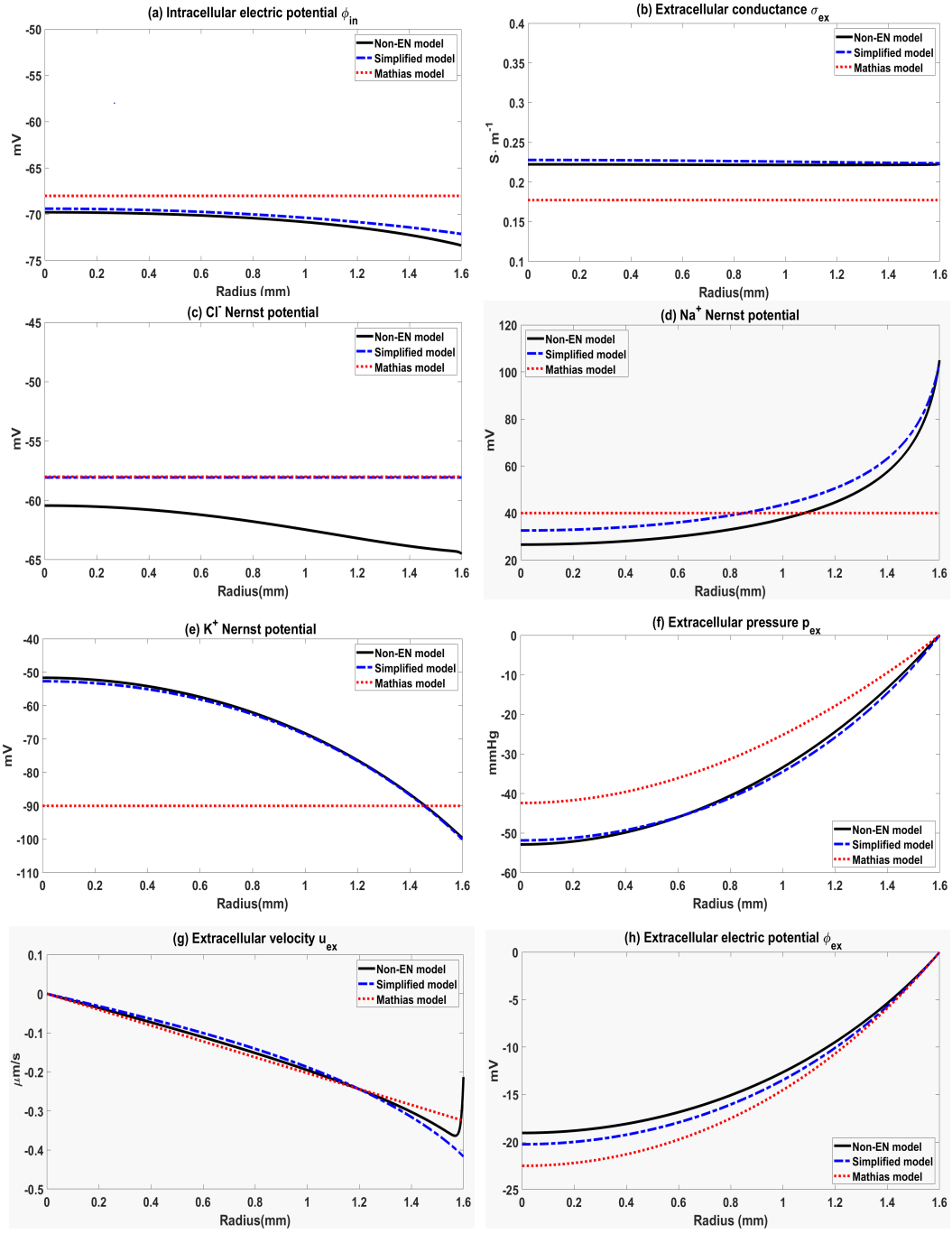

Figure 2.3: Comparison of the non-electro-neutral model, the simplified model and the Mathias's model in [3].

2.4 Conclusions

In this chapter, we propose a bidomain model to study the microcirculation of the lens. We include a capacitor in the representation of the membrane, and so our model is consistent

with classical electrodynamics. Consistency produces a linear correction term in the classical charge neutrality equation. This full model is calibrated by comparing it with experiments studying the effect of connexins on hydrostatic pressure. Our model can match the two experimental results with different connexins very well only by changing the intracellular membrane conductance (the strength of connexins). We conclude that our model can describe and predict the circulation of the lens. Furthermore, the numerical simulations show that the velocity and osmotic pressure in the intracellular and extracellular domains are not sensitive to increasing conductance.

Using asymptotic analysis, we derived a simplified model, which can be used to obtain the most interesting quantities except intracellular pressure. This simplified model could be further reduced to the model proposed by Mathias [3] with the additional assumptions that the Nernst potentials (which describe the gradients of the chemical potential of each ionic species) and spatial conductance are constant in space. However, we show that neither the Nernst potentials nor the conductance is constant. On the contrary, they vary significantly from the interior to the surface of the lens. Therefore, both of these quantities need to be coupled as part of the solution.

Another critical point to make is the decoupling of the intracellular pressure and the rest of the solution. Our simplified model suggests that all the qualities can be computed without knowing the intracellular pressure. On the other hand, we need to solve the full model to find the intracellular pressure value. The simplified model is to provide a link between the most recent computational models to some of the pioneering work in the 1970s and 80s. We strengthen the view that the lens provides an osmotic pump to maintain the microcirculation necessary to sustain a living lens for the animal's life.

Our model allows the calculation of variables that determine the role and life of the lens as an organ. Significant factors determine the transparency of the lens since that is the primary function of the organ. The dependence on the size of the extracellular space, and thus the pressure in extracellular and intracellular spaces and the difference between those two, is likely to be an important determinant of transparency. It can be imagined that the swelling of the extracellular space will scatter light, mainly because the swelling is likely to be irregular (in a way our model does not yet capture). Changes in the osmolarity (i.e., the activity of water estimated by the total concentration of solutes) are likely to be important as well.

This hydrodynamic bidomain model can point the way to dealing with other cells, tissues, and organs in which current flow, water flow, and cell volume changes are important. These include the kidney, the central nervous system (where the narrow extracellular space poses many of the biological problems facing the lens), the t-tubular system of skeletal and much cardiac muscle and so on. Additional compartments and additional structural complexity will surely be needed to deal with the workings of evolution. Through the study of microcirculation in the lens, we show that a mathematically well defined model can deal with the reality of biological structure and its complex distribution of channels.

Chapter 3

A tridomain model for optic nerve

In this chapter, as an extension of the model for the lens, we derive a tridomain model for the optic nerve, consisting of convection (due to water flow), diffusion, and electrical drift in three compartments: glial cells, neurons, and extracellular space. In Section 3.1, we present the modeling domain and global assumptions in the modeling. In Sections 3.2 and 3.3, we introduce the tridomain model for ion and water circulations in the optic nerve. This model is also applicable to other regions of the brain and central nervous system because mixtures of glial and nerve cells and nerve axons are found throughout the nervous system. In Section 3.4, we use the experimental system of the optic nerve, studied by the Harvard group Orkand et al [4, 22] as a prototype for the central nervous system in general and calibrate our model with experimental measurements. Through simulation study, our model predicts similar experimental results on the glial membrane potential variation when the axon is stimulated in bath solution with a given K^+ concentration.

3.1 Modeling domain and assumptions

In this section, we present a tridomain model for the microcirculation of optic nerve. The model deals with two types of flow: the circulation of water (hydrodynamics) and the circulation of ions (electrodynamics) in the

- glial compartment (Ω_{gl}).
- axon compartment (Ω_{ax}).
- extracellular space (Ω_{ex}).

The glial compartment and axon compartment are limited in the optic nerve, while extracellular space exists both in the optic nerve (Ω_{ex}^{OP}) and subarachnoid space (Ω_{ex}^{SAS}) (See Figure 3.1),

$$\Omega_{OP} = \Omega_{ax} \cup \Omega_{gl} \cup \Omega_{ex}^{OP}, \quad \Omega_{SAS} = \Omega_{ex}^{SAS}.$$

The model is derived from conservation laws of ions and water for flow through membranes between intracellular compartments (glial cells and axon) and extracellular space [68].

We first introduce the definition of the terms listed in the Glossary below, where $i = \mathrm{Na}^+, \mathrm{K}^+, \mathrm{Cl}^-$ for ion spices, $l = gl, ax, ex$ for glial compartment, axon compartment and extracellular space, and $k = gl, ax$ for glial or axon membrane in the optic nerve.

GLOSSARY

c_l^i: Ion i concentration in the l region,
ϕ_l: Electric potential in l region,
p_l: Hydrostatic pressure in l region,
η_l: Volume fraction of l region,
O_l: Osmotic concentration in l region,
$\mathbf{u}_l$: Fluid velocity inside of the l region,
$\mathbf{j}_l^i$: Ion i flux inside of l region,
U_k^m: Fluid transmembrane velocity on k membrane,
$J_k^{m,i}$:Ion i transmembrane flux on k membrane,
$J_{p,k}^i$: Active ATP based ion i pump on k membrane,
$J_{c,k}^i$: Passive transmembrane source of k membrane,
$I_{k,1}$: Max current of α_1- Na/K pump on k membrane,
$I_{k,2}$: Max current of α_2- Na/K pump on k membrane,
A_l: Negative charged protein density in l region,
$\mathcal{M}_k$: Membrane area k in per unit control volume,
κ_l: Water permeability of l region,
μ: Fluid viscosity,
L_k^m: Hydrostatic permeability of k membrane,
g_k^i: Conductance of k membrane for ion i,
$\bar{g}^i$: Maximum conductance of axon membrane for ion i,
g_{leak}^i: Leak conductance of axon membrane for ion i,
K_k: Stiffness constant of k membrane,
τ_l: Tortuosity of l region,
D_l^i: Diffusion coefficient of i ion in l region,
T: Temperature,
k_B: Boltzmann constant,
e: Electron charge,
z^i: Valence of the ion i.

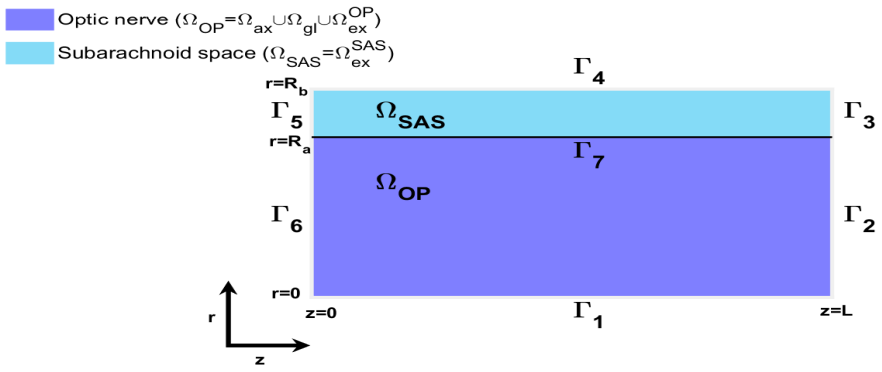

Figure 3.1: The optic nerve Ω_{OP} consists of axon compartment Ω_{ax}, glial compartment Ω_{gl} and extracellular space Ω_{ex}^{OP}. The subarachnoid space only has extracellular space Ω_{ex}^{SAS}.

Figure 1.3a shows the entire modeling region Ω that consists of the subarachnoid space (SAS) region Ω_{SAS} and optic nerve region Ω_{OP} (also see Figure 3.1),

$$\Omega = \Omega_{SAS} \cup \Omega_{OP}.$$

and the interface of Ω_{SAS} and Ω_{OP} is the pia mater denoted by Γ_7,

$$\Omega_{OP} \cap \Omega_{SAS} = \Gamma_7.$$

In our model, both pia mater Γ_7 and dura mater Γ_4 are modeled as macroscopic membranes with appropriate boundary conditions. The transmembrane water flow through pia mater [79] depends on hydrostatic and osmotic pressures, while that through dura mater only depends on the hydrostatic pressure. Obviously, at higher resolution, much more detail will be needed, and these structures will be represented in higher resolution models, in future studies, as the layered epithelia that they are.

For the boundaries, Γ_1 is the radius center of the optic nerve; Γ_2 and Γ_3 are the far end (away from the eyeball) of the optic nerve which is connected to optic canal region [14]. Γ_5 is used to model the dura mater connected to the sclera (the white matter of the eye) and assumed to be non-permeable [12]. Γ_6 is used to denote the lamina cribrosa where the optic nerve head exits the eye posteriorly through pores of the lamina cribrosa [69]. In the optic nerve region Ω_{OP}, the glial membrane and axon membrane separate domains Ω_{gl}, Ω_{ax} from the extracellular region Ω_{ex}^{OP}, respectively. Based on the structure of the optic nerve, we have the following global assumptions for the model:

Isotropy of glial compartment and extracellular space:

- the extracellular space forms a narrow structure of branching clefts surrounding the glial cells and nerve axons.
- the glial cells are connected by connexins and form a syncytium.
- the extracellular space is continuous and forms a syncytium.

Both syncytia are assumed isotropic here until we know better, and the axons are not connected. They are electrically separate. Current flow in one axon does not flow into its neighboring axon or glia. Current flow across the membrane of one axon flows down the axon and out across the membrane into the extracellular space, and then through the extracellular space back to the original membrane. Current completes its circuit in the axon and extracellular space, not in adjacent glia or axons.

For $l = gl, ex, i = \mathrm{Na}^+, \mathrm{K}^+, \mathrm{Cl}^-$, the ion flux and water flow velocity are in the following forms

$$\boldsymbol{j}_l^i = j_{l,r}^i \hat{\boldsymbol{r}} + j_{l,\theta}^i \hat{\boldsymbol{\theta}} + j_{l,z}^i \hat{\boldsymbol{z}},$$
$$\boldsymbol{u}_l = u_l^r \hat{\boldsymbol{r}} + u_l^\theta \hat{\boldsymbol{\theta}} + u_l^z \hat{\boldsymbol{z}}.$$

Anisotropy of axon compartment: The axons are separated, more or less parallel cylindrical cells that do not form a syncytium. For $i = \mathrm{Na}^+, \mathrm{K}^+, \mathrm{Cl}^-$, the ion flux and water flow velocity are in the following forms

$$\boldsymbol{j}_{ax}^i = j_{ax,z}^i \hat{\boldsymbol{z}},$$
$$\boldsymbol{u}_{ax} = u_{ax}^z \hat{\boldsymbol{z}}.$$

Charge neutrality: In each domain, we assume that electroneutrality such that

$$\begin{aligned} \eta_{gl} \sum_i z^i c^i_{gl} + z^{gl} \eta^{re}_{gl} A^{re}_{gl} = 0, \\ \eta_{ax} \sum_i z^i c^i_{ax} + z^{ax} \eta^{re}_{ax} A^{re}_{ax} = 0, \\ \sum_i z^i c^i_{ex} = 0, \end{aligned} \tag{3.1}$$

where $A^{re}_l > 0$ with $l = ax, gl$ is the density of proteins in axons or glial cells at resting state. The proteins are negatively charged, but a positive number of customarily describes the charge density. We assume the permanent negatively charged protein is uniformly distributed within glial cells and axons at resting state and has valence z^l, $l = gl, ax$. The η_{ax} and η_{gl} are the volume fraction of axon and glial compartments in the optic nerve and η^{re}_{ax} and η^{re}_{gl} are the resting state volume fractions.

Axis symmetry: For simplicity, axial symmetry is assumed. The model can be straightforwardly extended to three dimensions when data and needs justify the considerable extra computational resources needed to analyze such models.

3.2 Water circulation

We model water circulation with the following assumptions

- the loss or gain of water in axons and glial cells is only through membranes flowing into or out of the extracellular space.
- the transmembrane water flux is proportional to the intracellular/extracellular hydrostatic pressure and osmotic pressure differences.
- the glial cell and axons can swell and shrink due to the water inflows and outflows.

The conservation of mass in each domain yields

$$\begin{aligned} \frac{\partial \eta_{gl}}{\partial t} + \mathcal{M}_{gl} U^m_{gl} + \nabla \cdot (\eta_{gl} \boldsymbol{u}_{gl}) = 0, \text{ in } \Omega_{OP}, \\ \frac{\partial \eta_{ax}}{\partial t} + \mathcal{M}_{ax} U^m_{ax} + \frac{\partial}{\partial z} (\eta_{ax} u^z_{ax}) = 0, \text{ in } \Omega_{OP}, \\ \nabla \cdot (\eta_{gl} \boldsymbol{u}_{gl}) + \nabla \cdot (\eta_{ex} \boldsymbol{u}_{ex}) + \frac{\partial}{\partial z} (\eta_{ax} u^z_{ax}) = 0, \text{ in } \Omega_{OP}, \end{aligned} \tag{3.2}$$

where we assume that glial cells are isotropic, and axons are anisotropic. Here $\boldsymbol{u}_l$ with $l = gl, ax, ex$ is the velocity in the glial cells, axons, and extracellular space, respectively. The transmembrane water flow U^m_k with $k = gl, ax$ follows the Starling's law on the kth membrane,

$$\begin{aligned} U^m_{gl} = L^m_{gl} \left(p_{gl} - p_{ex} - \gamma_{gl} k_B T \left(O_{gl} - O_{ex} \right) \right), \\ U^m_{ax} = L^m_{ax} \left(p_{ax} - p_{ex} - \gamma_{ax} k_B T \left(O_{ax} - O_{ex} \right) \right). \end{aligned}$$

The p_l with $l = gl, ax, ex$ are the hydrostatic pressure in the glial cells, axons, and extracellular space, respectively. The $k_B T O_l$ is the theoretical osmotic pressure [64] where the O_l is the molar concentration of solute defined by

$$O_{ex} = \sum_i c_{ex}^i, \quad O_l = \sum_i c_l^i + \frac{\eta_j^{re}}{\eta_l} A_l^{re}, \quad l = gl, ax,$$

where $\frac{\eta_l^{re}}{\eta_l} A_l^{re} > 0$ with $l = gl, ax$ is the density of the permanent negatively charged protein in glial cells and axons that varies with the volume fraction of the region. The $\mathcal{M}_k$ and γ_k, $k = gl, ax$ are the glial cells (or axons) membrane area per unit volume and membrane reflection coefficient [70] respectively. The membrane reflection coefficient γ_k $(k = gl, ax)$ is the ratio between the observed osmotic pressure and theoretical osmotic pressure. k_B is Boltzmann constant, and T is temperature.
For the volume fraction η_l, $l = gl, ax, ex$, we have

$$\eta_{gl} + \eta_{ax} + \eta_{ex} = 1, \quad \text{in } \Omega. \tag{3.3}$$

The glial cells and axons are found only in the Ω_{OP} region. In other words, $\eta_{ax} = \eta_{gl} \equiv 0$ and $\eta_{ex} \equiv 1$ are fixed in Ω_{SAS}. Therefore, the solution is incompressible in the Ω_{SAS}, and we have

$$\nabla \cdot \boldsymbol{u}_{ex} = 0, \quad \text{in } \Omega_{SAS}.$$

The relation between the hydrostatic pressure p_l and volume fraction η_l $(l = gl, ax, ex)$ is connected by the force balance on the membrane [57, 64]

$$\begin{aligned} K_{gl}\left(\eta_{gl} - \eta_{gl}^{re}\right) &= p_{gl} - p_{ex} - \left(p_{gl}^{re} - p_{ex}^{re}\right), \quad \text{in } \Omega_{OP}, \\ K_{ax}\left(\eta_{ax} - \eta_{ax}^{re}\right) &= p_{ax} - p_{ex} - \left(p_{ax}^{re} - p_{ex}^{re}\right), \quad \text{in } \Omega_{OP}, \end{aligned} \tag{3.4}$$

where K_k $(k = gl, ax)$ is the stiffness constant related to Young's modules and Poisson's ratio. The p_l^{re} $(l = gl, ax, ex)$ is the resting state hydrostatic pressure.

Note that the concentrations of ions and effective concentration of water vary a great deal and so are described by equations in which the number density of ions and effective number density of water vary in both the radial and longitudinal directions according to conservation laws, without using compartments that may not have unique definitions or relations to anatomical structures. Indeed, the variation of concentration is one of the main determinants of the properties of ionic solutions. The solution is incompressible, but the components are not [71].
Next, we define the velocity in each domain.
Fluid Velocity in the Glial Compartment. As we mentioned before, the glial compartment is a connected space, where water can flow from cell to cell through connexins joining membranes of neighboring cells. The velocity of the fluid in glial syncytium $\boldsymbol{u}_{gl}$ depends on

the gradients of hydrostatic pressure and osmotic pressure as

$$\begin{aligned} u_{gl}^{r} &= -\frac{\kappa_{gl}\tau_{gl}}{\mu}\left(\frac{\partial p_{gl}}{\partial r} - \gamma_{gl}k_B T\frac{\partial O_{gl}}{\partial r}\right), \\ u_{gl}^{\theta} &= -\frac{\kappa_{gl}\tau_{gl}}{\mu}\left(\frac{1}{r}\frac{\partial p_{gl}}{\partial \theta} - \gamma_{gl}k_B T\frac{1}{r}\frac{\partial O_{gl}}{\partial \theta}\right), \\ u_{gl}^{z} &= -\frac{\kappa_{gl}\tau_{gl}}{\mu}\left(\frac{\partial p_{gl}}{\partial z} - \gamma_{gl}k_B T\frac{\partial O_{gl}}{\partial z}\right). \end{aligned} \tag{3.5}$$

The boundary conditions in the glial syncytium are as follows

$$\begin{cases} \boldsymbol{u}_{gl}\cdot\hat{\boldsymbol{r}} = 0, & \text{on } \Gamma_1, \\ \nabla p_{gl}\cdot\hat{\boldsymbol{z}} = 0, & \text{on } \Gamma_2, \\ \nabla p_{gl}\cdot\hat{\boldsymbol{z}} = 0, & \text{on } \Gamma_6, \\ \boldsymbol{u}_{gl}\cdot\hat{\boldsymbol{r}} = 0, & \text{on } \Gamma_7. \end{cases}$$

On boundary Γ_2 and Γ_6, the homogeneous Neumann boundary condition is applied. The no-flow boundary condition is used at Γ_7.

Fluid Velocity in the Axon Compartment. Since the axons are only connected in the longitudinal direction, the fluid velocity in the axons compartment is defined along z direction as

$$\begin{aligned} u_{ax}^{r} &= 0, \\ u_{ax}^{\theta} &= 0, \\ u_{ax}^{z} &= -\frac{\kappa_{ax}}{\mu}\frac{\partial p_{ax}}{\partial z}. \end{aligned} \tag{3.6}$$

Dirichlet boundary conditions are

$$\begin{cases} \boldsymbol{u}_{ax}\cdot\hat{\boldsymbol{z}} = u_{0l}, & \text{on } \Gamma_2, \\ \boldsymbol{u}_{ax}\cdot\hat{\boldsymbol{z}} = u_{0r}, & \text{on } \Gamma_6, \end{cases}$$

where u_{0l} and u_{0r} are inflow and outflow velocities at Γ_6 and Γ_2, respectively.

Fluid Velocity in the Extracellular Space. The extracellular space is narrow, and the extracellular velocity is determined by the gradients of hydrostatic pressure and electric potential

$$\begin{aligned} u_{ex}^{r} &= -\frac{\kappa_{ex}\tau_{ex}}{\mu}\frac{\partial p_{ex}}{\partial r} - k_e\tau_{ex}\frac{\partial \phi_{ex}}{\partial r}, \\ u_{ex}^{\theta} &= -\frac{\kappa_{ex}\tau_{ex}}{\mu}\frac{1}{r}\frac{\partial p_{ex}}{\partial \theta} - k_e\tau_{ex}\frac{1}{r}\frac{\partial \phi_{ex}}{\partial \theta}, \\ u_{ex}^{z} &= -\frac{\kappa_{ex}\tau_{ex}}{\mu}\frac{\partial p_{ex}}{\partial z} - k_e\tau_{ex}\frac{\partial \phi_{ex}}{\partial z}, \end{aligned} \tag{3.7}$$

where ϕ_{ex} is the electric potential in the extracellular space, τ_{ex} is the tortuosity of extracellular region [68, 72] and μ is the viscosity of water, k_e is introduced to describe the effect of

electro-osmotic flow [30, 32, 65], κ_{ex} is the permeability of extracellular space. Here the hydro permeability κ_{ex}, tortuosity τ_{ex} and electric-osmotic parameter k_e have two distinguished values in the region Ω_{ex}^{OP} and Ω_{ex}^{SAS},

$$\kappa_{ex} = \begin{cases} \kappa_{ex}^{OP}, \text{ in } \Omega_{OP}, \\ \kappa_{ex}^{SAS}, \text{ in } \Omega_{SAS}, \end{cases} \quad \tau_{ex} = \begin{cases} \tau_{ex}^{OP}, \text{ in } \Omega_{OP}, \\ \tau_{ex}^{SAS}, \text{ in } \Omega_{SAS}, \end{cases} \quad k_e = \begin{cases} k_e^{OP}, \text{ in } \Omega_{OP}, \\ k_e^{SAS}, \text{ in } \Omega_{SAS}, \end{cases}.$$

Since $\Gamma_2 \cup \Gamma_3$ are the far end of optic nerve away from eyeball and next to the optic canal, we assume the hydrostatic pressure of extracellular is equal to the cerebrospinal fluid (CSF) pressure. On the other hand, the intraocular pressure (IOP) is imposed at Γ_6 where the extracellular space is connected to the retina. At boundary Γ_5, we assume a non-permeable boundary. We are aware of the significance of the pressures and flows at these boundaries for clinical phenomena including glaucoma [46, 73, 74] and will return to that subject in later publications.

The lymphatic drainage produces the water flow across the semi-permeable membrane Γ_4 on the dura membrane, which depends on the difference between extracellular pressure and orbital pressure (OBP). We assume the velocity across the pia membrane Γ_7, is continuous and determined by the combination of hydrostatic and osmotic pressures. To summarize, the boundary conditions of the extracellular fluid are

$$\begin{cases} \boldsymbol{u}_{ex} \cdot \hat{\boldsymbol{r}} = 0, & \text{on } \Gamma_1, \\ p_{ex} = p_{CSF}, & \text{on } \Gamma_2 \cup \Gamma_3, \\ \boldsymbol{u}_{ex}^{SAS} \cdot \ \hat{\boldsymbol{r}} = L_{dr}^m \left(p_{ex}^{SAS} - p_{OBP} \right), & \text{on } \Gamma_4, \\ \boldsymbol{u}_{ex} \cdot \hat{\boldsymbol{z}} = 0, & \text{on } \Gamma_5, \\ p_{ex} = p_{ICP}, & \text{on } \Gamma_6, \\ \boldsymbol{u}_{ex}^{OP} \cdot \hat{\boldsymbol{r}} = \boldsymbol{u}_{ex}^{SAS} \cdot \hat{\boldsymbol{r}} = L_{pia}^m \left(p_{ex}^{OP} - p_{ex}^{SAS} - \gamma_{pia} k_B T \left(O_{ex}^{OP} - O_{ex}^{SAS} \right) \right), & \text{on } \Gamma_7, \end{cases} \tag{3.8}$$

where p_{CSF} is the cerebrospinal fluid pressure [46] and p_{ICP} is the pressure in the eye and p_{OBP} is the orbital pressure on the dura mater. For boundary conditions of the extracellular fluid, we refer to [75].

3.3 Ion transport

For ion circulation, we assume

- only three types of ions are considered: Na^+, K^+ and Cl^-.
- the Na/K pump is present on both glial and axon membranes.
- ion channel conductance on glial cell membranes is a fixed constant, independent of the voltage and time. The sodium conductance is assumed small, and its channel origin unknown. The potassium conductance is large and comes from the K_{ir4} channels [55, 76].

- sodium channel and potassium channel conductance on axons are voltage-gated, while the conductance of chloride channel is fixed.

The conservation of ion concentration implies the following system of partial differential equations to describe the dynamics of ions in each region, for $i = \mathrm{Na}^+, \mathrm{K}^+, \mathrm{Cl}^-$

$$\begin{aligned}
&\frac{\partial\left(\eta_{gl}c^i_{gl}\right)}{\partial t} + \mathcal{M}_{gl}J^{m,i}_{gl} + \nabla\cdot\left(\eta_{gl}\boldsymbol{j}^i_{gl}\right) = 0, && \text{in } \Omega_{OP},\\
&\frac{\partial\left(\eta_{ax}c^i_{ax}\right)}{\partial t} + \mathcal{M}_{ax}J^{m,i}_{ax} + \frac{\partial}{\partial z}\left(\eta_{ax}j^i_{ax,z}\right) = 0, && \text{in } \Omega_{OP},\\
&\frac{\partial\left(\eta_{ex}c^i_{ex}\right)}{\partial t} - \mathcal{M}_{ax}J^{m,i}_{ax} - \mathcal{M}_{gl}J^{m,i}_{gl} + \nabla\cdot\left(\eta_{ex}\boldsymbol{j}^i_{ex}\right) = 0, && \text{in } \Omega_{OP},
\end{aligned} \tag{3.9}$$

where the last equation reduces to the following in the Ω_{SAS} region,

$$\frac{\partial c^{i,SAS}_{ex}}{\partial t} + \nabla\cdot\boldsymbol{j}^{i,SAS}_{ex} = 0.$$

The transmembrane ion flux $J^{m,i}_k$ $(k = gl, ax)$ consists of active ion pump source $J^i_{p,k}$ and passive ion channel source $J^i_{c,k}$, on the kth membrane,

$$J^{m,i}_k = J^i_{p,k} + J^i_{c,k}, \quad k = gl, ax, \quad i = \mathrm{Na}^+, \mathrm{K}^+, \mathrm{Cl}^-.$$

On the glial cell membranes, $J^i_{c,gl}$ is defined as

$$J^i_{c,gl} = \frac{g^i_{gl}}{z^i e}\left(\phi_{gl} - \phi_{ex} - E^i_{gl}\right), \quad i = \mathrm{Na}^+, \mathrm{K}^+, \mathrm{Cl}^-, \tag{3.10}$$

where the Nernst potential is used to describe the gradient of chemical potential $E^i_{gl} = \frac{k_B T}{ez^i}\log\left(\frac{c^i_{ex}}{c^i_{gl}}\right)$ and the conductance g^i_{gl} for ith specie ion on the glial membrane is a fixed constant, independent of voltage and time.
On the axon's membrane, $J^i_{c,ax}$ is defined as

$$J^i_{c,ax} = \frac{g^i_{ax}}{z^i e}\left(\phi_{ax} - \phi_{ex} - E^i_{ax}\right), \quad i = \mathrm{Na}^+, \mathrm{K}^+, \mathrm{Cl}^-,$$

where

$$g^{Na}_{ax} = \bar{g}^{Na}m^3h + g^{Na}_{leak}, \quad g^K_{ax} = \bar{g}^K n^4 + g^K_{leak}, \quad g^{Cl}_{ax} = g^{Cl}_{leak}.$$

The time-dependent dynamic of open probability, often loosely called 'gating' is governed by the Hodgkin-Huxley model [66, 77]

$$\begin{aligned}
\frac{dn}{dt} &= \alpha_n(1-n) - \beta_n n,\\
\frac{dm}{dt} &= \alpha_m(1-m) - \beta_m m,\\
\frac{dh}{dt} &= \alpha_h(1-h) - \beta_h h.
\end{aligned} \tag{3.11}$$

For the active ion pump source $J^i_{p,k}$, we assume that the only pump is the Na/K active transporter. We are more than aware that other active transport systems can and likely do move ions and water in this system. They will be included as experimental information becomes available.
In the case of Na/K pump source $J^i_{p,k}$ $(k = gl, ax)$, the strength of ion pump I_k depends on the concentrations in intracellular and extracellular spaces [34, 77], such that

$$J^{Na}_{p,k} = \frac{3I_k}{e}, \quad J^{K}_{p,k} = -\frac{2I_k}{e}, \quad J^{Cl}_{p,k} = 0, \quad k = gl, ax, \tag{3.12}$$

where

$$I_{gl} = I_{gl,1}\left(\frac{c^{Na}_{gl}}{c^{Na}_{gl} + K_{Na1}}\right)^3\left(\frac{c^{K}_{ex}}{c^{K}_{ex} + K_{K1}}\right)^2 + I_{gl,2}\left(\frac{c^{Na}_{gl}}{c^{Na}_{gl} + K_{Na2}}\right)^3\left(\frac{c^{K}_{ex}}{c^{K}_{ex} + K_{K2}}\right)^2,$$
$$I_{ax} = I_{ax,1}\left(\frac{c^{Na}_{ax}}{c^{Na}_{ax} + K_{Na1}}\right)^3\left(\frac{c^{K}_{ex}}{c^{K}_{ex} + K_{K1}}\right)^2 + I_{ax,2}\left(\frac{c^{Na}_{ax}}{c^{Na}_{ax} + K_{Na2}}\right)^3\left(\frac{c^{K}_{ex}}{c^{K}_{ex} + K_{K2}}\right)^2.$$

$I_{k,1}$ and $I_{k,2}$ are related to the maximum current of α_1- and α_2- isoform of Na/K pump on the glial membrane $(k = gl)$ or axon membrane $(k = ax)$.
The definitions of ion flux in each domain are as follows, for $i = \mathrm{Na}^+, \mathrm{K}^+, \mathrm{Cl}^-$,

$$\boldsymbol{j}^i_l = c^i_l \boldsymbol{u}_l - D^i_l \tau_l \left(\nabla c^i_l + \frac{z^i e}{k_B T} c^i_l \nabla \phi_l\right), \quad l = gl, ex,$$
$$j^i_{ax,z} = c^i_{ax} u^z_{ax} - D^i_{ax}\left(\frac{\partial c^i_{ax}}{\partial z} + \frac{z^i e}{k_B T} c^i_{ax}\frac{\partial \phi_{ax}}{\partial z}\right).$$

For the axon compartment boundary condition, we have

$$c^i_{ax} = c^{i,re}_{ax}, \quad \text{on} \ \ \Gamma_2 \cup \Gamma_6,$$

and glial compartment boundary condition, we have

$$\begin{cases} \boldsymbol{j}^i_{gl} \cdot \hat{\boldsymbol{r}} = 0, & \text{on } \Gamma_1, \\ c^i_{gl} = c^{i,re}_{gl}, & \text{on } \Gamma_2 \cup \Gamma_6, \\ \boldsymbol{j}^i_{gl} \cdot \hat{\boldsymbol{r}} = 0, & \text{on } \Gamma_7, \end{cases}$$

where the Dirichlet boundary conditions are used at locations $\Gamma_2 \cup \Gamma_6$ for axons and glial cell, and a non-flux boundary condition is used for glial cells ions flux on pia mater Γ_7.
Similar boundary conditions are imposed for the extracellular space boundary condition except on the pia mater Γ_7. The ion flux across the pia mater is assumed continuous and follows Ohm's law [58]. Additionally, a non-flux boundary condition is used at location Γ_5 and a homogeneous Neumann boundary condition is applied at the location of the dura

mater Γ_4,

$$\begin{cases} \boldsymbol{j}_{ex}^i \cdot \hat{\boldsymbol{r}} = 0, & \text{on } \Gamma_1, \\ c_{ex}^i = c_{csf}^i, & \text{on } \Gamma_2 \cup \Gamma_3, \\ \nabla c_{ex}^i \cdot \hat{\boldsymbol{r}} = 0, & \text{on } \Gamma_4, \\ \boldsymbol{j}_{ex}^i \cdot \hat{\boldsymbol{z}} = 0, & \text{on } \Gamma_5, \\ c_{ex}^i = c_{eye}^i, & \text{on } \Gamma_6, \\ \boldsymbol{j}_{ex}^{i,OP} \cdot \hat{\boldsymbol{r}} = \boldsymbol{j}_{ex}^{i,SAS} \cdot \hat{\boldsymbol{r}} = \frac{G_{pia}^i}{z^i e} \left(\phi_{ex}^{OP} - \phi_{ex}^{SAS} - E_{pia}^i \right), & \text{on } \Gamma_7. \end{cases}$$

By multiplying equations in (3.9) with $z_i e$ respectively and summing up, we have following system for the electric potentials in axon compartment, glial compartment and extracellular space,

$$\begin{aligned} \sum_i z^i e \mathcal{M}_{gl} J_{gl}^{m,i} + \sum_i z^i e \nabla \cdot \left(\eta_g \boldsymbol{j}_{gl}^i \right) = 0, \\ \sum_i z^i e \mathcal{M}_{ax} J_{ax}^{m,i} + \sum_i z^i e \frac{\partial}{\partial z} \left(\eta_{ax} j_{ax,z}^i \right) = 0, \\ \sum_i z^i e \nabla \cdot \left(\eta_{gl} \boldsymbol{j}_{gl}^i \right) + \sum_i z^i e \frac{\partial}{\partial z} \left(\eta_{ax} j_{ax,z}^i \right) + \sum_i z^i e \nabla \cdot \left(\eta_{ex} \boldsymbol{j}_{ex}^i \right) = 0, \end{aligned} \tag{3.13}$$

where we use the charge neutrality condition in Equation (3.1).
In the subarachnoid space Ω_{SAS}, the governing equation for extracellular potential reduce to

$$\sum_i z^i e \nabla \cdot \left(\sum_i \boldsymbol{j}_{ex}^{i,SAS} \right) = 0. \tag{3.14}$$

The boundary conditions for electric fields ϕ_{ax}, ϕ_{gl} and ϕ_{ex} are given below.
In the axon compartment:

$$\begin{cases} \nabla \phi_{ax} \cdot \hat{\boldsymbol{z}} = 0, \text{ on } \Gamma_2, \\ \nabla \phi_{ax} \cdot \hat{\boldsymbol{z}} = 0, \text{ on } \Gamma_6, \end{cases}$$

In the glial compartment:

$$\begin{cases} \nabla \phi_{gl} \cdot \hat{\boldsymbol{r}} = 0, & \text{on } \Gamma_1, \\ \nabla \phi_{gl} \cdot \hat{\boldsymbol{z}} = 0, & \text{on } \Gamma_2, \\ \nabla \phi_{gl} \cdot \hat{\boldsymbol{z}} = 0, & \text{on } \Gamma_6, \\ \nabla \phi_{gl} \cdot \hat{\boldsymbol{r}} = 0, & \text{on } \Gamma_7, \end{cases}$$

and in the extracellular space:

$$\begin{cases} \nabla\phi_{ex}\cdot\hat{\boldsymbol{r}}=0, & \text{on } \Gamma_1,\\ \nabla\phi_{ex}\cdot\hat{\boldsymbol{z}}=0, & \text{on } \Gamma_2\cup\Gamma_3,\\ \nabla\phi_{ex}\cdot\hat{\boldsymbol{r}}=0, & \text{on } \Gamma_4,\\ \nabla\phi_{ex}\cdot\hat{\boldsymbol{z}}=0, & \text{on } \Gamma_5,\\ \nabla\phi_{ex}\cdot\hat{\boldsymbol{z}}=0, & \text{on } \Gamma_6,\\ \sum_i z^i e\boldsymbol{j}_{ex}^{i,OP}\cdot\hat{\boldsymbol{r}}=\sum_i z^i e\boldsymbol{j}_{ex}^{i,SAS}\cdot\hat{\boldsymbol{r}}=\sum_i G_{pia}^i\left(\phi_{ex}^{OP}-\phi_{ex}^{SAS}-E_{pia}^i\right), & \text{on } \Gamma_7. \end{cases} \tag{3.15}$$

3.4 Model calibration

Our work is made possible because of and was motivated by the paper of Orkand et al. [4, 13], that measured the accumulation of potassium in the narrow extracellular space of the optic nerve of the amphibian salamander Necturus, in the spirit of the original work of Frankenhaeuser and Hodgkin [25], who were the first to analyze the accumulation of potassium outside a nerve fiber. The existence and qualitative properties of this potassium accumulation were known and caused concern to Hodgkin from his first work on the voltage clamp [78].

A key experiment in Orkand paper [4] measures the change in potential across the glial membrane produced by a train of action potentials. The glial membrane potential is used to estimate and report potassium concentration in the narrow extracellular space.

In the experiment, the optic nerve was placed in bath solutions with three different K^+ concentrations (1.5 mM, 3 mM, 4.5 mM) and the resting potential across the glial membrane was measured. Then the axon was stimulated to give a train of action potentials. Action potentials increased K^+ in the extracellular space (ECS) and the accumulated K^+ then made the glial membrane potential more positive. Stimuli were applied to both ends of the optic nerve region, thereby producing a more uniform (in space) potential within that region (see Appendix B).

The model of this system is solved by using the Finite Volume Method with mesh size $h = 1/20$ and temporal size $t = 1/10$ in dimensionless units. The code is written and executed in the Matlab environment. The flowchart for the simulation is shown in Figure 3.2. In the first step, we obtain the resting state of the system by iteration and fixed volume fraction [13]

$$\eta_{ax}^{re}=0.5,\ \eta_{gl}^{re}=0.4,\ \eta_{ex}^{re}=0.1.$$

In the dynamic process, the resting state values are taken as initial values. Then, we first solve the concentration governing equations, followed by electrical potentials equation and pressure equations. We update the volume fraction by using Equation (3.4).

In our simulation study, we first set the ECS concentration of K^+ to 3 mM and obtained a resting potential across the glial membrane (~ -89 mV). In Orkand's work [4, 13], suction electrodes were used for stimulating; The two ends of the optic nerve were placed in suction

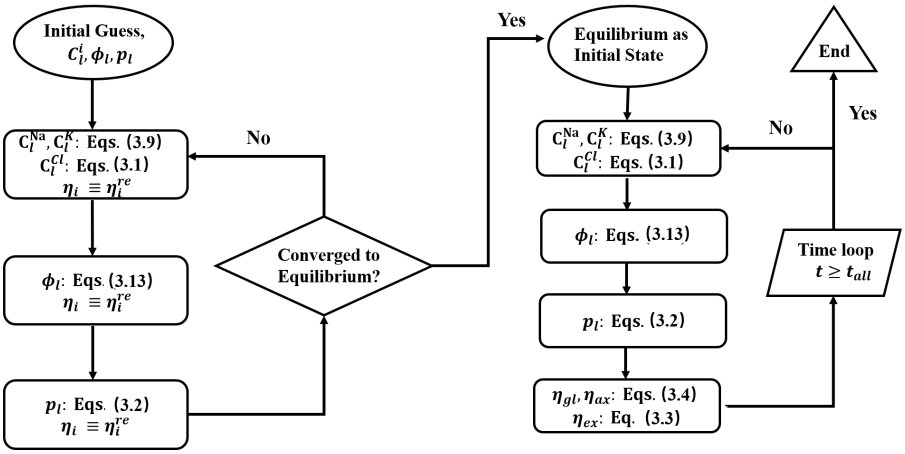

Figure 3.2: Flowchart for simulation process

electrodes. We modeled the suction electrodes by applying a train of rectangular function (sometimes called a box car stimulus in the engineering literature) currents through the axon membrane at $z = 2.25$ mm, 13.5 mm, and $0 < r < R_a = r^* = 48$ μm. Each stimulus in the train lasted 3 ms (as Orkand's paper indicated) with current strength 3 mA/m^2. The stimulus was large enough to exceed the threshold and generate action potentials. After a train of stimuli with a frequency of 17/s for 1 s, the first panel of Figure 3.3 shows the train of axon membrane action potentials and its return to the initial level (~ -89 mV) after 1 s. The profiles of the first action potential and the last action potential in the train are presented in the second panel. The third and fourth panels are used to illustrate the increase in glial cell membrane potential and extracellular potassium concentration during and after the train of stimuli. The fourth panel of Figure 3.3 shows that during stimulus, the ECS K^+ concentration keeps increasing due to the opening of the voltage-gated potassium channel of the axon membrane. As a result of the accumulated K^+ in the ECS, the membrane potential of glial cells also continues to increase until the stimulus stops.

Then, we vary the ECS K^+ between 1.5 mM, 3 mM, 4.5 mM and record the magnitude of the maximum glial membrane depolarized potential in each case, as in Figure 3.4. The dark squares are used for experimental data; the red triangles are simulation results of our model, respectively. Figure 3.4 shows that our model can very well match the experimental resting potentials (solid symbols) and depolarization potentials (open symbols) with different ECS K^+ concentrations.

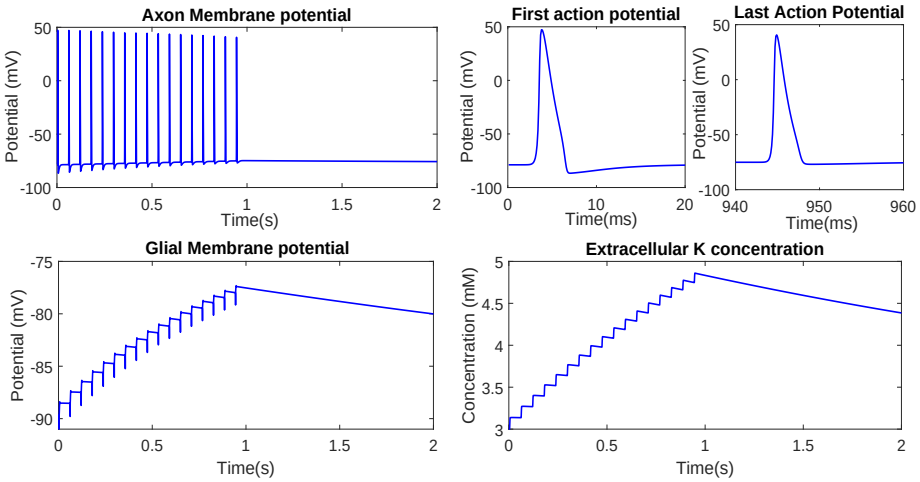

Figure 3.3: Recording axon membrane potential, glial membrane potential and extracellular K^+ at center axis point (where $r = 0$ and $z = L/2$) when the extracellular solution with 3 mM K^+.

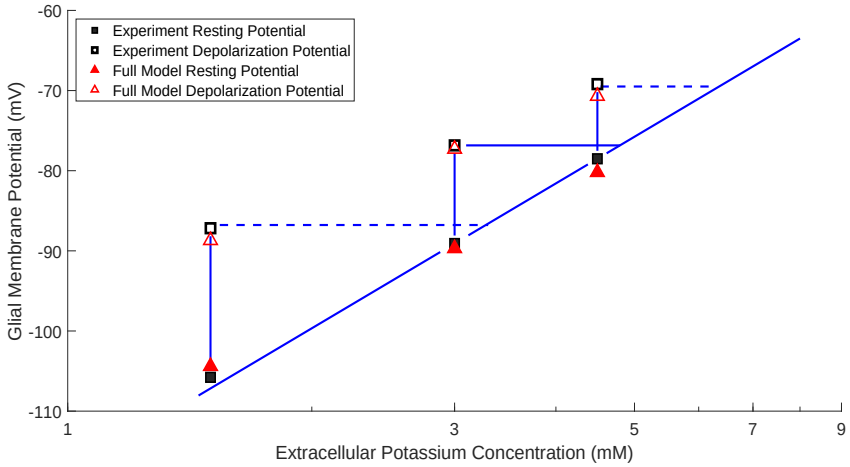

Figure 3.4: Comparison between the experimental results in [4] and numerical simulations of the effect of nerve impulses on the membrane potential of glial cells. The solid symbols are resting potentials, and the open symbols are depolarization potentials with different ECS K^+ concentrations.

Chapter 4

Effects of water in the optic nerve

In this chapter, we estimate the ion fluxes and water flows in regions when the nerve is stimulated and explore how the nervous (neuron-glia) system interacts with the extracellular space to create microcirculation in the optic nerve.

In Section 4.1, we identify the osmotic pressure as driving force for water circulation when part of axon stimulated. We examine water circulation pattern and their effects on ion concentrations and fluxes within and between each compartment. In addition, we find that the electric-coupled glial compartment serves as an important and quick potassium transport device to remove excessive potassium in the extracellular space during the axon firing.

In Section 4.2, we verify our estimations on the ion fluxes and water circulation pattern in the optic nerve through numerical simulations. In addition, we compare the convection-electrodiffusion (full) model with the corresponding electrodiffusion model and find that osmosis-driven water flow plays an important role in glial buffering. Furthermore, we show the multiple train of stimulus can enhance this convective effect on potassium transport in the glial compartment.

4.1 Water circulation driven by osmotic pressure

In this section, we estimate the transmembrane fluxes and the resulting accumulation of ions in the extracellular space when part of the nerve is stimulated. Our estimations show that the variation of osmotic pressure in extracellular space is the dominant mechanism that drives the water flow. The circulation pattern and strength of water flow in the optic nerve are also discussed.

To simplify our discussions, we focus our analysis on an idealized setting where the stimulus is applied at a part of the axon membranes. As shown in Figure 4.1, the stimulus has applied at $r < r_{sti}$ at a given location $z = z_0$ with $\theta \in [0, 2\pi]$. This stimulus is located within the optic nerve, so $r_{sti} < R_a = r^*$. We distinguish between the stimulated region and the non-stimulated region in the optic nerve Ω_{OP} shown in the Figure 4.1 since the electrical signals propagate in the z direction in the axon compartment. We do not put the stimulus all over in this stimulated region, rather we apply the stimulus only at the location

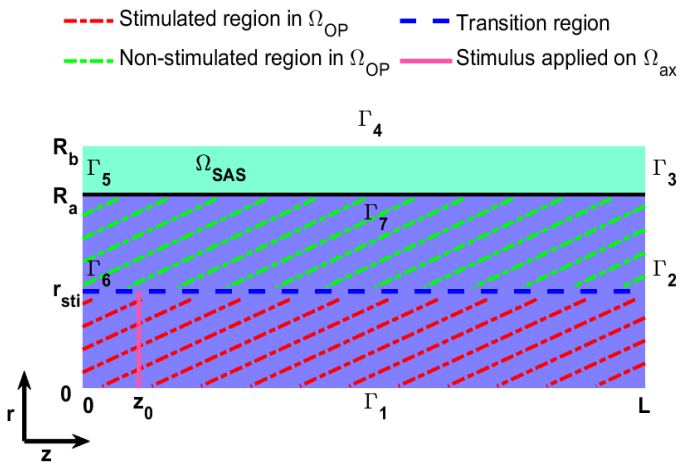

Figure 4.1: Stimulated and non-stimulated regions in the optic nerve (Ω_{OP}). The stimulus is applied on the axon membrane, where $r < r_{sti}$ at a given location $z = z_0$.

(z_0) within the radius r_{sti}. In the next chapter, we present the results when different spatial distributions of stimuli are applied.

To understand the mechanism inducing the water circulation, we first estimate the changes in ion concentration in the extracellular space during a single action potential. Then we analyze the different transmembrane currents in the glial compartment and identify the dominant K^+ current. Finally, we study the osmotic pressure change after a train of action potentials generated by the axon.

4.1.1 Single action potential estimation

Based on our estimations in this section, we find that the variations of Na^+ and K^+ in the extracellular space of the stimulated region are the same at the leading order, and that agrees with experimental observations [53, 79, 80]. Although the estimation of ion fluxes is based on the classic Hodgkin-Huxley model, the methods are general and can be applied to systems with other channels and transporters.

When an action potential is generated by the nerve, the equilibrium flux formed by the ion concentration gradient and electric potential difference on the axon membrane is lost. Since the condition changes, we introduce notations to separate the resting state variables (with superscript 're') before the action potentials from the variables during the action potentials (with superscript 'dy').

We introduce the current of ith ionic species through axon and glial membrane as

$$I_k^{i,j} = z^i e J_k^{m,i,j} = z^i e J_{p,k}^{i,j} + z^i e J_{c,k}^{i,j},\ i = \mathrm{Na}^+, \mathrm{K}^+, \mathrm{Cl}^-,\ j = re, dy,\ k = gl, ax,$$

where $J_k^{m,i,j}$ consists of the active Na/K pump source ($J_{p,k}^{i,j}$) and passive ion channel source

($J_{c,k}^{i,j}$) for ith ionic species on the axons ($k = ax$) or glial cells membranes ($k = gl$) at resting state ($j = re$) before the action potentials or during the action potentials ($j = dy$).

At the resting state, Na/K pump source $J_{p,k}^{i,re}$ and ion channels source $J_{c,k}^{i,re}$ on the axon membrane ($k = ax$) and glial membrane ($k = gl$) satisfy

$$J_{p,k}^{Na,re} = \frac{3I_k^{re}}{e}, \quad J_{p,k}^{K,re} = -\frac{2I_k^{re}}{e}, \quad J_{p,k}^{Cl,re} = 0,$$
$$J_{c,k}^{i,re} = \frac{g_k^{i,re}}{z^i e}\left(V_k^{re} - E_k^{i,re}\right),\ i = \mathrm{Na}^+, \mathrm{K}^+, \mathrm{Cl}^-,\ k = gl, ax,$$

where the membrane potential V_k^{re} at the resting state is

$$V_k^{re} = \phi_k^{re} - \phi_{ex}^{re}, \quad k = gl, ax.$$

The ion channel conductance on the axon membrane is defined as in the classical Hodgkin-Huxley model

$$g_{ax}^{Na,re} = \bar{g}^{Na}\left(m^{re}\right)^3 h^{re} + g_{leak}^{Na},\ \ g_{ax}^{K,re} = \bar{g}^{K}\left(n^{re}\right)^4 + g_{leak}^{K},\ \ g_{ax}^{Cl,re} = g_{leak}^{Cl},$$

and the ion channel conductance on the glial membrane is a fixed constant,

$$g_{gl}^{i,re} = g_{gl}^{i}.$$

The kinetic variables m^{re}, h^{re} and n^{re} are measures of the resting state open probability for the voltage-gated Na^+ and K^+ channel on the axon membrane. In addition, in the resting state, the ion fluxes through the active Na/K pump $J_{p,k}^{i,re}$ and ion channel $J_{c,k}^{i,re}$ in the glial membrane ($k = gl$) or axon membrane ($k = ax$) are balanced in magnitude

$$O\left(|J_{p,k}^{i,re}|\right) = O\left(|J_{c,k}^{i,re}|\right),\ i = \mathrm{Na}^+, \mathrm{K}^+, \mathrm{Cl}^-,\ k = gl, ax.$$

During action potentials, the ion fluxes through active Na/K pump are

$$J_{p,k}^{Na,dy} = \frac{3\left(I_k^{re} + \delta I_k\right)}{e}, \quad J_{p,k}^{K,dy} = -\frac{2\left(I_k^{re} + \delta I_k\right)}{e}, \quad k = gl, ax,$$

where δI_k is the variation of current through Na/K pump in the membrane due to the ion concentration changes . The ion fluxes through ion channels can be written as

$$J_{c,k}^{i,dy} = \frac{g_k^{i,dy}}{z^i e}\left(V_k^{re} - E_k^{i,re}\right) + \frac{g_k^{i,dy}}{z^i e}\left(\delta V_k - \delta E_k^i\right),\ i = \mathrm{Na}^+, \mathrm{K}^+, \mathrm{Cl}^-,\ k = gl, ax,$$

where $\delta \mathrm{X}_k = \mathrm{X}_k^{dy} - \mathrm{X}_k^{re}$ is the deviation of X away from the resting state value with $\mathrm{X} = V, E, I$ on the membrane. For the conductance on membranes, we have

$$g_{ax}^{Na,dy} = \bar{g}^{Na}\left(m^{dy}\right)^3 h^{dy} + g_{leak}^{Na},\ \ g_{ax}^{K,dy} = \bar{g}^{K}\left(n^{dy}\right)^4 + g_{leak}^{K},\ \ g_{ax}^{Cl,dy} = g_{ax}^{Cl,re},$$
$$g_{gl}^{i,dy} = g_{gl}^{i,re},\ \ i = \mathrm{Na}^+, \mathrm{K}^+, \mathrm{Cl}^-,$$

where m^{dy}, h^{dy} and n^{dy} are governed by system (3.11). During a single action potential, we claim that the variation of ion's Nernst potential is much smaller than changes in the axon membrane potential (see Appendix C.1),

$$\delta E_{ax}^{i} = o\left(\delta V_{ax}^{*}\right), \quad i = \mathrm{Na}^{+}, \mathrm{K}^{+}, \mathrm{Cl}^{-},$$

At the same time, we estimate that

$$J_{p,ax}^{i,dy} = o\left(\frac{g_{ax}^{i,dy}}{z^{i}e}\left(V_{ax}^{re} - E_{ax}^{i,re}\right)\right), \quad i = \mathrm{Na}^{+}, \mathrm{K}^{+}.$$

This is because the voltage-gated Na^{+} and K^{+} channels are open during the action potential and satisfy

$$g_{ax}^{i,re} = o\left(g_{ax}^{i,dy}\right), \quad i = \mathrm{Na}^{+}, \mathrm{K}^{+}.$$

In addition, the increments of Na/K pump strength is limited since the ion fluxes through the Na/K pump is controlled by its maximum currents $I_{ax,1}$ and $I_{ax,2}$ in Equation (3.12).

In sum, during action potentials, we can approximate the axon transmembrane current for each ionic species as

$$I_{ax}^{i,dy} \approx g_{ax}^{i,dy}\left(V_{ax}^{re} - E_{ax}^{i,re}\right) + g_{ax}^{i,dy}\delta V_{ax}, \quad i = \mathrm{Na}^{+}, \mathrm{K}^{+}, \mathrm{Cl}^{-}. \tag{4.1}$$

In the next paragraphs, by using Equation (4.1), we estimate the accumulative Na^{+} and K^{+} fluxes through the axon membrane during a single action potential. This estimation helps us estimate the concentration changes in the stimulated extracellular region.

The governing equation of the open probability for Na^{+} channel m-gates in the Hodgkin-Huxley model is

$$\frac{dm^{dy}}{dt} = \alpha_m\left(1 - m^{dy}\right) - \beta_m m^{dy}, \tag{4.2}$$

where

$$\alpha_m = \frac{1}{10}\frac{25 - \delta V_{ax}}{\exp\left(\frac{25-\delta V_{ax}}{10}\right) - 1}, \quad \beta_m = 4\exp\left(-\frac{\delta V_{ax}}{18}\right), \tag{4.3}$$

and $\delta V_{ax} = V_{ax}^{dy} - V_{ax}^{re}$.
The solution for Equation (4.2) is

$$m^{dy}(t) = m_0 \exp\left(\int_0^t \alpha_m(s) + \beta_m ds\right) + \int_0^t \alpha_m(s)\exp\left(-\int_s^t \alpha_m(u) + \beta_m(u)du\right)ds, \tag{4.4}$$

with initial value m_0.
For a single action potential period $[0, T_{ax}^{*}]$, we define two distinguished time intervals based on the rapidly-responding m-gates open probability m^{dy} as shown in Figure 4.2.

The first period $[0, t_{m1}]$ is when the Na^{+} channel becomes fully open, and the action membrane potential moves positive from its resting value to its most positive value (at the peak of its overshoot, as it was classically named). The second period $[t_{m1}, T_{ax}^{*} = t_{m1} + t_{m2}]$

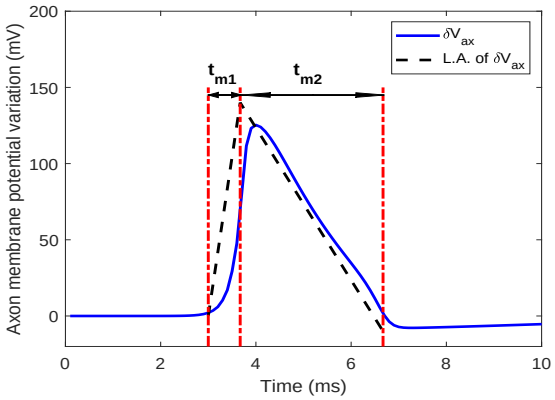

Figure 4.2: Two distinguished time intervals used in the estimation during a single action potential. The blue line is the axon membrane potential variation $\delta V_{ax} (= V_{ax}^{dy} - V_{ax}^{re})$ during a single action potential. The dark dash line is the linear approximation of the δV_{ax}. t_{m1} and t_{m2} are the time parameters in Equations (C.7) and (C.8).

occurs when the Na^+ channel closes and the action potential recovers from the peak value to the hyperpolarization value.

At the first time interval $[0, t_{m1}]$, we estimate that δV_{ax} increases monotonically from 0 to $E_{ax}^{Na,re} - V_{ax}^{re}$, where we approximate the peak value of action potential by the Nernst potential of Na^+ in the resting state such that

$$\delta V_{ax}(t) = \frac{E_{ax}^{Na,re} - V_{ax}^{re}}{t_{m1}} t, \quad t \in [0, t_{m1}]. \tag{4.5}$$

In Equation (4.5), t_{m1} is an unknown variable. The initial value of Equation (4.4) is chosen as

$$m_0 = m^{re} = m^{eq}(0),$$

where m^{eq} is the equilibrium state of Equation (4.2) depending on δV_{ax}, such that

$$m^{eq}(\delta V_{ax}) = \frac{\alpha_m(\delta V_{ax})}{\alpha_m(\delta V_{ax}) + \beta_m(\delta V_{ax})}. \tag{4.6}$$

By using Equations (4.3), (4.4) and (4.5), we can obtain one equation for t_{m1} as shown in Equation (C.7) (see Appendix C.2). Without loss of generality, we assume the voltage-gated Na^+ channel is almost fully open when $t = t_{m1}$ and $m^{dy}(t_{m1}) = 0.95$[1]. The estimation from Equation (C.7) gives $t_{m1} \approx 0.67$ ms.

At the second time interval, we use the homogeneous property of Equation (4.2) and move the time interval $[t_{m1}, T_{ax}^* = t_{m1} + t_{m2}]$ to $[0, t_{m2}]$ to simplify the notation. We assume

[1]The trajectory of m^{dy} in Equation (4.2) follows its equilibrium $m^{eq}(\delta V_{ax})$.

that δV_{ax} decreases monotonically from $E_{ax}^{Na,re} - V_{ax}^{re}$ to $E_{ax}^{K,re} - V_{ax}^{re}$ at second time period such that

$$\delta V_{ax}(t) = E_{ax}^{Na,re} - V_{ax}^{re} - \frac{E_{ax}^{Na,re} - E_{ax}^{K,re}}{t_{m2}} t, \quad t \in [0, t_{m2}]. \tag{4.7}$$

We assume that the initial value m_0 of Equation (4.4) at the second time period is

$$m_0 = m^{dy}(t_{m1}).$$

The Na^+ channel is in a nearly closed state when the δV_{ax} approaching $E_{ax}^{K,re} - V_{ax}^{re}$ and we assume $m^{dy}(t_{m2}) = 0.1$. In a similar way, by using Equations (4.3), (4.4) and (4.7), we could have another equation for t_{m2} as shown in Equation (C.8) (see Appendix C.2). Based on Equation (C.8), we get $t_{m2} \approx 3$ ms.

In sum, by using the estimated t_{m1} and t_{m2} in above, we obtain the approximations for the δV_{ax} and the h during a single action potential period ($t \in [0, T_{ax}^* = t_{m1} + t_{m2}]$) as

$$\delta V_{ax} = \begin{cases} \dfrac{E_{ax}^{Na,re} - V_{ax}^{re}}{t_{m1}} t, & t \in [0, t_{m1}], \\ E_{ax}^{Na,re} - V_{ax}^{re} - \dfrac{E_{ax}^{Na,re} - E_{ax}^{K,re}}{t_{m2}} (t - t_{m1}), & t \in [t_{m1}, T_{ax}^*]. \end{cases}$$

and

$$h^{dy}(t) = h_0 \exp\left(- \int_0^t \alpha_h(s) + \beta_h(s) ds \right) + \int_0^t \alpha_h(s) \exp\left(- \int_s^t \alpha_h(u) + \beta_h(u) du \right) ds,$$

where

$$\alpha_h = \frac{7}{100} \exp\left(-\frac{\delta V_{ax}}{20} \right), \quad \beta_h = \frac{1}{\exp\left(\frac{30 - \delta V_{ax}}{10}\right) + 1},$$

with the initial value h_0

$$h_0 = h^{re}(0) = \frac{\alpha_h(0)}{\alpha_h(0) + \beta_h(0)}.$$

By using Equation (4.1), we estimate the cumulative Na^+ flux through the axon membrane during a single action potential $[0, T_{ax}^*]$ by

$$\begin{aligned} \int_0^{T_{ax}^*} J_{ax}^{m,Na,dy} dt &\approx \int_0^{T_{ax}^*} \frac{\bar{g}^{Na} h^{dy} (m^{dy})^3}{z^{Na} e} \left(V_{ax}^{re} - E_{ax}^{Na,re} \right) + \frac{\bar{g}^{Na} h^{dy} (m^{dy})^3}{z^{Na} e} \delta V_{ax} dt \\ &\approx -2 \times 10^{-9} \text{ mol/m}^2. \end{aligned} \tag{4.8}$$

In the next step, we estimate the cumulative Cl^- flux through the axon membrane during a single action potential $[0, T_{ax}^*]$ by

$$\int_0^{T_{ax}^*} J_{ax}^{m,Cl,dy} dt \approx \int_0^{T_{ax}^*} \frac{g_{ax}^{Cl} \delta V_{ax}}{z^{Cl} e} dt \approx -3.7 \times 10^{-10} \text{ mol/m}^2. \tag{4.9}$$

In Equation (4.9), we use

$$I_{ax}^{Cl,dy} = g_{ax}^{Cl}\left(V_{ax}^{re} - E_{ax}^{Cl,re}\right) + g_{ax}^{Cl}\left(\delta V_{ax} - \delta E_{ax}^{Cl}\right) \approx g_{ax}^{Cl}\delta V_{ax},$$

since both $V_{ax}^{re} - E_{ax}^{Cl,re}$ and δE_{ax}^{Cl} are small in compare with δV_{ax}.

In the next, we provide the estimation of the cumulative K^+ flux through axon membrane during a single action potential. The governing equation of ϕ_{ax} yields

$$\sum_i z^i e \frac{\partial}{\partial z}\left(\eta_{ax} j_{ax}^i\right) = -\mathcal{M}_{ax}\left(I_{ax}^{Na,dy} + I_{ax}^{K,dy} + I_{ax}^{Cl,dy}\right). \tag{4.10}$$

At every location of the stimulated region, the time for a single action potential is T_{ax}^*. We introduce T_{all}^* for the electrical signal propagation time, during which the signal propagates from one end of the axon (near the the optic nerve head) to the other end (far-eye-side of the optic nerve) as shown in Figure B.1. By integrating right-hand side of Equation (4.10) over space $[0, L]$ and time $[0, T_{all}^*]$, we have

$$-\mathcal{M}_{ax}\int_0^{T_{all}^*}\int_0^L I_{ax}^{Na,dy} + I_{ax}^{K,dy} + I_{ax}^{Cl,dy} dz dt \approx -\mathcal{M}_{ax} L \int_0^{T_{ax}^*} I_{ax}^{Na,dy} + I_{ax}^{K,dy} + I_{ax}^{Cl,dy} dt. \tag{4.11}$$

where we use the propagation property of the action potential along z direction, and only the axon firing period is taken into consideration. By integrating the left-hand side of Equation (4.10), we get

$$\int_0^{T_{all}^*}\int_0^L \sum_i z^i e \frac{\partial}{\partial z}\left(\eta_{ax} j_{ax}^i\right) dz dt = O\left(T_{all}^* e \eta_{ax} j_{ax}^{bd*}\right). \tag{4.12}$$

We assume that the characteristic time scale of T_{all}^* equals $O(10^{-3})$. The scale of ion flux j_{ax}^{bd} at left and right boundaries ($z = 0, L$) is dominated by the diffusion term

$$j_{ax}^{bd*} = O\left(D_{ax}^* \frac{\delta c_{ax}^*}{z^*}\right),$$

since the boundary conditions are $\frac{\partial \phi_{ax}}{\partial z}\big|_{z=0,L} = 0$ and $u_{ax}(0) = u_{ax}(L) = 0$. δc_{ax}^* is the characteristic difference between ion concentration at boundary value and the ion concentration inside the axon after a single action potential. Based on the Na^+ flux estimation in Equation (4.8), we estimate $\delta c_{ax}^* = O(10^{-1})$. From Equations (4.8) and (4.9), we get the following order of the cumulative fluxes through axon membrane during a single action potential time interval

$$O\left(T_{all}^* \eta_{ax} j_{ax}^{bd*}\right) \ll O\left(\mathcal{M}_{ax} L \left|\int_0^{T_{ax}^*} J_{ax}^{m,Cl,dy} dt\right|\right) \ll O\left(\mathcal{M}_{ax} L \left|\int_0^{T_{ax}^*} J_{ax}^{m,Na,dy} dt\right|\right). \tag{4.13}$$

In other words, based on Equations (4.11), (4.12) and (4.13), it yields

$$O\left(\left|\int_0^{T_{ax}^*} J_{ax}^{m,K,dy} dt\right|\right) = O\left(\left|\int_0^{T_{ax}^*} J_{ax}^{m,Na,dy} dt\right|\right). \tag{4.14}$$

Therefore, based on Equation (4.8), we estimate the cumulative axon transmembrane K^+ flux during a single action potential should be

$$\int_0^{T_{ax}^*} J_{ax}^{m,K,dy} dt \approx 2 \times 10^{-9} \text{ mol/m}^2. \tag{4.15}$$

where $[0, T_{ax}^*]$ is the time interval enclosing a single action potential.

Remark 4.1. Equation (4.14) shows that for a single action potential, the leading order of the cumulative K^+ flux out of the axon to the extracellular space equals the leading order of the cumulative Na^+ flux into the axon from the extracellular space. This estimation is consistent with observations in the literature [53, 79, 80].

Next, we estimate the concentration variation in the stimulated extracellular region due to a single action potential. Since the time scale of T_{ax}^* is in milliseconds, the cumulative ion fluxes through axon transmembrane are the main source changes the ion concentration in the stimulated extracellular region,

$$\eta_{ex} \delta c_{ex}^i = \mathcal{M}_{ax} \int_0^{T_{ax}^*} J_{ax}^{m,i,dy} dt, \quad i = \text{Na}^+, \text{K}^+, \tag{4.16}$$

where δc_{ex}^i is the ith ion's concentration variation from its resting state.
Based on Equations (4.14) and (4.16), the absolute variation of Na^+ and K^+ concentrations in the stimulated extracellular region due to action potentials, can be written as

$$\delta c_{sti} = O\left(\frac{\mathcal{M}_{ax}}{\eta_{ex}} \left| \int_0^{T_{ax}^*} J_{ax}^{m,i,dy} dt \right| \right), \ i = \text{Na}^+, \text{K}^+. \tag{4.17}$$

In the later discussion, we use δc_{sti} to describe the amount of ion concentration changes in the stimulated extracellular region after a single action potential.

4.1.2 Estimation of glial transmembrane K^+ flux

In this section, we estimate the glial transmembrane current when the K^+ and the Na^+ concentration vary by δc_{sti} in the stimulated extracellular region. We also find that the electric field ϕ_{gl} responds immediately to the glial K^+ Nernst potential changes. In the stimulated region, the variation of extracellular electric potential $\delta\phi_{ex}$ is small in compare to the variation of glial electric potential $\delta\phi_{gl}$.

The dominant current through the glial membrane in the stimulated region is through the passive K^+ channel, rather than the Na^+ channel or the Na/K pump. Simultaneously, in the non-stimulated extracellular region, almost the same amount of K^+ moves from the glial compartment to extracellular space. In other words, both the glial cells and extracellular space in the non-stimulated region participate in the spatial buffering process to help potassium clearance [81, 82].

In the stimulated region, the Nernst potential for K^+ across the glial membrane changes because of the additional potassium δc_{ex}^K in the extracellular space,

$$\delta E_{gl}^K = \frac{k_B T}{z^K e}\left(\log\left(1+\frac{\delta c_{ex}^K}{c_{ex}^{K,re}}\right)-\log\left(1+\frac{\delta c_{gl}^K}{c_{gl}^{K,re}}\right)\right), \tag{4.18}$$

where $\delta c_l^K, l = gl, ex$ are the variations of concentrations in the l compartment. The variation of K^+ concentration in the glial compartment δc_{gl}^K is a result of the δc_{ex}^K produced by the glial transmembrane K^+ flux. Recall that the volume fraction (η_{gl}) of the glial compartment is much larger than the extracellular space (η_{ex}). At same time, based on Equation (4.17) and K^+ concentration at resting state, we get

$$\delta c_{ex}^K = o\left(c_{ex}^{K,re}\right), \quad \frac{\delta c_{gl}^K}{c_{gl}^{K,re}} = o\left(\frac{\delta c_{ex}^K}{c_{ex}^{K,re}}\right).$$

Therefore, δE_{gl}^K in Equation (4.18) can be approximated by its Taylor expansion,

$$\delta E_{gl}^K \approx \frac{k_B T}{z^K e}\frac{\delta c_{ex}^K}{c_{ex}^{K,re}}. \tag{4.19}$$

The variation of K^+ Nernst potential in the stimulated region produces the changes of glial membrane potential V_{gl} and glial compartment electric potential ϕ_{gl}. We move on now to estimate the variations of electric potentials in the stimulated extracellular and glial regions.
From the governing equation for ϕ_{ex},

$$\sum_i z^i e \nabla\cdot\left(\eta_{ex}\boldsymbol{j}_{ex}^i\right) = \sum_i z^i e \mathcal{M}_{gl}\left(J_{p,gl}^i + J_{c,gl}^i\right) + \sum_i z^i e \mathcal{M}_{ax}\left(J_{p,ax}^i + J_{c,ax}^i\right), \tag{4.20}$$

where

$$\boldsymbol{j}_{ex}^i = c_{ex}^i \boldsymbol{u}_{ex} - D_{ex}^i \tau_{ex}\left(\nabla c_{ex}^i + \frac{z^i e}{k_B T} c_{ex}^i \nabla\phi_{ex}\right).$$

We claim that after the axon stops firing, the major current is through glial membrane K^+ channels (see Appendix C.3). Therefore, the right-hand side of Equation (4.20) can be approximated as

$$\sum_i z^i e \mathcal{M}_{gl}\left(J_{p,gl}^i + J_{c,gl}^i\right) + \sum_i z^i e \mathcal{M}_{ax}\left(J_{p,ax}^i + J_{c,ax}^i\right) \approx \mathcal{M}_{gl} g_{gl}^K\left(\delta V_{gl} - \delta E_{gl}^K\right). \tag{4.21}$$

Next, we integrate Equation (4.20) over the stimulated region $V_S = \{(r,z,\theta)|r\in[0,r_{sti}],\ z\in[0,L],\ \theta\in[0,2\pi]\}$, through which the action potential propagates as shown in Figure 4.1. By Equation (4.21), we have the approximation of the total current (over the glial membrane area) is

$$\int_{V_S} \mathcal{M}_{gl} g_{gl}^K\left(\delta V_{gl} - \delta E_{gl}^K\right) dv \approx \pi r_{sti}^2 L \mathcal{M}_{gl} g_{gl}^K\left(\delta V_{gl} - \delta E_{gl}^K\right). \tag{4.22}$$

In the left-hand side of Equation (4.20), by the charge neutrality assumption in Equation (3.1), we naturally have

$$\sum_i z^i e c_{ex}^i \boldsymbol{u}_{ex} = 0. \tag{4.23}$$

Based on Equations (4.9), (4.14) and (4.17), we know that after a single action potential the leading order of ion concentration variations in the stimulated extracellular region are as follows

$$\delta c_{ex}^{Na} = -\delta c_{sti}, \quad \delta c_{ex}^{K} = \delta c_{sti}, \quad \delta c_{ex}^{Cl} = o\left(\delta c_{sti}\right). \tag{4.24}$$

Using Equations (3.15) and (4.24), the diffusion term in left-hand side of Equation (4.20) can be approximated as

$$-\int_{V_S} \sum_i z^i e \nabla \cdot \left(\eta_{ex} D_{ex}^i \tau_{ex} \nabla c_{ex}^i\right) dv \approx 2\pi r_{sti} L e \eta_{ex} D_{ex}^{\text{diff}} \tau_{ex} \frac{\delta c_{sti}}{r^*}, \tag{4.25}$$

where $D_{ex}^{\text{diff}} = D_{ex}^K - D_{ex}^{Na}$.
In Equation (4.25), we claim that the currents through the left ($z = 0$) and right ($z = L$) boundaries of the stimulated region V_S is much smaller than those through the radial transition region S_T. This is because (1) the ion concentration variations are in radial direction (between stimulated region and non-stimulated region) and (2) the length scales in the z and r direction are different. Therefore, the radial transition region $S_T = \partial V_S^r = \{(r, z, \theta) | r = r_{sti}, z \in [0, L], \theta \in [0, 2\pi]\}$ has much larger area than the left and right boundaries of V_S,

$$\frac{\partial V_S^z}{\partial V_S^r} = \frac{r_{sti}}{2L} = O\left(10^{-3}\right).$$

Similarly, the integration of the electric drift term in left-hand side of Equation (4.20) yields the approximation,

$$-\int_{V_S} \sum_i z^i e \nabla \cdot \left(\eta_{ex} D_{ex}^i \tau_{ex} \frac{z^i e}{k_B T} c_{ex}^i \nabla \phi_{ex}\right) dv \approx 2\pi r_{sti} L \eta_{ex} \sigma_{ex} \frac{\delta \phi_{ex}}{r^*}, \tag{4.26}$$

where $\sigma_{ex} = \frac{\tau_{ex} e^2}{k_B T} \sum_i (z^i)^2 D_{ex}^i c_{ex}^i$.
From Equations (4.22), (4.25) and (4.26), we get

$$\frac{2}{r_{sti}} \left(\frac{\eta_{ex} \tau_{ex} e D_{ex}^{\text{diff}}}{\mathcal{M}_{gl}} \frac{\delta c_{sti}}{r^*} + \frac{\eta_{ex} \sigma_{ex}}{\mathcal{M}_{gl}} \frac{\delta \phi_{ex}}{r^*}\right) \approx g_{gl}^K \left(\delta V_{gl} - \delta E_{gl}^K\right). \tag{4.27}$$

At the same time, from the governing equation of ϕ_{gl}

$$\sum_i z^i e \nabla \cdot \left(\eta_{gl} \boldsymbol{j}_{gl}^i\right) = -\sum_i z^i e \mathcal{M}_{gl} \left(J_{p,gl}^i + J_{c,gl}^i\right), \tag{4.28}$$

where

$$\boldsymbol{j}_{gl}^i = c_{gl}^i \boldsymbol{u}_{gl} - D_{gl}^i \tau_{gl} \left(\nabla c_{gl}^i + \frac{z^i e}{k_B T} c_{gl}^i \nabla \phi_{gl}\right),$$

we obtain the following estimation in a similar way

$$-\frac{2}{r_{sti}}\frac{\eta_{gl}\sigma_{gl}}{\mathcal{M}_{gl}}\frac{\delta\phi_{gl}}{r^*} \approx g_{gl}^K\left(\delta V_{gl} - \delta E_{gl}^K\right), \tag{4.29}$$

where $\sigma_{gl} = \frac{\tau_{gl}e^2}{k_BT}\sum_i (z^i)^2 D_{gl}^i c_{gl}^i$.
Here, we neglect the diffusion and convection terms in Equation (4.28) because these terms require much longer time to respond to the extracellular concentration change. Based on Equation (4.27) and Equation (4.29), we get

$$\delta\phi_{ex} = -\frac{\eta_{gl}\sigma_{gl}}{\eta_{ex}\sigma_{ex}}\delta\phi_{gl} - \frac{\tau_{ex}eD_{ex}^{\text{diff}}}{\sigma_{ex}}\delta c_{sti}. \tag{4.30}$$

In Appendix C.4, by matching the orders in both side of Equation (4.29), we claim that $\delta\phi_{ex} = o\left(\delta\phi_{gl}\right)$ in the stimulated region and therefore,

$$\delta V_{gl} = \delta\phi_{gl} - \delta\phi_{ex} = O(\delta\phi_{gl}). \tag{4.31}$$

In the next step, we approximate the K^+ current through the leaking K^+ channel on the glial membrane. Based on Equations (4.29) and (4.31), we get

$$g_{gl}^K\left(\delta\phi_{gl} - \delta E_{gl}^K\right) \approx g_{gl}^K\left(\delta V_{gl} - \delta E_{gl}^K\right) \approx -\frac{2\eta_{gl}\sigma_{gl}}{r_{sti}\mathcal{M}_{gl}}\frac{\delta\phi_{gl}}{r^*}. \tag{4.32}$$

Hence, by Equation (4.32), we obtain the relation between δE_{gl}^K and $\delta\phi_{gl}$ as

$$\delta E_{gl}^K \approx \left(1 + h_\epsilon\right)\delta\phi_{gl}, \tag{4.33}$$

where

$$h_\epsilon = \frac{2\eta_{gl}\sigma_{gl}}{r_{sti}\mathcal{M}_{gl}r^* g_{gl}^K}.$$

Based on Equation (4.32), it gives us the following approximation

$$g_{gl}^K\left(\delta V_{gl} - \delta E_{gl}^K\right) \approx -\frac{g_{gl}^K h_\epsilon}{1 + h_\epsilon}\delta E_{gl}^K. \tag{4.34}$$

Furthermore, from Equations (4.30), (4.33) and (4.19), we get the approximation

$$\delta\phi_{ex} \approx -\frac{\eta_{gl}\sigma_{gl}k_BT}{\eta_{ex}\sigma_{ex}\left(1 + h_\epsilon\right)z^K e}\frac{\delta c_{ex}^K}{c_{ex}^{K,re}}. \tag{4.35}$$

The variations of electric field $\delta\phi_{gl}$ in both stimulated and non-stimulated regions are produced without delay by δE_{gl}^K in the stimulated region, as described in the governing equation of ϕ_{gl} in Equation (3.13).

The K^+ leaking current is the major current through the glial membrane in the non-stimulated region as it is in the stimulated region because the current through the ion channel is voltage ϕ_{gl} dependent and K^+ conductance is one dominant ion conductance in the glial membrane

$$g_{gl}^i = o\left(g_{gl}^K\right), \quad i = \mathrm{Na}^+, \mathrm{Cl}^-.$$

In the next steps, we introduce the superscript notation 'S' for the stimulated region variables and superscript 'NS' for non-stimulated region ones. For the glial transmembrane currents, we have the following approximation

$$\sum_i z^i e \mathcal{M}_{gl} \left(J_{p,gl}^{S,i} + J_{c,gl}^{S,i}\right) \approx \mathcal{M}_{gl} g_{gl}^K \left(\delta V_{gl}^S - \delta E_{gl}^{S,K}\right),$$
$$\sum_i z^i e \mathcal{M}_{gl} \left(J_{p,gl}^{NS,i} + J_{c,gl}^{NS,i}\right) \approx \mathcal{M}_{gl} g_{gl}^K \left(\delta V_{gl}^{NS} - \delta E_{gl}^{NS,K}\right).$$

By integration of the ϕ_{gl} Equation (3.13) over the stimulated region V_S and the non-stimulated region V_{NS} respectively, it yields

$$\begin{cases} \displaystyle\int_{V_S} \sum_i z^i \mathrm{e} \nabla \cdot \left(\eta_{gl}^S \boldsymbol{j}_{gl}^{S,i}\right) dv \approx \int_{V_S} \mathcal{M}_{gl} g_{gl}^K \left(\delta V_{gl}^S - \delta E_{gl}^{S,K}\right), \\ \displaystyle\int_{V_{NS}} \sum_i z^i \mathrm{e} \nabla \cdot \left(\eta_{gl}^{NS} \boldsymbol{j}_{gl}^{NS,i}\right) dv \approx \int_{V_{NS}} \mathcal{M}_{gl} g_{gl}^K \left(\delta V_{gl}^{NS} - \delta E_{gl}^{NS,K}\right). \end{cases} \tag{4.36}$$

Most of the current between region V_S and region V_{NS} goes through the radial transition region S_T. By Equation (4.36) and boundary conditions for ϕ_{gl} we obtain

$$\int_{V_S} \mathcal{M}_{gl} g_{gl}^K \left(\delta V_{gl}^S - \delta E_{gl}^{S,K}\right) dv \approx -\int_{V_{NS}} \mathcal{M}_{gl} g_{gl}^K \left(\delta V_{gl}^{NS} - \delta E_{gl}^{NS,K}\right) dv. \tag{4.37}$$

Based on Equation (4.37), the average K^+ flux through the glial membrane in the non-stimulated region leaks out to extracellular space with an approximate strength

$$\frac{g_{gl}^K}{z^K e} \left(\delta V_{gl}^{NS} - \delta E_{gl}^{NS,K}\right) = -\frac{r_{sti}^2}{r^{*2} - r_{sti}^2} \frac{g_{gl}^K}{z^K e} \left(\delta V_{gl}^S - \delta E_{gl}^{S,K}\right). \tag{4.38}$$

In summary, Equation (4.37) and Equation (4.38), show how the glial compartment in the non-stimulated region serve as spatial buffers and help clear potassium from the extracellular space outside the stimulated axons [52].

Remark 4.2. The glial compartment serves as an important and quick potassium transport device to remove accumulated potassium in the extracellular space during the axon firing.

In the stimulated region, the potassium Nernst potential change makes the glial membrane potential more positive and moves potassium through ion channels into the glial compartment. In the non-stimulated region, since glia is an electrical syncytium, the glial membrane potential also simultaneously increases. However, the glia potassium Nernst potential

in the non-stimulated region is not very different from its resting state. These potentials produce the outward potassium flux from the glial compartment in the non-stimulated region.

Interacting regions of this sort depend on spatial variables and the properties of the glia as a syncytium (see Figure 4.9c). It is difficult to capture these effects in models that do not include space as an independent variable.

These effects make our spatial model quite different from the existing ODE models [53, 83] since those ODE models either take the extracellular ion concentration as constant or they do not consider the ion exchange between the extracellular space at all. In recent work, Marte J. et al. [84] introduce a compartment model similar to Equation (4.39) by considering ion flux between neuron, glia, and extracellular regions in both the dendrite and soma region. It is always possible to take a field theory and approximate its x dependence into compartments. Nevertheless, it is quite challenging to know how to describe the parameter dependence and compartment inter-dependence consistently in compartment models. It is even harder to describe results over a range of conditions or sizes of structures. The usual result is that parameters in compartment models have to be changed as interactions, conditions, sizes change. Different investigators choose different representations for their compartment models, and it becomes difficult to make progress in understanding mechanisms. Using a theory with the spatial and time dependence of field equations lessens these difficulties since there is no freedom in the choice of conservation laws and little in their numerical analysis or approximation, if systematic methods of perturbation theory are used as we do here.

4.1.3 The circulation of water flow

In this section, we discuss water circulation between the stimulated and the non-stimulated regions. As extra K^+ is gradually cleared, it produces an osmotic pressure difference between the intra- and inter- domain, i.e., between the inside the glial compartment and the extracellular space. This osmotic pressure variation drives transmembrane water flow and water circulation in the optic nerve.

Now we consider a train of stimulus stimulated with the frequency f_m $(= \frac{1}{T})$ in the axon region $(r < r_{sti}, z = z_0)$ during time $[0, T_{sti}]$. Our estimation depends on the K^+ and Na^+ concentration variations in the extracellular space and charge neutrality condition. The clearance of extra amount of K^+ (δc^K_{ex}) in the stimulated extracellular space mostly goes through glial membrane and extracellular pathway (see Appendix C.5),

$$\frac{d\left(\eta_{ex}\delta c^K_{ex}\right)}{dt} = -\left(\lambda^{m,K}_{gl} + \lambda^K_{ex}\right)\delta c^K_{ex}, \tag{4.39}$$

where

$$\lambda^{m,K}_{gl} = \frac{\mathcal{M}_{gl} g^K_{gl} h_\epsilon k_B T}{z^K\left(1+h_\epsilon\right) e^2 c^{K,re}_{ex}}, \quad \lambda^K_{ex} = \frac{2\eta_{ex} D^K_{ex}\tau_{ex}}{r_{sti} r^*}.$$

The $\lambda^{m,K}_{gl}$ presents the effect of glial transmembrane K^+ flux and the λ^K_{ex} describes the spatial effect of the extracellular K^+ transport between the stimulated region and non-stimulated

region. This spatial communication is not negligible since λ_{ex}^{K} is comparable magnitude to the $\lambda_{gl}^{m,K}$ (see Figure 5.1). We start with the first stimulus on axon, so the initial condition in Equation (4.39) is

$$\delta c_{ex}^{K}(0) = \delta c_{sti},$$

and at the beginning of each period T, there is an additional δc_{sti} amount of K^+ accumulated in the extracellular space due to the axon firing

$$\delta c_{ex}^{K}(iT) = \delta c_{ex}^{K}(iT) + \delta c_{sti}, \quad i = 1 \dots n-1,$$

where $n \left(= \frac{T_{sti}}{f_m}\right)$ is the total number of periods. In the above setting, we see that the extracellular K^+ concentration immediately changes due to axon firing.
The time course of Na^+ variation (δc_{ex}^{Na}) in the stimulated extracellular space is (see Appendix C.5)

$$\frac{d\left(\eta_{ex}\delta c_{ex}^{Na}\right)}{dt} = -\lambda_{ex}^{Na,1}\delta c_{ex}^{Na} + \lambda_{ex}^{Na,2}\delta c_{ex}^{K}, \tag{4.40}$$

with the initial condition

$$\delta c_{ex}^{Na}(0) = -\delta c_{sti}.$$

There is δc_{sti} amount of Na^+ flux into axon compartment from the extracellular space at the beginning of each period T

$$\delta c_{ex}^{Na}(iT) = \delta c_{ex}^{Na}(iT) - \delta c_{sti}, \quad i = 1 \dots n-1.$$

The $\lambda_{ex}^{Na,1}$ describes the effect of extracellular diffusion and $\lambda_{ex}^{Na,2}$ presents the extracellular electric drift between stimulated and non-stimulated regions. In Equation (4.40), we have

$$\lambda_{ex}^{Na,1} = \frac{2\eta_{ex}D_{ex}^{Na}\tau_{ex}}{r_{sti}r^*}, \quad \lambda_{ex}^{Na,2} = \frac{2\eta_{gl}\sigma_{gl}D_{ex}^{Na}\tau_{ex}c_{ex}^{Na,re}}{r_{sti}\sigma_{ex}\left(1+h_\epsilon\right)r^* c_{ex}^{K,re}}.$$

In Appendix C.5, we present the solution of the coupled linear system of (4.39) and (4.40). By the charge neutrality condition Equation (3.1), the variation of extracellular osmotic concentration is

$$\delta O_{ex} = 2\left(\delta c_{ex}^{K} + \delta c_{ex}^{Na}\right), \tag{4.41}$$

where δc_{ex}^{K} and δc_{ex}^{Na} are written in Equations (C.29) and (C.30).
Notice that sodium and potassium behave differently in the extracellular space. In the extracellular space, the electric drift K^+ flux has a much smaller magnitude in comparison to diffusive K^+ flux, since the scale ratio R_{ex}^{K} between the electric drift term and diffusion term for K^+ is (see Appendix C.5)

$$R_{ex}^{K} = \frac{\eta_{gl}\sigma_{gl}}{\eta_{ex}\sigma_{ex}(1+h_\epsilon)} = o(1). \tag{4.42}$$

However, for Na^+ in the extracellular space, the magnitude of electric drift flux are comparable to diffusive flux since (see Appendix C.5)

$$R_{ex}^{Na} = \frac{\eta_{gl}\sigma_{gl}}{\eta_{ex}\sigma_{ex}\left(1+h_\epsilon\right)}\frac{c_{ex}^{Na}}{c_{ex}^{K}} = O(1). \tag{4.43}$$

In the next discussion, we estimate the scales of the glial transmembrane velocity, glial radial velocity, and extracellular radial velocity. The variation in osmotic pressure in the stimulated region is the driving force for the water flow and circulation. Our estimation is based on the equations governing fluid flow and the spatial variation of osmotic pressure.

From the conservation of mass in glial compartment, we have

$$\frac{\partial \eta_{gl}}{\partial t} + \mathcal{M}_{gl}L_{gl}^{m}\left(p_{gl} - p_{ex} - \gamma_{gl}k_BT\left(O_{gl} - O_{ex}\right)\right) + \nabla\cdot\left(\eta_{gl}\boldsymbol{u}_{gl}\right) = 0. \tag{4.44}$$

Based on Equation (4.41), at $t = T_{sti}$, we know there is cumulative osmosis variation $\delta O_{ex}(T_{sti})$ in the stimulated extracellular region. Since the glial compartment volume fraction (η_{gl}) is larger than the extracellular volume fraction (η_{ex}), so we naturally get

$$|\delta O_{gl}| < |\delta O_{ex}|.$$

Therefore, we view the $k_BT\delta O_{ex}$ as the dominated osmotic pressure variation. At the resting state, Equation (4.44) yields

$$\mathcal{M}_{gl}L_{gl}^{m}\left(p_{gl}^{re} - p_{ex}^{re} - \gamma_{gl}k_BT\left(O_{gl}^{re} - O_{ex}^{re}\right)\right) + \nabla\cdot\left(\eta_{gl}^{re}\boldsymbol{u}_{gl}^{re}\right) = 0,$$

and by Equation (4.44), we get

$$\frac{\partial \delta\eta_{gl}}{\partial t} + \mathcal{M}_{gl}L_{gl}^{m}\left(\delta p_{gl} - \delta p_{ex} - \gamma_{gl}k_BT\left(\delta O_{gl} - \delta O_{ex}\right)\right) + \nabla\cdot\left(\delta\left(\eta_{gl}\boldsymbol{u}_{gl}\right)\right) = 0. \tag{4.45}$$

In Equation (4.45), the scale of the second term is much larger than the third term, since

$$\frac{\eta_{gl}\kappa_{gl}\tau_{gl}}{\mu(r^*)^2} = o\left(\mathcal{M}_{gl}L_{gl}^{m}\right).$$

Therefore, Equation (4.45) in the stimulated glial region can be approximated as

$$\frac{\partial\left(\delta p_{gl} - \delta p_{ex}\right)}{K_{gl}\partial t} + \mathcal{M}_{gl}L_{gl}^{m}\left(\delta p_{gl} - \delta p_{ex}\right) + \mathcal{M}_{gl}L_{gl}^{m}\gamma_{gl}k_BT\delta O_{ex} = 0, \tag{4.46}$$

with the initial condition

$$\delta\eta_{gl}(0) = \frac{\delta p_{gl}(0) - \delta p_{ex}(0)}{K_{gl}} = 0.$$

In Equation (4.46), we have used the relationship between hydraulic pressures $p_l,\ l = gl, ex$ and glial compartment volume fraction η_{gl} in Equation (3.4)

$$K_{gl}\delta\eta_{gl} = \delta p_{gl} - \delta p_{ex}. \tag{4.47}$$

By using a linear approximation of extracellular osmotic concentration variation δO_{ex}

$$\delta O_{ex}(t) = \frac{\delta O_{ex}(T_{sti})}{T_{sti}} t, \quad t \in [0, T_{sti}],$$

the solution of $\delta\left(p_{gl} - p_{ex}\right)$ in Equation (4.46) has the analytic expression.
Hence, we estimate the average glial transmembrane water velocity in the stimulated region as

$$U_{gl}^{m}(t) = L_{gl}^{m}\left(\delta p_{gl}(t) - \delta p_{ex}(t) + \gamma_{gl} k_B T \delta O_{ex}(t)\right), \tag{4.48}$$

and we estimate the scale of glial transmembrane velocity in the stimulated region as

$$U_{gl}^{m*} = \left|U_{gl}^{m}(T_{sti})\right|. \tag{4.49}$$

In Equation (4.48), the hydrostatic pressure variations $\delta p_l, l = gl, ex$ passively react to the osmotic pressure variation $k_B T \cdot \delta O_{ex}$ in the stimulated region. Therefore, the direction of this glial transmembrane water flow is determined by osmotic pressure variation $k_B T \cdot \delta O_{ex}$.

In the next step, we estimate the glial radial velocity scale u_{gl}^{r*} and extracellular radial velocity scale u_{ex}^{r*}. By the incompressibility condition, we have

$$\nabla \cdot (\eta_{gl} \boldsymbol{u}_{gl}) + \nabla \cdot (\eta_{ex} \boldsymbol{u}_{ex}) + \frac{\partial\left(\eta_{ax} u_{ax}^{z}\right)}{\partial z} = 0. \tag{4.50}$$

In Equation (4.50), the dominant terms are the gradients in radial direction, because the length scale difference between r^* and z^* and the osmotic pressure variation are both in the radial direction. Therefore, Equation (4.50) can be approximated by

$$\frac{\partial\left(\eta_{gl} u_{gl}^{r}\right)}{\partial r} + \frac{\partial\left(\eta_{ex} u_{ex}^{r}\right)}{\partial r} = 0, \tag{4.51}$$

The velocity boundary conditions at $r = 0$,

$$u_{gl}^{r} = u_{ex}^{r} = 0,$$

and Equation (4.51) yield

$$\eta_{gl} u_{gl}^{r} + \eta_{ex} u_{ex}^{r} = 0. \tag{4.52}$$

Furthermore, by Equation (4.52), the radial velocity scale (u_{ex}^{r*}) in the extracellular space is naturally given by

$$u_{ex}^{r*} = \frac{\eta_{gl}}{\eta_{ex}} u_{gl}^{r*}. \tag{4.53}$$

With the help of Equation (4.52), we can rewrite u_{gl}^{r} in form of

$$u_{gl}^{r} = (1 - \chi) u_{gl}^{r} - \chi \frac{\eta_{ex}}{\eta_{gl}} u_{ex}^{r}, \tag{4.54}$$

where the χ is defined as

$$\chi = \frac{\kappa_{gl}\tau_{gl}}{\frac{\eta_{ex}}{\eta_{gl}}\kappa_{ex}\tau_{ex} + \kappa_{gl}\tau_{gl}}.$$

By substituting Equations (3.5), (3.7) into Equation (4.54), we estimate the radial velocity scale in the glial compartment as

$$u_{gl}^{r*} = \left|(1-\chi)\frac{\kappa_{gl}\tau_{gl}}{\mu}\frac{\delta p_{gl} - \delta p_{ex}}{r^*} - (1-\chi)\frac{\kappa_{gl}\tau_{gl}}{\mu}\gamma_{gl}k_B T\frac{\delta O_{gl}}{r^*} - \chi\frac{\eta_{ex}}{\eta_{gl}}k_e\tau_{ex}\frac{\delta\phi_{ex}}{r^*}\right|_{t=T_{sti}} \tag{4.55}$$

In Equation (4.55), the δO_{gl} is due to the changes of the volume fraction ($\delta\eta_{gl}$) of the glial compartment can be estimated as

$$\delta O_{gl} \approx \frac{\eta_{gl}^{re}}{\eta_{gl}^{re} + \delta\eta_{gl}}O_{gl}^{re} - O_{gl}^{re} = -\frac{\delta\eta_{gl}}{\eta_{gl}^{re} + \delta\eta_{gl}}O_{gl}^{re},$$

where $\delta\eta_{gl}$ can be written by using the δp_l as in Equation (4.47)

$$\delta\eta_{gl} = \frac{\delta p_{gl} - \delta p_{ex}}{K_{gl}}.$$

4.1.4 The relative importance of ion flux components

In this section, we discuss the relative importance of ion flux components, due to diffusion, convection, and electric drift in the glial and extracellular regions, respectively. Our discussion focuses on the radial direction since these are the dominant fluxes.

In the extracellular space, we characterize the relative importance between electric drift and diffusion in radial direction by the ratios R_{ex}^K and R_{ex}^{Na} analyzed in Equation (4.42) and Equation (4.43)

$$R_{ex}^K = \left|\frac{\eta_{gl}\sigma_{gl}}{\eta_{ex}\sigma_{ex}\left(1+h_\epsilon\right)}\right|, \quad R_{ex}^{Na} = \left|\frac{\eta_{gl}\sigma_{gl}}{\eta_{ex}\sigma_{ex}\left(1+h_\epsilon\right)}\frac{c_{ex}^{Na}}{c_{ex}^K}\right|.$$

For Na^+ and K^+, the ratio between convection and diffusion in the extracellular space is estimated by the Peclet number

$$Pe_{ex}^i = \left|\frac{c_{ex}^i u_{ex}^{r*} r^*}{D_{ex}^i\tau_{ex}\delta c_{ex}^i}\right|, \quad i = \mathrm{Na}^+, \mathrm{K}^+, \tag{4.56}$$

where we approximate radial diffusion flux scale in the extracellular space as

$$\left|D_{ex}^*\tau_{ex}\frac{\delta c_{ex}^i}{r^*}\right|, \quad i = \mathrm{Na}^+, \mathrm{K}^+.$$

In a similar way, we estimate the Peclet numbers in the glial compartment as

$$Pe_{gl}^i = \left|\frac{c_{gl}^i u_{gl}^{r*} r^*}{D_{gl}^*\tau_{gl}\delta c_{gl}^i}\right|, \quad i = \mathrm{Na}^+, \mathrm{K}^+. \tag{4.57}$$

Note that the Peclet numbers for Na^+ and K^+ are significantly different due to their different concentrations as shown in Equations (4.56) and (4.57). Our Peclet numbers depend on the ion type, the ion concentration and the domain in which they are evaluated.
In the glial compartment, the ratio between electric drift and diffusion is

$$R_{gl}^K = \left| \frac{1}{1+h_\epsilon} \frac{c_{gl}^K \delta c_{ex}^K}{c_{ex}^K \delta c_{gl}^K} \right|, \quad R_{gl}^{Na} = \left| \frac{1}{1+h_\epsilon} \frac{c_{gl}^{Na} \delta c_{ex}^K}{c_{ex}^K \delta c_{gl}^{Na}} \right|. \tag{4.58}$$

where we have used Equations (4.19) and (4.33).
In Equation (4.58), we can estimate the K^+ concentration change (δc_{gl}^K) in the stimulated glial compartment as

$$\delta c_{gl}^K \approx \left(n c_{sti} - \delta c_{ex}^K \right) \frac{\lambda_{gl}^{m,K}}{\lambda_{gl}^{m,K} + \lambda_{ex}^K} \frac{\eta_{ex}}{\eta_{gl}}, \tag{4.59}$$

where $\lambda_{gl}^{m,K}$ and λ_{ex}^K are defined in Equation (4.39), and n is the number of stimuli.
We estimate the δc_{gl}^{Na} in the stimulated glial compartment as

$$\delta c_{gl}^{Na} \approx -\frac{3\delta I_{gl}}{g_{gl}^K \left(\delta V_{gl} - \delta E_{gl}^K \right)} \delta c_{gl}^K. \tag{4.60}$$

where δI_{gl} are approximated by Taylor expansion as

$$\delta I_{gl} \approx 2 \left(\frac{\mathrm{K_{K1}} I_{gl}^{re,1}}{c_{ex}^{K,re} \left(c_{ex}^{K,re} + K_{K1} \right)} + \frac{\mathrm{K_{K2}} I_{gl}^{re,2}}{c_{ex}^{K,re} \left(c_{ex}^{K,re} + K_{K2} \right)} \right) \delta c_{ex}^K.$$

In the next section, we carry out numerical simulations to validate the estimations above. We follow our plan of using perturbation expansions to evaluate the dominant term, and numerical analysis to study the error in the dominant terms. We are careful to evaluate the error in important conditions, not just one condition. Furthermore, we compare the results of the electrodiffusion model with the convection-electrodiffusion (full) model to show the effect of water flow on the ion transport.

4.2 Numerical simulation

We use numerical analysis to compute exact results of our full set of field equations, using a range of numerical methods appropriate for each situation. We are careful to check the validity of the numerical method with the usual checks of robustness, accuracy in reduced situations, etc. The numerical methods can never show how results (e.g., water flows, potassium clearance, etc.) depend qualitatively on parameters. We determine these crucial biological properties by an analytical perturbation analysis and use the numerical solutions to evaluate the approximation in the analytical result.

In this section, we apply a train of stimuli to stimulate the axon membrane near the left boundary ($\{(z_0, r)|z_0 = 1.875$ mm and $r < r_{sti} = \frac{1}{2}r^* = 24\ \mu$m$\}$). Each single stimulus has current strength $I_{sti} = 3 \times 10^{-3}$ A/m^2 with duration 3 ms. The frequency of the stimuli is 50 Hz ($T = 0.02$ s) and the duration is $T_{sti} = 0.2$ s.

4.2.1 Estimation of velocity scales

We first estimate how large are the fluid velocities in extracellular space and glial compartment generated by a train of stimuli. From Equations (C.30) and (C.29), the estimated concentration variations in the stimulated extracellular region at $t = T_{sti}$ are

$$\delta c_{ex}^{Na} \approx -1.06 \text{ mM}, \quad \delta c_{ex}^{K} \approx 0.89 \text{ mM}, \quad \delta O_{ex} \approx -0.34 \text{ mM}.$$

The estimated glial transmembrane velocity by Equation (4.55) is

$$U_{gl}^{m*} \approx 9.78 \times 10^{-2} \text{ nm/s}.$$

From Equation (4.55) and Equation (4.53), the estimated scale of radial water velocities inside glial compartment and extracellular space are

$$u_{ex}^{r,*} \approx 1.56 \times 10^{1} \text{ nm/s}, \quad u_{gl}^{r,*} \approx 3.90 \text{ nm/s}.$$

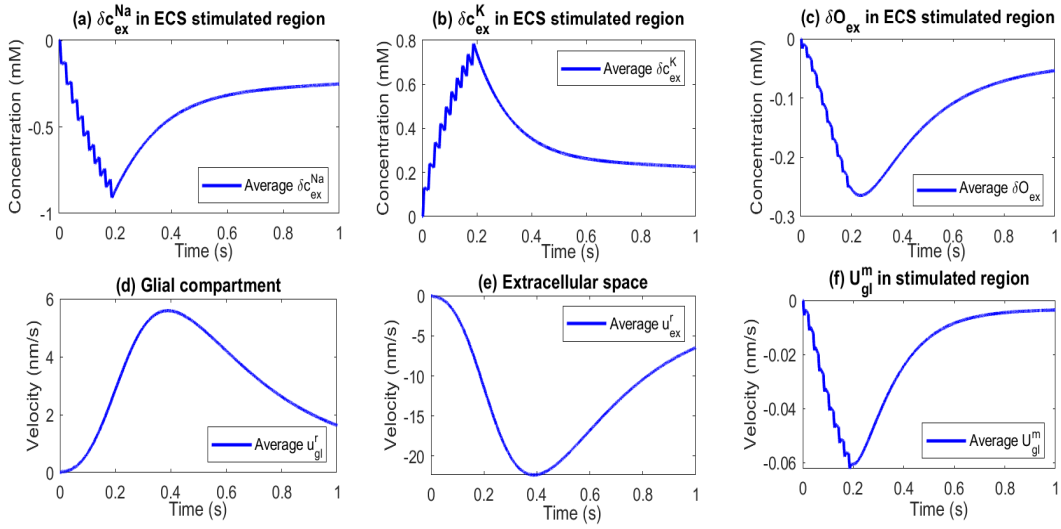

Figure 4.3: Numerical Results. a-c: Average concentration variations in the stimulated extracellular region. d-e: Average radial velocity in the intradomain. f: Average glial transmembrane velocity in the stimulated region (with normal direction points to ECS).

We now turn to the numerical results. In Figure 4.3a-c, we plot the computed average concentration variations in the stimulated extracellular region. These computed concentration changes are consistent with the estimates presented above. The change of concentration

reaches its peak at the end of the train of stimuli ($t = T_{sti}$) and quickly returns to its previous equilibrium value.

In Figure 4.3f, we plot the computed average transmembrane water flow through the glial membrane in the stimulated region. We see Figure 4.5b that the water flows into the glial compartment from the extracellular space in the stimulated region. This transmembrane water flow generates the water circulation between the stimulated and non-stimulated regions in the radial direction. As in the Figure 4.5b, in the extracellular compartment, the water flow goes from the non-stimulated region to the stimulated region. In the glial compartment, water flows in the opposite radial direction. In Figure 4.3d-e, we plot the computed average radial water velocity in the glial compartment and extracellular space. The computational results are consistent with our estimation above.

In Figure 4.4a, we show the numerical simulation of the transmembrane water flow through the glial membrane in the non-stimulated region as in the schematic Figure 4.5b. This water flow to the extracellular space produces widening of the extracellular space volume in the non-stimulated region, as shown in Figure 4.4b. At the same time, the extracellular space volume shrinks (in the stimulated region) as shown in Figure 4.4c. The shrinkage is produced by the inward water flow through the glial membrane in stimulated region, as in Figure 4.3f.

Our simulation is consistent with the experiments in reference [5, 6], where the extracellular space become smaller in the middle cortical layers (where the stimulus applied) but widens in the most superficial and deep cortical layers (where no stimulus is applied).

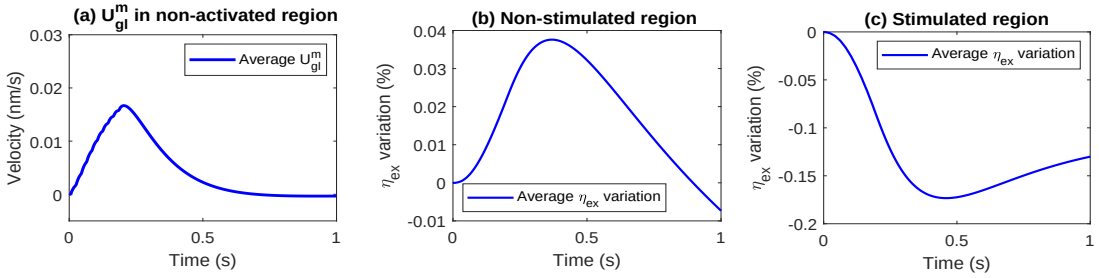

Figure 4.4: a: Average glial transmembrane velocity in the non-stimulated region (with normal direction points to ECS). b-c: Variations of the average extracellular volume fraction in the non-stimulated and stimulated regions.

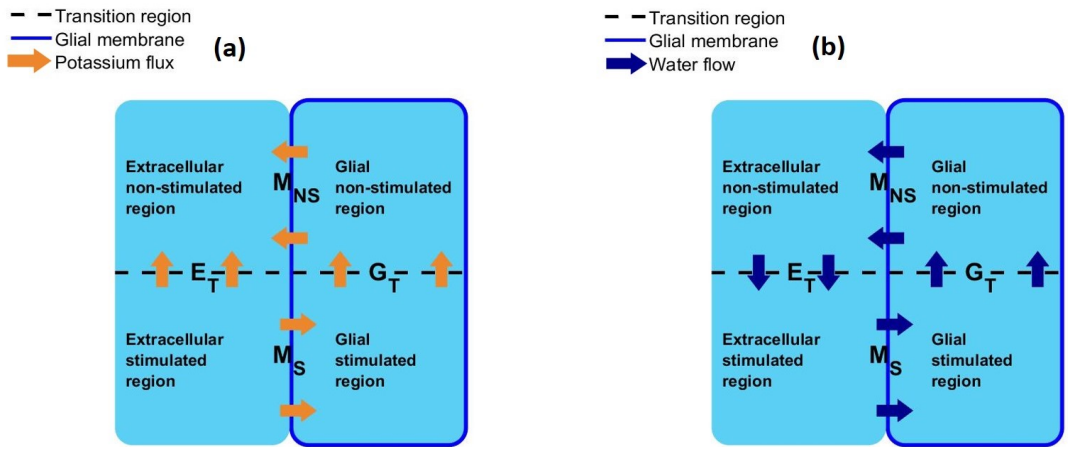

Figure 4.5: a: Schematic graph of the potassium flux when inner part axon was stimulated. b: Schematic graph of the water circulation when inner part axon was stimulated.

Remark 4.3. In Figs. 4.6-4.7, it is an illusion that there are jumps in the contours of volume fractions for extracellular space and glial compartment. By checking a line-plot at a fixed radius $r = 1.5\mu$m, Figure C.1 in the Appendix illustrates that there are not jumps rather than local extreme values at the $z_0 = 1.875$ mm where the stimuli are applied. These stimuli result in the local potassium accumulation which decreases the osmosis variation in the extracellular space near z_0 (see Appendix Figure C.3). Therefore, less shrunken of the extracellular volume fraction near z_0 as Figs. 4.6-4.7 shown.

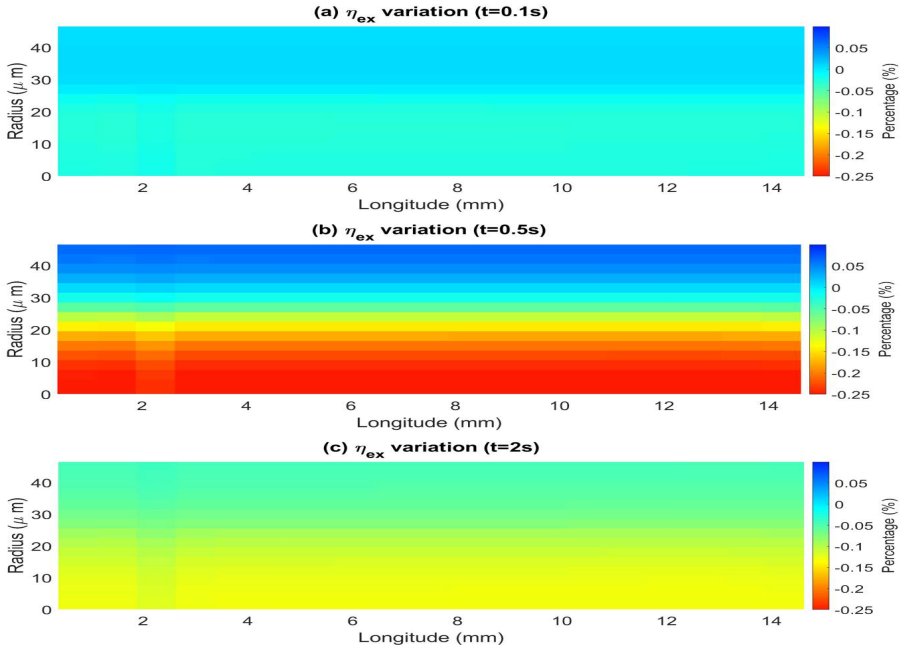

Figure 4.6: (a)-(c): Extracellular volume fraction (η_{ex}) variation at time $t = 0.1$s, 0.5s, 2s. The blue is the enlarged region of extracellular space and red is the shrunken region of the extracellular space which is qualitatively consistent with the results in [5, 6].

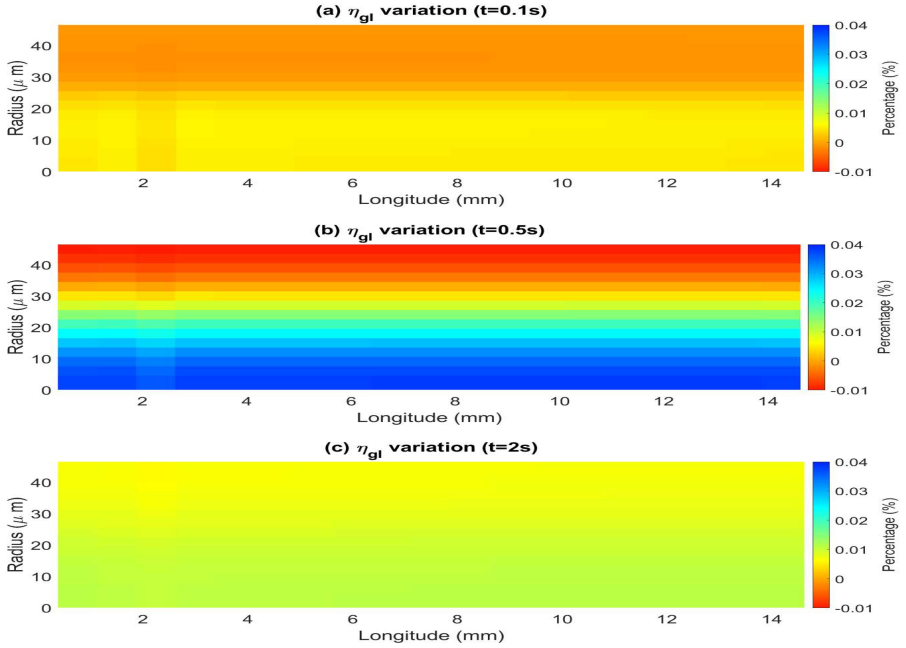

Figure 4.7: (a)-(c):Glial compartment volume fraction (η_{gl}) variation at $t = 0.1$s, 0.5s, 2s.

4.2.2 Importance of convection in the glial compartment

In this section, we explore the importance of fluid convection during potassium clearance in each region. We first examine the estimated Peclet numbers for Na^+ and K^+ in the extracellular and glial compartments.

By Equation (4.56), the Peclet numbers (for the radial ion flux) in the extracellular space are

$$Pe_{ex}^K = \left| \frac{c_{ex}^K u_{ex}^{r*} r^*}{D_{ex}^K \tau_{ex} \delta c_{ex}^K} \right| \approx 1.0 \times 10^{-2}, \quad Pe_{ex}^{Na} = \left| \frac{c_{ex}^{Na} u_{ex}^{r*} r^*}{D_{ex}^{Na} \tau_{ex} \delta c_{ex}^{Na}} \right| \approx 3.5 \times 10^{-1}.$$

By Equations (4.42) and (4.43), the ratios between electric drift and diffusion (of the radial ion flux) in the extracellular space are

$$R_{ex}^K = \left| \frac{\eta_{gl}\sigma_{gl}}{\eta_{ex}\sigma_{ex}\left(1+h_\epsilon\right)} \right| \approx 6.2 \times 10^{-2}, \quad R_{ex}^{Na} = \left| \frac{\eta_{gl}\sigma_{gl}}{\eta_{ex}\sigma_{ex}\left(1+h_\epsilon\right)} \frac{c_{ex}^{Na}}{c_{ex}^K} \right| \approx 2.3.$$

In the glial compartment, based on Equations (4.57), (4.59) and (4.60), we get the Peclet numbers (for the radial ion flux) in the glial compartment are

$$Pe_{gl}^K = \left| \frac{c_{gl}^K u_{gl}^{r*} r^*}{D_{gl}^K \tau_{gl} \delta c_{gl}^K} \right| \approx 2.9 \times 10^1, \quad Pe_{gl}^{Na} = \left| \frac{c_{gl}^{Na} u_{gl}^{r*} r^*}{D_{gl}^{Na} \tau_{gl} \delta c_{gl}^{Na}} \right| \approx 1.7 \times 10^1.$$

By Equation (4.58), the ratios between electric drift and diffusion (of the radial ion flux) in the glial space are

$$R_{gl}^K = \left| \frac{1}{1+h_\epsilon} \frac{c_{gl}^K \delta c_{ex}^K}{c_{ex}^K \delta c_{gl}^K} \right| \approx 4.3 \times 10^2, \quad R_{gl}^{Na} = \left| \frac{1}{1+h_\epsilon} \frac{c_{gl}^{Na} \delta c_{ex}^K}{c_{ex}^K \delta c_{gl}^{Na}} \right| \approx 1.7 \times 10^2.$$

In Figure 4.8, we plot the computed average K^+ and Na^+ flux components in the extracellular space and glial compartment, respectively.

In the extracellular space, the importance of different fluxes are complicated because they depend on the ion species concentration as shown in Equation (4.56). For potassium, the diffusion flux is dominant as shown in Figure 4.8a upper panel. But for the sodium (Figure 4.8a lower panel), the three fluxes, diffusion, convection, and electric drift, are comparable with the electric drift flux being somewhat larger. These simulation results agree with our estimations above. In the extracellular space, the potassium's Pelect number Pe_{ex}^K and the ratio R_{ex}^K are in $O(10^{-2})$, while the sodium's Pelect number Pe_{ex}^{Na} is order of $O(10^{-1})$ and the ratio R_{ex}^{Na} is in $O(1)$.

In the glial compartments (Figure 4.8b), the situation is different from the extracellular space. The electric drift is dominant, and convection flux comes as second in importance for both sodium and potassium. The water flow has a more important effect on potassium in the glial compartment than in the extracellular space. The maximum of the convection flux

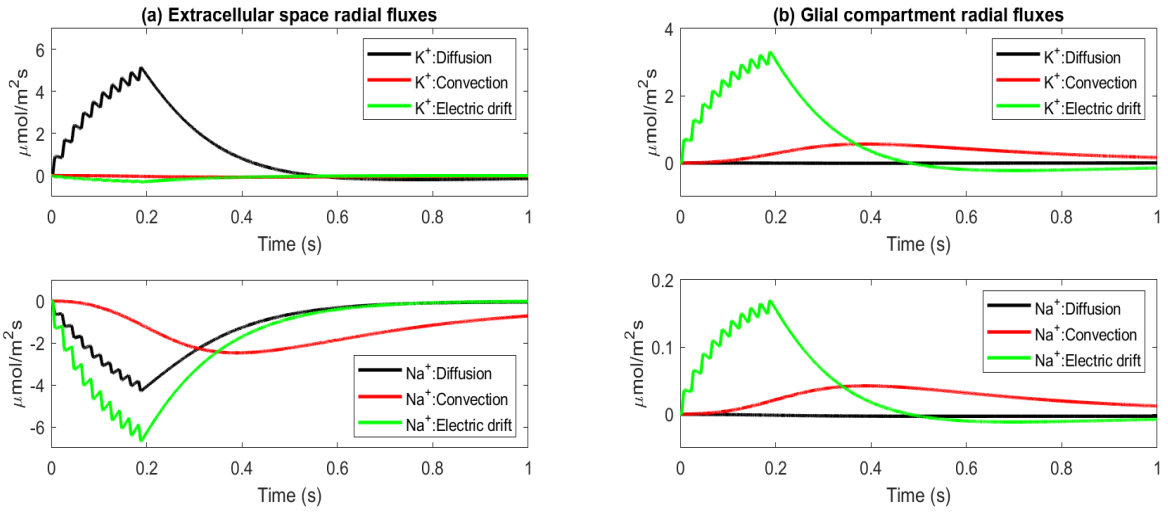

Figure 4.8: a: Average radial direction fluxes components in the extracellular space. b: Average radial direction fluxes components in the glial compartment (radial direction as normal direction).

occurs after the stimuli, since it takes that long for osmotic pressure to accumulate. Also, it lasts longer time when the effect of electric drift has decreased.

In Figure 4.9a and 4.9b, the potassium and sodium flux through the glial membrane are presented, and the results are consistent with our estimates. The major current in the glial membrane is through the potassium channel in both the stimulated and non-stimulated regions. Figure 4.9c shows the total potassium fluxes through potassium channel (integrated over the glial membrane area). The strength of total potassium fluxes in the stimulated and non-stimulated regions are the same, but they differ in direction as in our previous estimates in Equation (4.37).

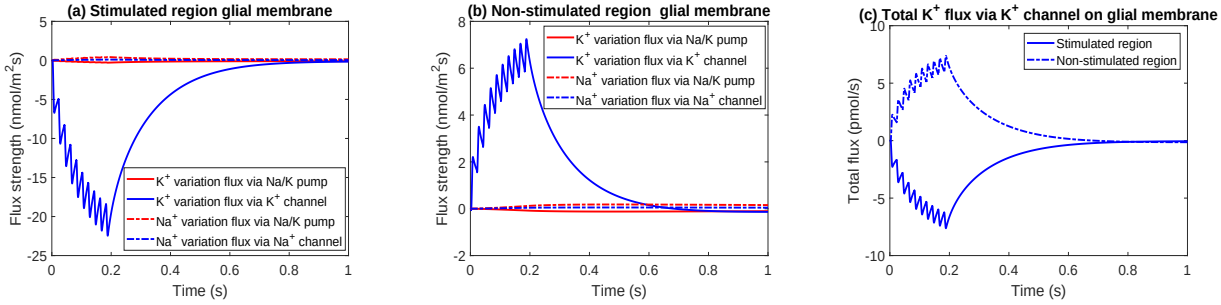

Figure 4.9: a: K^+ and Na^+ flux variations through Na/K pump and ion channels on the stimulated glial membrane. b: K^+ and Na^+ flux variations through Na/K pump and ion channels in the non-stimulated glial membrane. c: The total K^+ fluxes through K^+ channel in the stimulated membrane and non-stimulated glial membrane.

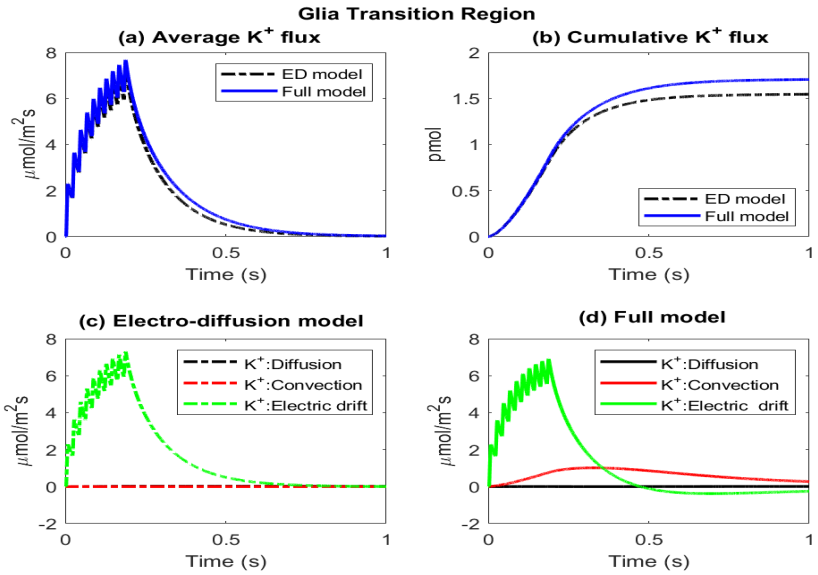

Figure 4.10: Comparison between electrodiffusion model and full model on average K^+ flux, cumulative K^+ flux and K^+ flux components on glial transition region S_T (with radial normal direction).

We now compare the results of the electrodiffusion model with the convection-electrodiffusion (full) model to show the effect of water flow on potassium transport. Figure 4.10 compares potassium flux in the electrodiffusion (ED) model and convection-electrodiffusion (full) model. In the full model, due to water circulation between the stimulated and non-stimulated regions in glial compartment, the potassium flow through the glial compartment has been increased. Figure 4.10b shows how this water flow increases potassium flux through the glial transition region in comparison to the electro-diffusion model. In this way, water circulation enhances the effect of glial compartment on potassium buffering in the optic nerve.

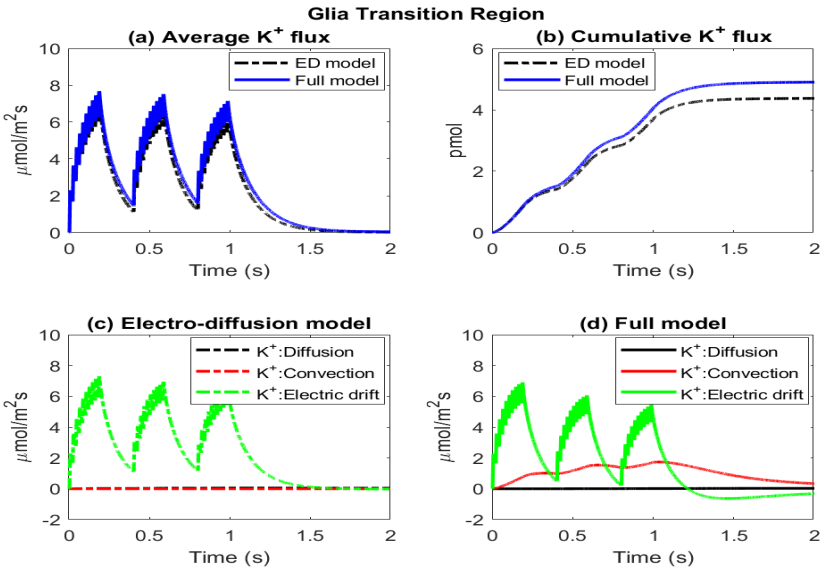

Figure 4.11: Comparison between electro-diffusion model and full model when three trains of the stimulus current are applied to the axon (with radial normal direction).

Multiple trains of action potentials strengthen the effect of water flow on the transport through the glial compartment. In Figure 4.11, we present the simulation results when three trains of action potentials occur (with 0.2 s resting period between each train of stimuli). Figure 4.11b shows that the water flow increases the amount of cumulative potassium flux through the transition region in the glial compartment, beyond the potassium flow in the electro-diffusion model. In the Figure 4.11d, the potassium convection flux gradually becomes an more important component in the glial compartment as multiple trains of action potentials occurs.

4.3 Conclusions

In this chapter, we provide a comprehensive set of estimations and computations, showing water circulation and its effect on potassium transport in the optic nerve. The estimations

show the main effects. The computations validate the estimations and verify the qualitative analysis that is so important for biologists understanding.

Through our analysis, we identify the osmotic pressure variations in the stimulated region due to the difference in ion conductance on the glial membrane. As a result of these osmotic pressure variations, glial transmembrane water flows in the stimulated region and forms the water circulation between the stimulated and the non-stimulated regions in the optic nerve.

Our estimation of the velocity scales in the glial compartment and extracellular space shows that this water flow has a considerable effect on potassium flux in the glial compartment. By comparing the full model (including water) with the electrodiffusion model (excluding water), we validate the conclusion of our analytical perturbations. Water circulation through the glial pathway helps potassium clearance in the extracellular space and enhances the glial buffering effect. With additional numerical simulations, we show that the repetitive activity of the nerve fibers further increases the importance of water flow, and increases the water flow contribution to glia buffering.

Water flow is likely to dramatically dominate pathological situations of the repetitive activity. The importance of convection is hardly a surprise to physiologists familiar with the role of the circulatory system in animals in general. In our computations of the optic nerve, convection and water flow dominate, but those flows are mostly in the glia. The glia form the pathway for convection and clearance in this optic nerve. Our results substantiate the views of workers on the glymphatic system, by direct calculation and mathematical analysis .

In addition, we show the role of the electrical syncytial property of the glial cells during the neuron firings. The inward glial transmembrane potassium flux in the stimulated region is almost the same as the outward potassium flux out to the extracellular space in the non-stimulated region. This is due to the fact that the electric potential spreads through the connected cells in the glial compartment. The glial electric potential in the non-stimulated region becomes more positive in response to the depolarization of the glial electric potential in the stimulated region. In this way, the glial cells wrapping the axon form a faster potassium transporter, which removes the extra potassium in the extracellular space from the stimulated region to the non-stimulated region.

Chapter 5

Potassium clearance in optic nerve

In this chapter, we explore potassium clearance in the optic nerve under various conditions using the tridomain model. In Section 5.1, we apply a train of stimuli at alternative locations on the axon membrane and show the cooperative interactions between the extracellular pathway and the glial compartment to help potassium clearance during a train of stimuli. In addition, we find that the glial transmembrane pathway become the major potassium clearance mechanism after the neuron stops firing. In Section 5.2, we further study the effect of glial membrane conductance and boundary condition on the pia (macroscopic) membrane on potassium clearance. We introduce the Na-K-Cl cotransporter (NKCC) into the glial membrane and consider a paracellular (non-selective) pathway on the pia boundary. Through numerical simulations, we find that NKCC in the glial membrane dramatically increase the potassium clearance speed in comparison to the baseline model (without NKCC channels in the glial membrane). At the same time, the non-selective pathway in the pia mater does not have significant effect on potassium clearance.

5.1 Alternative distribution of stimulus location

In this section, we apply the stimulus current at several different radial locations. We seek to determine whether the choice of radial location affects potassium clearance and fluid velocity. To facilitate the discussion, we define the following regions which K^+ flux could pass through

- M_S: glial membrane in stimulated region,
- E_T: extracellular pathway in transition region,
- M_{NS}: glial membrane in non-stimulated region,
- G_T: glial pathway in transition region.

The normal directions on M_S and M_{NS} point to ECS and the normal direction of E_T and G_T is the radial direction. We mainly focus on the two distinguished periods of time,

- during a train of stimuli ($[0, T_{sti}]$),
- after neuron stops firing ($[T_{sti}, T_{af}]$).

In the simulations below, we take $T_{sti} = 0.2$ s and $T_{af} = 10$ s.

5.1.1 Inner and outer radial regions stimulated

We first make a comparison between the inner radial stimulated case ($\{(r, z, \theta)|\ 0 < r < \frac{r^*}{2}, z = z_0, \theta \in [0, 2\pi]\}$) with the outer radial stimulated case ($\{(r, z, \theta)|\ \frac{r^*}{2} < r < r^*, z = z_0, \theta \in [0, 2\pi]\}$). For the inner radial stimulated case, the stimulated region is $V_S^{in} = \{(r, z, \theta)|r < \frac{r^*}{2}, z \in [0, L], \theta \in [0, 2\pi]\}$ and the non-stimulated region is $V_{NS}^{in} = \{(r, z, \theta)|\frac{r^*}{2} < r < r^*, z \in [0, L], \theta \in [0, 2\pi]\}$; for the outer radial stimulated case, $V_{NS}^{out} = V_S^{in}$ and $V_S^{out} = V_{NS}^{in}$. The transition region $S_T = \{(r, z, \theta)|r = \frac{r^*}{2}, z \in [0, L], \theta \in [0, 2\pi]\}$ is the same for both cases.

(a) During a train of stimuli

In Figure 5.1, we plot the total K^+ flux (K^+ flux integrated over area) and the cumulative K^+ flux (total K^+ flux integrated over time) during a train of stimuli $[0, T_{sti}]$. In both cases, Figure 5.1ab shows that the glial transmembrane K^+ flux in stimulated region (M_S), and K^+ flux through extracellular transition region (E_T) act together to facilitate potassium clearance in the stimulated extracellular space. The cumulative K^+ flux through the glial

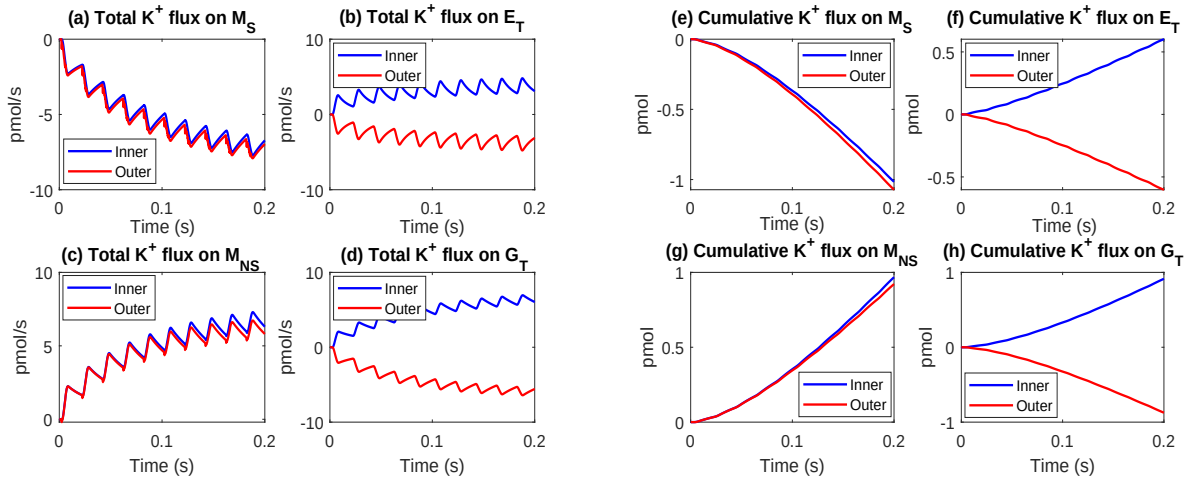

Figure 5.1: a-d: Total K^+ fluxes through M_S, E_T, M_{NS} and G_T during a train of stimuli. e-h: Cumulative K^+ fluxes during a train of stimuli.

membrane (M_S) is twice as large as that through the extracellular pathway in transition

region (E_T) as shown in Figure 5.1ef. This numerical result supports our previous estimation in Equation (4.39) that the λ_{ex}^{K} is comparable to the $\lambda_{gl}^{m,K}$.

In both cases, numerical simulations confirm that the glial compartment serves as an important and quick K^+ transport device to remove the accumulated K^+ when the neuron fires action potentials. In Figure 5.1eg, the cumulative K^+ flux through the glial membrane (M_S) into the stimulated glia compartment is almost the same as that leaking out to extracellular space through the non-stimulated glial membrane (M_{NS}). The cumulative K^+ flux through the glial transition region (G_T) is also the same as shown in Figure 5.1h. These observations verify our previous estimations in Equation (4.37).

The spatial distributions of K^+ concentration changes from resting state over time are shown in the Figure 5.2 and Figure 5.3. Figure 5.2 shows that the K^+ concentration varies in the stimulus region along the longitudinal direction during one action potential, while there is no change of K^+ in the non-stimulus region. Figure 5.3 ab show there an obvious potassium concentration difference in the radial direction after a train of stimuli over time $T_{sti} = 0.2s$. In Figure 5.3c, the potassium concentration difference vanishes due to the communication of the extracellular space and glial compartment shown in Figure 5.5fg.

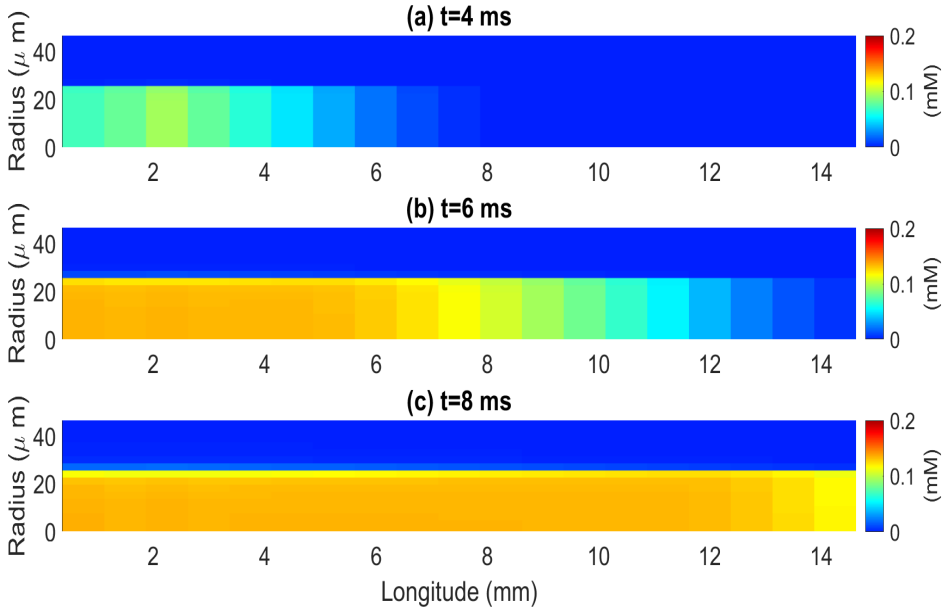

Figure 5.2: Spatial distribution of potassium changes from the resting state during an action potential.

During a train of stimuli, K^+ in both the extracellular space and glial compartment continue to move from the stimulated region to the non-stimulated region shown in Figure 5.1bd. The schematic graph of potassium transport in the optic nerve is the same as the Figure 4.5a.

Water circulation in the optic nerve driven by the extracellular osmotic pressure variation is shown in Figure 5.4. Through the glial membrane (M_S), water increasingly flows into the

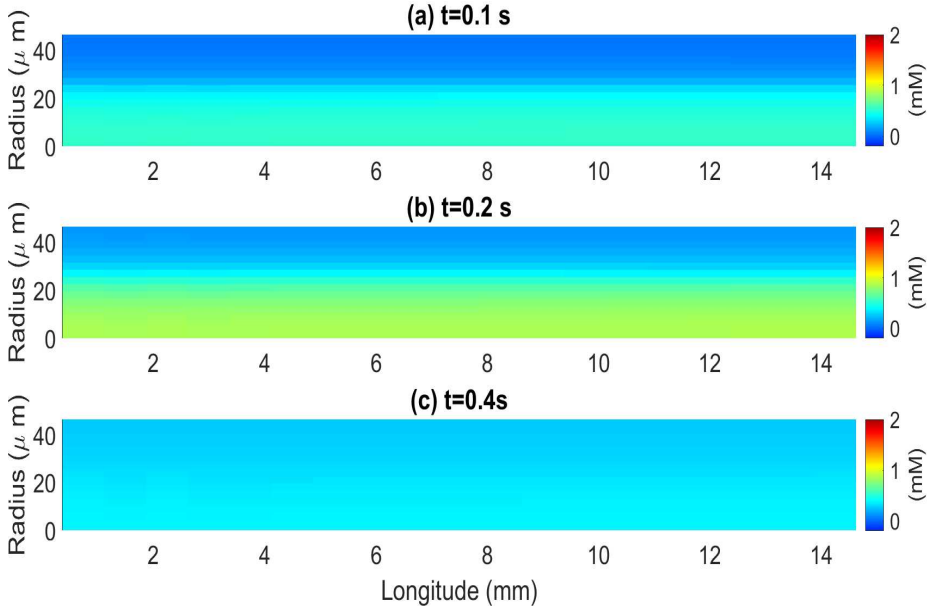

Figure 5.3: Spatial distribution of potassium changes from the resting state during and after a train of stimuli.

glial compartment from the extracellular space (Figure 5.4*a*). The glial volume fraction and the hydrostatic pressure in the stimulated region have also increased. This increased hydrostatic pressure raises the hydrostatic pressure in the non-stimulated region as water flows from the stimulated region to the non-stimulated region through transition region G_T (See Figure 5.4*d*). In the non-stimulated region, water flows out of the glial compartment into the extracellular space because of the increased glial hydrostatic pressure (Figure 5.4*c*). Then, because the fluid is incompressible, the fluid in the non-stimulated region flows back to the stimulated region through transition region E_T (Figure 5.4*b*). The schematic graph of water circulation in the optic nerve is summarized in Figure 4.5*b*. Note that calculations are always done on field equations. The compartments in the figure are used to make vivid the biological conclusions of the analysis of the partial differential equations of our tridomain model.

In Figure 5.4*ef*, we show how the extracellular space volume fraction changes. In the stimulated region, the volume of extracellular space decreases because water flows into the glial cell; while in the non-stimulated region, the extracellular space expands because of the water flow [77].

In sum, during a train of stimuli, the potassium transport pattern and potassium flux strength are the same for both inner and outer radial stimulated cases. The glial compartment pathway is the dominant clearance mechanism of the potassium accumulated in the extracellular stimulated region in both cases.

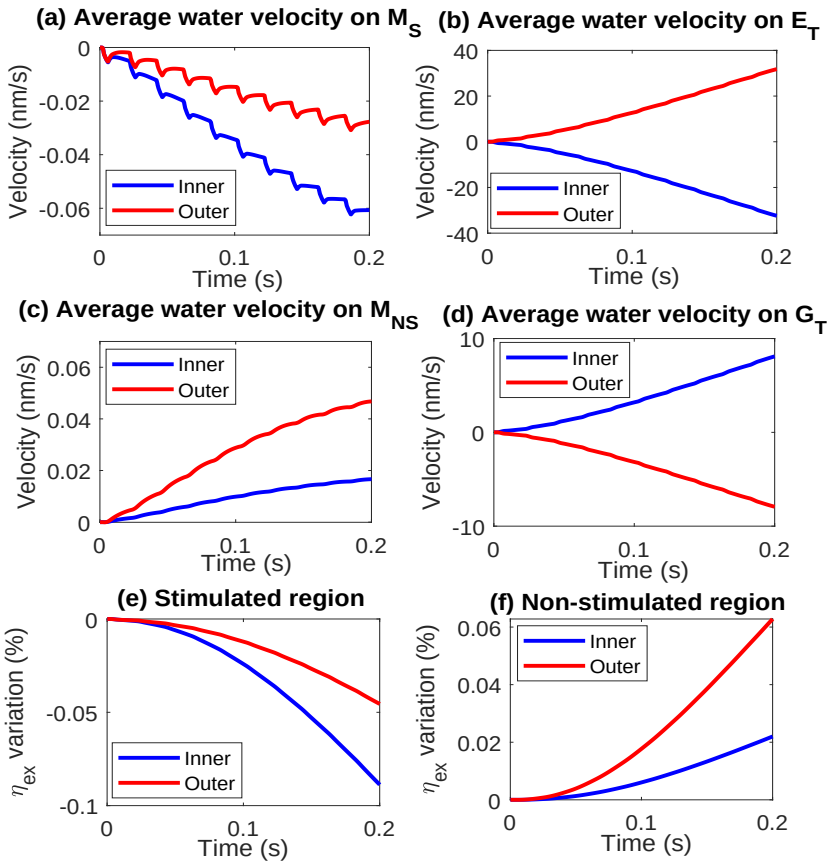

Figure 5.4: a-d: Average water velocities through M_S, E_T, M_{NS} and G_T during a train of stimuli in $[0, T_{sti}]$. e-f: Variations of extracellular volume fractions in the stimulated and non-stimulated regions.

(b) Post firing time period

After neuron stops firing, the strength of K^+ fluxes through the glial transmembrane pathway (M_S) and extracellular pathway (E_T) have dramatically decreased in both cases. In Figure 5.5, we plot the total K^+ flux and the cumulative K^+ fluxes through M_S, E_T, M_{NS}, and G_T after neuron stops firing. The figure shows the main potassium clearance mechanism is through the glial transmembrane (M_S and M_{NS}).

Figure 5.5*e* shows that the K^+ flux keep flowing into the stimulated glial compartment after the axon firing period. Figure 5.5*g* shows that the K^+ flux through the glial membrane in the non-stimulated region reverses its direction for a short time after the neuron stops firing. This occurs because right after neuron stops firing, the extracellular K^+ concentration has not become evenly distributed in space, and the glial compartment and extracellular pathway keep on carrying the extra K^+ from stimulated region to non-stimulated region.

The K^+ fluxes inside of glial compartment become negligible for a short time after neuron

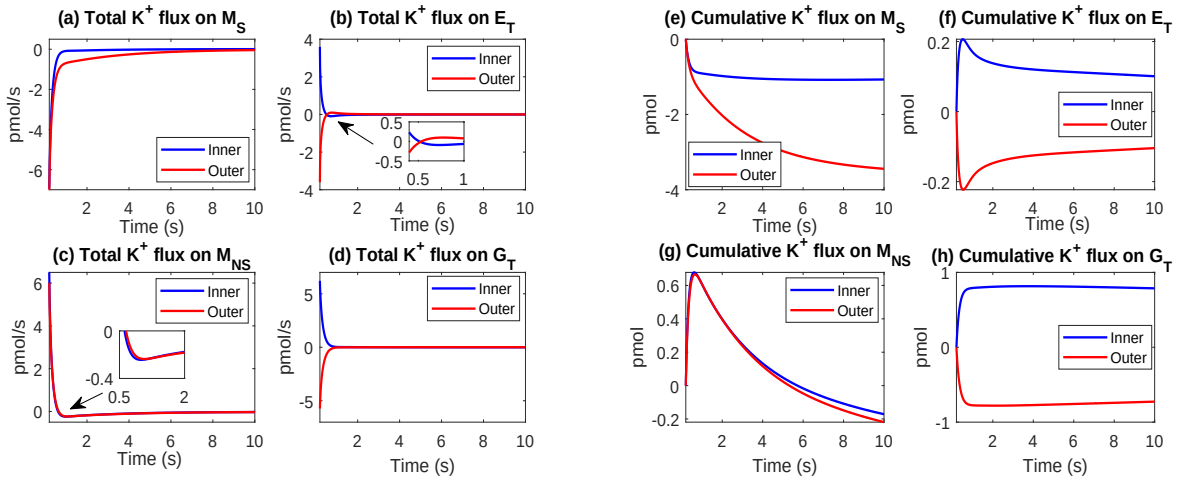

Figure 5.5: a-d: Total K^+ fluxes through M_S, E_T, M_{NS}, and G_T after neuron stops firing. e-h: Cumulative K^+ fluxes after neuron stops firing.

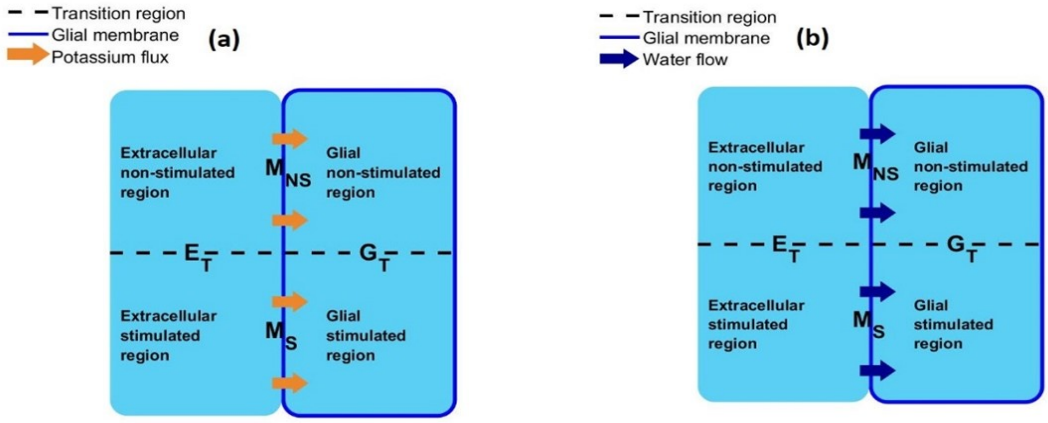

Figure 5.6: a: Schematic graph of the K^+ flux after neuron stops firing. b: Schematic graph of the water flow after neuron stops firing. The compartments shown are important for biological understanding and comparison with the literature. We do not compute a compartmental model. Our computations are of field models with partial differential equations in space and time.

stops firing shown in Figure (5.5h). The glial compartment could be approximated as a single compartment. In Figure 5.5f, in the extracellular space, K^+ flows back to the stimulated region from the non-stimulated region via the extracellular pathway. A schematic figure of potassium flux pattern is shown in Figure 5.6a.

Accordingly, Figure 5.7 shows that after the neuron stops firing, the water flow inside the compartments almost stops. The water flows through both stimulated and non-stimulated

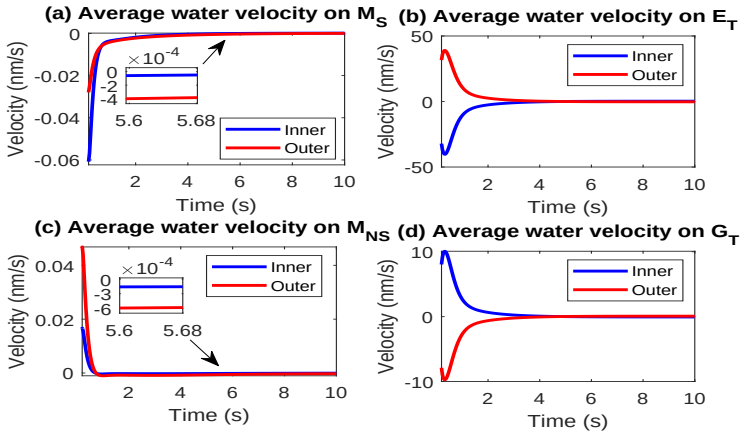

Figure 5.7: a-d: Average water velocities through M_S, E_T, M_{NS} and G_T after neuron stops firing.

glial membrane into the glial compartment, which is the same as the schematic graph Figure 5.6*b*.

In sum, after the neuron stops firing action potentials, the extracellular K^+ concentration becomes evenly distributed between the stimulated and non-stimulated regions in a short time. The potassium flux through the extracellular pathway becomes weaker and the primary clearance of potassium is through the glial membrane in both stimulated and non-stimulated regions.

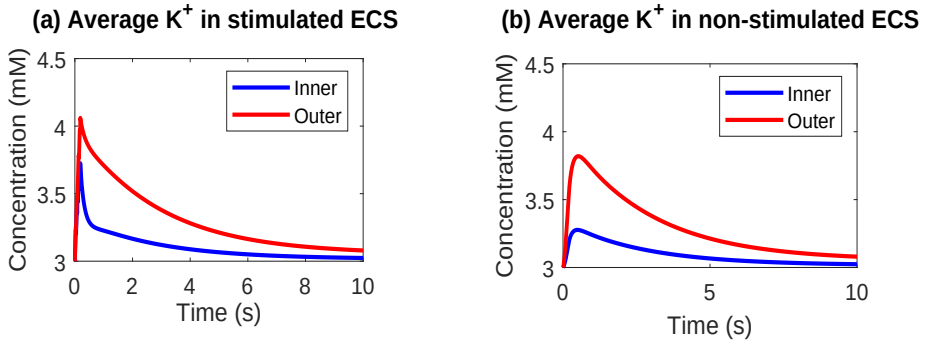

Figure 5.8: a-b: K^+ concentration variations in the stimulated and non-stimulated extracellular regions.

In Figure 5.8*ab*, we show the K^+ concentration variation in the stimulated and non-stimulated extracellular regions, respectively. The peak K^+ concentration approximately occurs at the end of stimuli in both cases. In the stimulated region, the outer radial stimulated case has a higher peak value than the inner case (Figure 5.8*a*). This is because the strength of potassium clearance (through M_s and E_T) is the same for both cases during a

train of stimuli (see Figure 5.1ab) and the volume of outer stimulated region (V_S^{out}) is as triple as the volume of inner stimulated region (V_S^{in}). In a similar way, this also explains the peak K^+ concentration in the non-stimulated region (Figure 5.8*b*). We provide a decay timetable for K^+ concentration in Appendix D.2.

5.1.2 Randomly distributed stimulated cases

In this section, we consider the cases when stimulations are distributed randomly in the radial direction, which differ from the spatially uniform ones (inner or outer cases). We apply a train of stimuli to randomly selected regions in the radial direction. The strength, duration and location of stimuli are the same as in the Section 4.2. The details of radial stimulated location are shown in Figure 5.9.

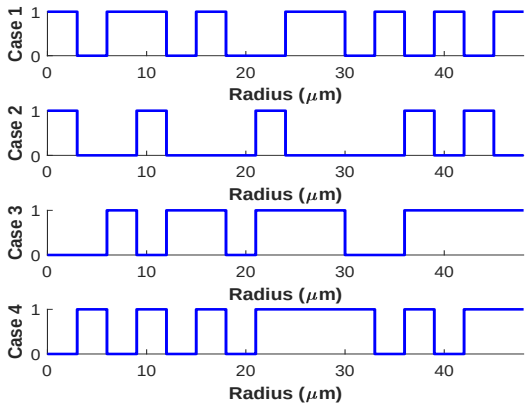

Figure 5.9: Stimulated radial segments in each case. The intervals with value 1 are stimulated segments, and the intervals with value 0 are unstimulated segments.

(a) During a train of stimuli

We compare the spatially randomly stimulated case (case 1, the rest cases are shown in Appendix D.2) with the inner radial stimulated case in Figure 5.10$a-d$. Figure 5.10ab show that the potassium flux through the extracellular pathway (E_T) has dramatically increased and potassium clearance through the glial transmembrane (M_S) has been reduced.

Figure 5.10ef shows that the major K^+ clearance pathway in the randomly stimulated cases becomes the extracellular transition pathway (E_T) during a train of neuron firings. This differs from the outer and inner stimulated cases, where the glial transmembrane (M_S) is the dominant K^+ clearance pathway as seen in Figure 5.1ef.

In addition, in Figure 5.10$a-d$, the K^+ flux pattern is quite different. In the inner stimulated case (blue line), the strength of K^+ flux gradually increased with small oscillations

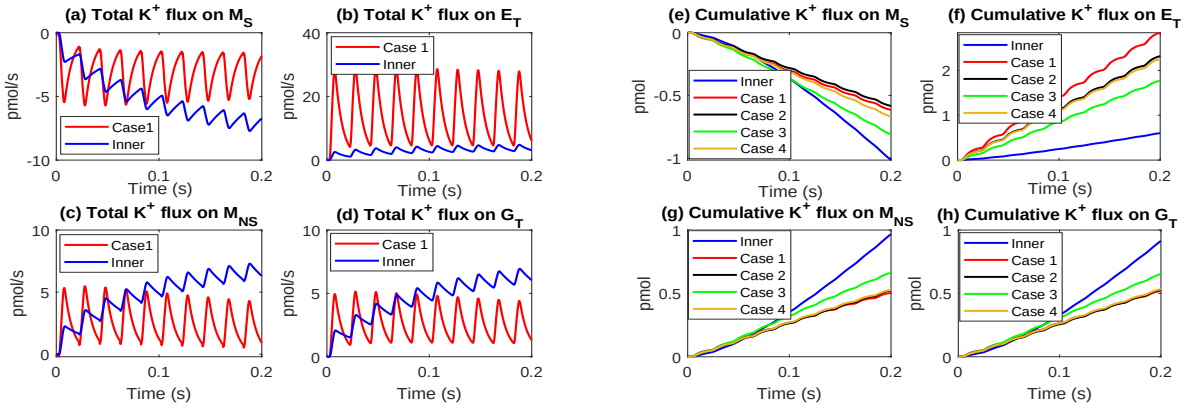

Figure 5.10: Comparison between spatially randomly stimulated case 1 with the uniform radial (inner) case during a train of stimuli.

in each stimulus period; While in the spatially randomly stimulated case (red line), the strength of K^+ flux shows a periodic pattern in time with larger oscillations in each stimulus period. The reason for this is that the extra K^+ in the stimulated extracellular region has been cleared more quickly in the random case than the inner case, which leads the K^+ concentration goes back to its resting state faster.

(b) Post firing time period

In this period, both cases have similarly reduced potassium fluxes (see Figure 5.11$a-d$) and the main pathway for potassium clearance is through the glial transmembrane pathway (M_S and M_{NS} in Figure 5.11eg).

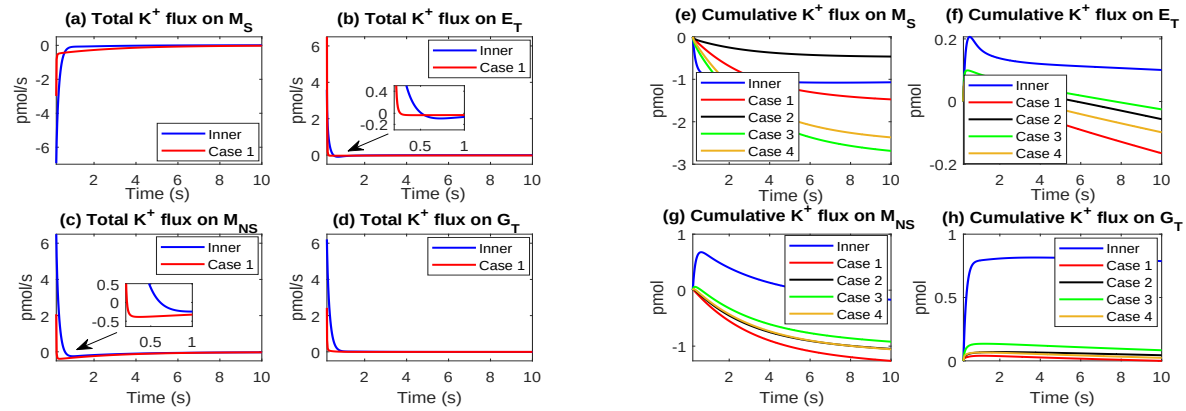

Figure 5.11: Comparison between spatially randomly stimulated case 1 with the uniform radial (inner) case after a train of stimuli.

Right after neuron stops firing, Figure 5.11fg show that the potassium fluxes direction

in randomly stimulated case and inner stimulated case are different. This phenomenon happens because there still exists spatially inhomogeneous potassium concentration between stimulated and non-stimulated regions in the inner case. As a result of that, the glial electric potential ϕ_{gl} follows the potassium pattern and forms the electric drift flux in the glial radial direction as shown in Figure 5.11*h*.

(c) Potassium clearance and fluid velocity

In the randomly simulated cases, since the potassium through the glial transmembrane pathway in the stimulated region is less compared to that in the baseline case (in Figure 5.10e), the extracellular osmotic pressure variation in the stimulated region has been reduced. As a result, the glial transmembrane water flow in the stimulated region is reduced, which also leads the intradomain velocities decrease as shown in Figure 5.12*cd*. The average potassium concentration changes in both the stimulated and the non-stimulated regions are shown in Figure 5.12*ab* and the randomly simulated cases have similar potassium decay rate (timetable is shown in Appendix D.2).

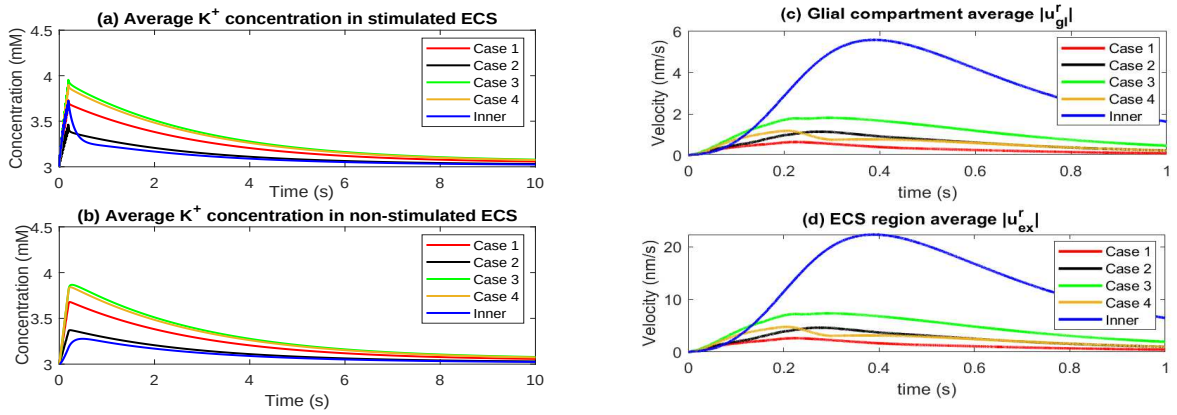

Figure 5.12: a-b: Potassium concentration variations in the extracellular stimulated and non-stimulated regions. c-d: Average glial compartment and extracellular space absolute radial velocities.

5.2 Effect of NKCC and non-selective pathway

In this section, we consider the effect of glial membrane conductance and a non-selective pathway at the pia boundary on the potassium clearance process. We first consider the Na-K-Cl cotransporter (NKCC) on the glial membrane, which has widely studied in the literature [85, 86]. We compare simulation results between the models with NKCC and without NKCC. In the second part, we consider the effect of a non-selective pathway at the

pia mater boundary, which allows the convection flux through an extracellular pathway out of the optic nerve. We explore how these factors affect potassium clearance.

5.2.1 Effect of NKCC on the glial membrane

On the glial membrane, there is an impressive array of potassium channels, which may be responsible for elevated K^+-induced glial swelling. NKCC is one of the commonly recognized co-transporters for K^+-mediated glia swelling and K^+ clearance in the optic nerve [87, 88]. The main character of the NKCC proteins is they can transport one Na^+ and one K^+ and two Cl^- across the cell membrane at the same time. The energy required by NKCC proteins to move Na^+, K^+ and Cl^- across the cell membrane is provided by the electrochemical gradient of Na^+, which is indirectly dependent on the Na/K pump and ATP supply. For this reason, NKCC proteins are said to move solutes by way of secondary active transport.

In this section, we introduce a model of NKCC on the glial membrane [53, 89], which describes K^+, Na^+ and Cl^- fluxes through the NKCC on the glial membrane as follows. Note we expect other transport systems to be discovered that are important in the optic nerve and elsewhere in the central nervous system. We expect these systems to be different in different parts of the nervous system and to be specialized to support the functions of each part. The approach used here is meant to be flexible enough to accommodate different transport systems in different locations.

$$\begin{aligned} J^K_{NKCC} &= -\tfrac{I^{NKCC}_{\max}}{ez^K} \log\left(\tfrac{c^K_{ex}}{c^K_{gl}}\tfrac{c^{Na}_{ex}}{c^{Na}_{gl}}\left(\tfrac{c^{Cl}_{ex}}{c^{Cl}_{gl}}\right)^2\right), \\ J^{Na}_{NKCC} &= -\tfrac{I^{NKCC}_{\max}}{ez^{Na}} \log\left(\tfrac{c^K_{ex}}{c^K_{gl}}\tfrac{c^{Na}_{ex}}{c^{Na}_{gl}}\left(\tfrac{c^{Cl}_{ex}}{c^{Cl}_{gl}}\right)^2\right), \\ J^{Cl}_{NKCC} &= 2\tfrac{I^{NKCC}_{\max}}{ez^{Cl}} \log\left(\tfrac{c^K_{ex}}{c^K_{gl}}\tfrac{c^{Na}_{ex}}{c^{Na}_{gl}}\left(\tfrac{c^{Cl}_{ex}}{c^{Cl}_{gl}}\right)^2\right). \end{aligned} \tag{5.1}$$

To compare the models with NKCC and without NKCC, we keep the K^+ and Na^+ concentrations as well as the electric potentials in the glial compartment and extracellular space the same at resting state. In addition, we set K^+ and Na^+ currents through NKCC are comparable to the Na/K pump current as indicated by [53, 89]. We provide the two sets of parameters (NKCCa and NKCCb) in Appendix D.3, which balance the NKCC current on the glial membrane.

Figure 5.13 shows the cumulative potassium fluxes through M_S, E_T, M_{NS}, and G_T during and after a train of stimuli. With the effect of NKCC, Figure 5.13*a* shows that more potassium goes through the glial membrane in the stimulated region during neuron firings. The NKCC has enhanced the transport of potassium through the glial membrane after the axon stopped firing as well (Figure 5.13*eg*).

Figure 5.14*ab* show the variation of potassium concentration in the stimulated and non-stimulated extracellular regions. The potassium concentration decay is much faster when NKCC is present, presumably because NKCC allows larger potassium movement into the

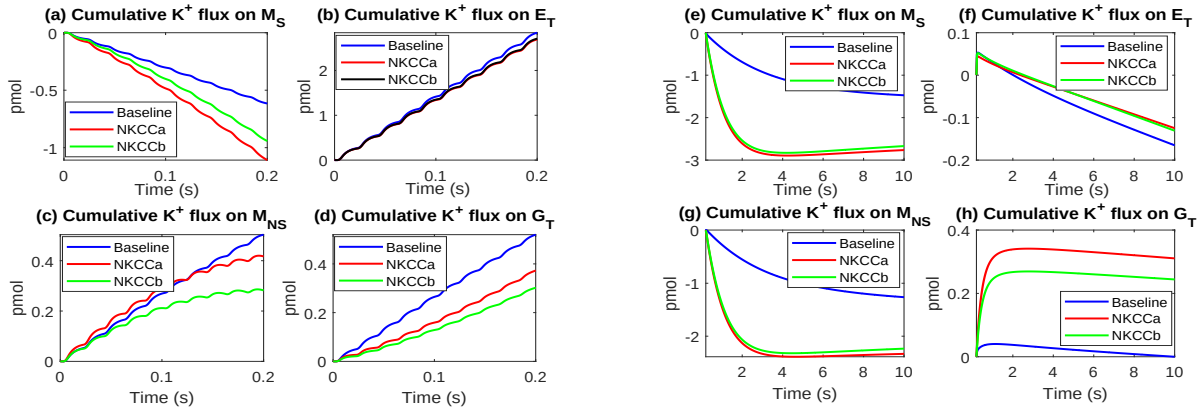

Figure 5.13: a-d: Cumulative fluxes comparison during a train of action potentials. e-h: Cumulative fluxes comparison after a train of action potentials.

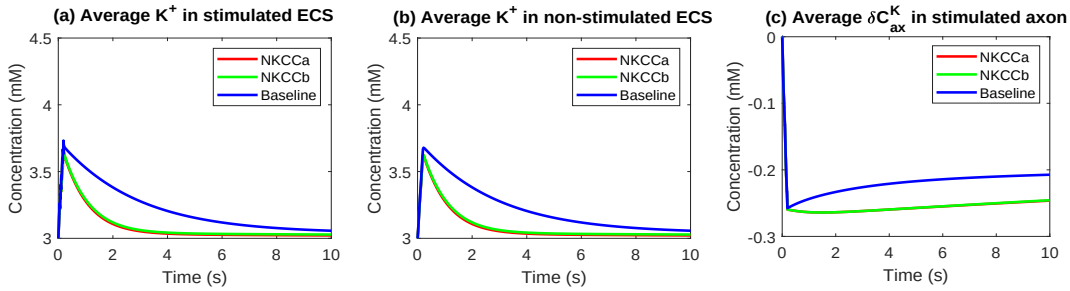

Figure 5.14: a-b: Extracellular potassium concentration variations between the model with NKCC and baseline model (without NKCC). c: Average potassium variations in the axon stimulated region.

glial compartment (the decay timetable is provided in Appendix D.3). After action potentials cease, the potassium movement back to the axon compartment is reduced in the model with the NKCC channel. Figure 5.14*c*, shows that the average potassium concentration in the baseline model increases faster after the axon stops firing than in the model with NKCC.

5.2.2 Non-selective pathway through the pia mater

In this section, we consider the effect of a non-selective pathway across the pia boundary. The non-selective pathway allows both ion and water transport through the cleft between the cells (paracellular pathway) in the pia mater. We assume that water goes through the non-selective pathway only depends on the hydrostatic pressure difference. Therefore, the condition on pia boundary (Γ_7) in Equation (3.8) becomes

$$\boldsymbol{u}_{ex}^{OP} \cdot \hat{\boldsymbol{r}} = \boldsymbol{u}_{ex}^{SAS} \cdot \hat{\boldsymbol{r}} = u_{pia}^{m} + u_{pia}^{ns}, \quad \text{on } \Gamma_7, \tag{5.2}$$

where

$$u_{pia}^{m} = L_{pia}^{m}\left(p_{ex}^{OP} - p_{ex}^{SAS} - \gamma_{pia} k_B T\left(O_{ex}^{OP} - O_{ex}^{SAS}\right)\right), \quad u_{pia}^{ns} = L_{pia}^{ns}\left(p_{ex}^{OP} - p_{ex}^{SAS}\right).$$

The non-selective pathway between the cell clefts provides an additional pathway for diffusion, electric drift as well as convection for ions. We modify the boundary condition (3.3) for ion on pia boundary (Γ_7) as

$$\begin{aligned}\boldsymbol{j}_{ex}^{i,OP}\cdot\hat{\boldsymbol{r}} &= \boldsymbol{j}_{ex}^{i,SAS}\cdot\hat{\boldsymbol{r}} \\ &= \frac{G_{pia}^{i}+G^{ns}}{z^i e}\left(\phi_{ex}^{OP}-\phi_{ex}^{SAS}-E_{pia}^{i}\right)+c_{ex}^{i}u_{pia}^{ns},\ i=\mathrm{Na}^+,\mathrm{K}^+,\mathrm{Cl}^-\ \text{on}\ \Gamma_7,\end{aligned}$$

where G^{ns} is the additional conductance due to the non-selective pathway and $c_{ex}^{i}u_{pia}^{ns}$ is the convection flux through the non-selective pathway on pia boundary.

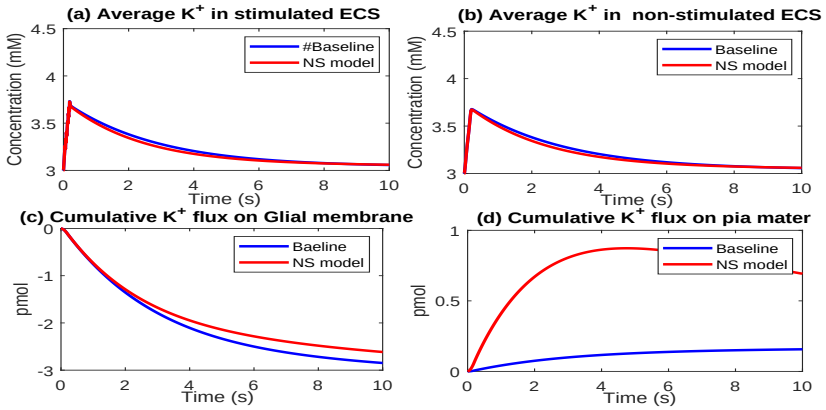

Figure 5.15: a-b: Extracellular K^+ concentration variations between the model with non-selective pathway and baseline model (without non-selective pathway). c: Cumulative K^+ flux through the glial membrane. d: Cumulative K^+ flux through pia boundary.

In the simulation study, we compare with the non-selective pathway and baseline model (without the non-selective pathway). We choose the conductances as follows

$$\frac{G^{ns}}{G_{pia}^{K}} = \frac{L_{pia}^{ns}}{L_{pia}^{m}} = 10.$$

In Figure 5.15, we show K^+ variation in the extracellular space and the cumulative K^+ fluxes through the pia mater and glial membrane. The amount of K^+ leaking out of the optic nerve through the pia boundary is dramatically increased when the non-selective pathway is present shown in Figure 5.15*d*. At the same time, the dominant pathway of potassium clearance is still through the glial membrane as previous (Figure 5.15*c*). This is mainly because the effect of the effective membrane area difference. The total glial membrane area is much larger than the surface area on the pia boundary,

$$\frac{2\pi r^* L}{V_{op}\mathcal{M}_{gl}} = O\left(10^{-3}\right),$$

where the V_{op} is the total optic nerve volume and $\mathcal{M}_{gl}$ is the glial membrane per unit volume. Figure 5.15*ab* shows that the non-selective pathway on the pia boundary does not accelerate the potassium clearance rate very much.

5.3 Conclusions

The numerical simulations in this chapter verify our previous analysis. We find that both the extracellular pathway and glial membrane play essential roles in potassium clearance from the narrow extracellular space when the neuron fires. In both spatial uniform stimulated case and spatial randomly stimulated case, the extracellular pathway and glial compartment work together to remove extra potassium from the stimulated region to the non-stimulated region. In addition, we further validate the importance of the electrical syncytial property of the glial cells, which produces an immediate outward potassium flux out to the extracellular space in the non-stimulated region, in response to the changes in potassium concentration between the stimulated and unstimulated extracellular regions.

Furthermore, we discuss the effect of enhanced potassium conductance in the glial membrane and nerve membranes of the pia mater. On the one hand, by incorporating NKCC channels into the glial membrane, it dramatically increases potassium clearance speed, and the potassium clearance time is much shorter than that predicted by the baseline model (without NKCC channels in the glial membrane). On the other hand, an additional non-selective pathway in another location, in the pia mater, does not have significant effect on potassium clearance. This is not surprising since the total membrane area of the glial membrane in the optic nerve is much greater than the effective surface membrane of nerves in the pia mater. It is important to realize that in the present state of knowledge, other relevant channels may not yet have revealed themselves. Some channels become activated only under special conditions that are hard to find. Some channels may become activated only to protect systems under severe stress, as in clinical situations like oxygen deprivation, swelling, and so on. It will be important to identify such channels as the model is applied to clinical situations, some of which are of considerable importance.

Chapter 6

Conclusions and future work

The thesis provides a glimpse of the fundamental properties in the ion and water transport in biological tissues by using a generalized multi-domain model. This work is novel since most studies in the literature mainly focus on either electro-diffusion or non-spatial models. We combine the effect of fluid circulation and spatial property into the model and study the essential characteristics of the computational model in the prediction.

Our research was inspired by the microcirculation study in the lens [3, 29], where the avascular circulation of water was discovered by the Mathias group. We proposed a generalized bidomain (full) model of the lens and studied the coupled relationships among ion fluxes, water flows and electric fields inside fiber cells and in the narrow extracellular spaces between fiber cells. In addition, a simplified model was derived based on asymptotic analysis, which allowed us to obtain a deep understanding of the physical process without making unrealistic assumptions. Our full model captured the experimental results of the gap junction in the lens [1, 2] well. At the same time, the simplified model provided a good approximation of the full model and helped to understand the effects of membrane permeability in the full model.

The hydrodynamic bidomain model of the lens pointed a way to dealing with other tissues and organs, such as the kidney, the central nervous system and cardiac muscle, in which current flows, water flow, and cell volume changes are important. We naturally extended our model to the optic nerve, which belongs to the central nervous system and proposed a tridomain model to study potassium clearance in the optic nerve of Necturus, following a series of experiments from Richard Orkand and the Harvard group [4, 13, 22]. Our model, analysis, and simulations provided a detailed picture of the role of glial cells as an electrical syncytium in buffering potassium concentration in the narrow extracellular space. In comparison with the (reduced) electrodiffusion model, water circulation driven by the osmotic pressure in the optic nerve enhanced the potassium transport in the glial compartment. At the same time, through numerical simulations, we showed the effect of increased conductance on the glial membrane and nerve membranes of the pia mater on potassium clearance.

Our study on the optic nerve now forms part of the emerging field of glymphatic system,

which has established the importance of convective flows in glia in a wide variety of clinical and biological phenomena of the CNS, from sleep to Alzheimer's disease. Our work provides a firm theoretical basis for quantitative models useful in the glymphatic system. However, our work is more than just theoretical because it fits some of the best quantitative biology done on flows in the CNS in some detail. In the future, our distributed model should be generalized to describe ionic and water transport in tissues with more complicated and heterogeneous structures and with glymphatic pathways connected to the circulatory system. Specifically, we expect that the spatially non-uniform distribution of ion and water channels and transporters can be used in many structures to control the flows.

Bibliography

[1] J. Gao, X. Sun, L. C. Moore, P. R. Brink, T. W. White, R. T. Mathias, The effect of size and species on lens intracellular hydrostatic pressure, Investigative ophthalmology & visual science 54 (1) (2013) 183–192.

[2] J. Gao, X. Sun, L. C. Moore, T. W. White, P. R. Brink, R. T. Mathias, Lens intracellular hydrostatic pressure is generated by the circulation of sodium and modulated by gap junction coupling, Journal of General Physiology 137 (6) (2011) 507–520.

[3] R. T. Mathias, Steady-state voltages, ion fluxes, and volume regulation in syncytial tissues., Biophysical journal 48 (3) (1985) 435.

[4] R. Orkand, J. Nicholls, S. Kuffler, Effect of nerve impulses on the membrane potential of glial cells in the central nervous system of amphibia., Journal of neurophysiology 29 (4) (1966) 788–806.

[5] K. Holthoff, O. W. Witte, Directed spatial potassium redistribution in rat neocortex, Glia 29 (3) (2000) 288–292.

[6] P. Kofuji, E. A. Newman, Potassium buffering in the central nervous system, Neuroscience 129 (4) (2004) 1043–1054.

[7] S. Bassnett, Lens organelle degradation, Experimental eye research 74 (1) (2002) 1–6.

[8] M. D. Jacobs, C. Soeller, A. M. Sisley, M. B. Cannell, P. J. Donaldson, Gap junction processing and redistribution revealed by quantitative optical measurements of connexin46 epitopes in the lens, Investigative ophthalmology & visual science 45 (1) (2004) 191–199.

[9] G. E. Bunce, J. Kinoshita, J. Horwitz, Nutritional factors in cataract, Annual review of nutrition 10 (1) (1990) 233–254.

[10] K.-J. Yeum, F. Shang, W. Schalch, R. M. Russell, A. Taylor, Fat-soluble nutrient concentrations in different layers of human cataractous lens, Current eye research 19 (6) (1999) 502–505.

[11] J. B. Selhorst, Y. Chen, The optic nerve, in: Seminars in neurology, Vol. 29, © Thieme Medical Publishers, 2009, pp. 029–035.

[12] S. S. Hayreh, Ischemic optic neuropathy, Progress in retinal and eye research 28 (1) (2009) 34–62.

[13] S. Kuffler, J. Nicholls, R. Orkand, Physiological properties of glial cells in the central nervous system of amphibia., Journal of Neurophysiology 29 (4) (1966) 768–787.

[14] S. S. Hayreh, The sheath of the optic nerve, Ophthalmologica 189 (1-2) (1984) 54–63.

[15] H. Killer, H. Laeng, J. Flammer, P. Groscurth, Architecture of arachnoid trabeculae, pillars, and septa in the subarachnoid space of the human optic nerve: anatomy and clinical considerations, British Journal of Ophthalmology 87 (6) (2003) 777–781.

[16] H. E. Killer, H. R. Laeng, P. Groscurth, Lymphatic capillaries in the meninges of the human optic nerve., Journal of neuro-ophthalmology: the official journal of the North American Neuro-Ophthalmology Society 19 (4) (1999) 222–228.

[17] Y. Hua, A. P. Voorhees, I. A. Sigal, Cerebrospinal fluid pressure: revisiting factors influencing optic nerve head biomechanics, Investigative ophthalmology & visual science 59 (1) (2018) 154–165.

[18] W. H. Morgan, C. Balaratnasingam, C. R. Lind, S. Colley, M. H. Kang, P. H. House, D.-Y. Yu, Cerebrospinal fluid pressure and the eye, British Journal of Ophthalmology 100 (1) (2016) 71–77.

[19] A. S. Filippidis, S. G. Zarogiannis, M. Ioannou, K. Gourgoulianis, P.-A. Molyvdas, C. Hatzoglou, Permeability of the arachnoid and pia mater. the role of ion channels in the leptomeningeal physiology, Child's Nervous System 28 (4) (2012) 533–540.

[20] R. Eisenberg, V. Barcilon, R. Mathias, Electrical properties of spherical syncytia., Biophysical Journal 25 (1) (1979) 151.

[21] R. Mathias, J. Rae, G. Baldo, Physiological properties of the normal lens, Physiological reviews 77 (1) (1997) 21–50.

[22] S. W. Kuffler, J. G. Nicholls, The physiology of neuroglial cells, in: Ergebnisse der physiologie biologischen chemie und experimentellen pharmakologie, Springer, 1966, pp. 1–90.

[23] J. P. Keener, J. Sneyd, Mathematical physiology, Vol. 1, Springer, 1998.

[24] J. Keener, J. Sneyd, Mathematical physiology 1: Cellular physiology (2009).

[25] B. Frankenhaeuser, A. Hodgkin, The after-effects of impulses in the giant nerve fibres of loligo, The Journal of physiology 131 (2) (1956) 341–376.

[26] B. Ransom, C. Yamate, B. Connors, Activity-dependent shrinkage of extracellular space in rat optic nerve: a developmental study, Journal of Neuroscience 5 (2) (1985) 532–535.

[27] B. R. Ransom, R. K. Orkand, Glial-neuronal interactions in non-synaptic areas of the brain: studies in the optic nerve, Trends in neurosciences 19 (8) (1996) 352–358.

[28] M. Nedergaard, S. A. Goldman, Glymphatic failure as a final common pathway to dementia, Science 370 (6512) (2020) 50–56.

[29] R. Mathias, J. Rae, R. Eisenberg, The lens as a nonuniform spherical syncytium, Biophysical journal 34 (1) (1981) 61–83.

[30] S. McLAUGHLIN, R. T. Mathias, Electro-osmosis and the reabsorption of fluid in renal proximal tubules., The Journal of general physiology 85 (5) (1985) 699–728.

[31] D. T. K. Malcolm, A computational model of the ocular lens, Ph.D. thesis, ResearchSpace@ Auckland (2006).

[32] E. Vaghefi, D. T. Malcolm, M. D. Jacobs, P. J. Donaldson, Development of a 3d finite element model of lens microcirculation, Biomedical engineering online 11 (1) (2012) 69.

[33] E. Vaghefi, N. Liu, P. J. Donaldson, A computer model of lens structure and function predicts experimental changes to steady state properties and circulating currents, Biomedical engineering online 12 (1) (2013) 85.

[34] J. Gao, X. Sun, V. Yatsula, R. Wymore, R. Mathias, Isoform-specific function and distribution of na/k pumps in the frog lens epithelium, The Journal of membrane biology 178 (2) (2000) 89–101.

[35] O. Candia, P. Bentley, C. Mills, H. Toyofuku, Asymmetrical distribution of the potential difference in the toad lens, Nature 227 (5260) (1970) 852–853.

[36] O. Candia, R. Gerometta, Fluid movement across the surface of the isolated bovine lens, Investigative Ophthalmology & Visual Science 44 (13) (2003) 3455–3455.

[37] O. A. Candia, L. J. Alvarez, Water and ion transport in ocular tissues, Physiol Mini-Rev 1 (2006) 48–57.

[38] J. Fischbarg, F. P. Diecke, K. Kuang, B. Yu, F. Kang, P. Iserovich, Y. Li, H. Rosskothen, J. P. Koniarek, Transport of fluid by lens epithelium, American Journal of Physiology-Cell Physiology 276 (3) (1999) C548–C557.

[39] A. M. DeRosa, F. J. Martinez-Wittinghan, R. T. Mathias, T. W. White, Intercellular communication in lens development and disease, in: Gap Junctions in Development and Disease, Springer, 2005, pp. 173–195.

[40] D. Mackay, A. Ionides, Z. Kibar, G. Rouleau, V. Berry, A. Moore, A. Shiels, S. Bhattacharya, Connexin46 mutations in autosomal dominant congenital cataract, The American Journal of Human Genetics 64 (5) (1999) 1357–1364.

[41] P. Donaldson, J. Kistler, R. T. Mathias, Molecular solutions to mammalian lens transparency, Physiology 16 (3) (2001) 118–123.

[42] R. T. Mathias, J. Kistler, P. Donaldson, The lens circulation, Journal of Membrane Biology 216 (1) (2007) 1–16.

[43] P. Causin, G. Guidoboni, A. Harris, D. Prada, R. Sacco, S. Terragni, A poroelastic model for the perfusion of the lamina cribrosa in the optic nerve head, Mathematical biosciences 257 (2014) 33–41.

[44] I. A. Sigal, J. G. Flanagan, I. Tertinegg, C. R. Ethier, Finite element modeling of optic nerve head biomechanics, Investigative ophthalmology & visual science 45 (12) (2004) 4378–4387.

[45] N. M. Jansonius, J. Schiefer, J. Nevalainen, J. Paetzold, U. Schiefer, A mathematical model for describing the retinal nerve fiber bundle trajectories in the human eye: average course, variability, and influence of refraction, optic disc size and optic disc position, Experimental eye research 105 (2012) 70–78.

[46] L. R. Band, C. L. Hall, G. Richardson, O. E. Jensen, J. H. Siggers, A. J. Foss, Intracellular flow in optic nerve axons: a mechanism for cell death in glaucoma, Investigative ophthalmology & visual science 50 (8) (2009) 3750–3758.

[47] D. R. McNeal, Analysis of a model for excitation of myelinated nerve, IEEE Transactions on Biomedical Engineering (4) (1976) 329–337.

[48] M. Oozeer, C. Veraart, V. Legat, J. Delbeke, Simulation of intra-orbital optic nerve electrical stimulation, Medical and Biological Engineering and Computing 43 (5) (2005) 608–617.

[49] D. E. Postnov, L. S. Ryazanova, O. V. Sosnovtseva, Functional modeling of neural–glial interaction, BioSystems 89 (1-3) (2007) 84–91.

[50] K.-Y. Fu, L.-G. Dai, I.-M. Chiu, J.-R. Chen, S.-h. Hsu, Sciatic nerve regeneration by microporous nerve conduits seeded with glial cell line-derived neurotrophic factor or brain-derived neurotrophic factor gene transfected neural stem cells, Artificial organs 35 (4) (2011) 363–372.

[51] S. Bellinger, G. Miyazawa, P. Steinmetz, Submyelin potassium accumulation may functionally block subsets of local axons during deep brain stimulation: a modeling study, Journal of neural engineering 5 (3) (2008) 263.

[52] K. C. Chen, C. Nicholson, Spatial buffering of potassium ions in brain extracellular space, Biophysical journal 78 (6) (2000) 2776–2797.

[53] I. Østby, L. Øyehaug, G. T. Einevoll, E. A. Nagelhus, E. Plahte, T. Zeuthen, C. M. Lloyd, O. P. Ottersen, S. W. Omholt, Astrocytic mechanisms explaining neural-activity-induced shrinkage of extraneuronal space, PLoS computational biology 5 (1) (2009) e1000272.

[54] J. Sibille, K. D. Duc, D. Holcman, N. Rouach, The neuroglial potassium cycle during neurotransmission: role of kir4. 1 channels, PLoS computational biology 11 (3) (2015) e1004137.

[55] A. Bellot-Saez, O. Kekesi, J. W. Morley, Y. Buskila, Astrocytic modulation of neuronal excitability through k+ spatial buffering, Neuroscience & Biobehavioral Reviews 77 (2017) 87–97.

[56] R. Hou, Z. Zhang, D. Yang, H. Wang, W. Chen, Z. Li, J. Sang, S. Liu, Y. Cao, X. Xie, et al., Intracranial pressure (icp) and optic nerve subarachnoid space pressure (onsp) correlation in the optic nerve chamber: the beijing intracranial and intraocular pressure (icop) study, brain research 1635 (2016) 201–208.

[57] Y. Mori, A multidomain model for ionic electrodiffusion and osmosis with an application to cortical spreading depression, Physica D: Nonlinear Phenomena 308 (2015) 94–108.

[58] Y. Zhu, S. Xu, R. S. Eisenberg, H. Huang, A bidomain model for lens microcirculation, Biophysical journal 116 (6) (2019) 1171–1184.

[59] Y. Zhu, S. Xu, R. S. Eisenberg, H. Huang, Optic nerve microcirculation: Fluid flow and electrodiffusion, Physics of Fluids 33 (4) (2021) 041906.

[60] Y. Zhu, S. Xu, R. S. Eisenberg, H. Huang, A tridomain model for potassium clearance in optic nerve of necturus, Biophysical Journal (2021),doi:https://doi.org/10.1016/j.bpj.2021.06.020.

[61] O. R. Levine, R. B. Mellins, R. M. Senior, A. P. Fishman, The application of starling's law of capillary exchange to the lungs, The Journal of clinical investigation 46 (6) (1967) 934–944.

[62] B. Eisenberg, Life's solutions are complex fluids. a mathematical challenge, arXiv preprint arXiv:1207.4737.

[63] B. Eisenberg, Interacting ions in biophysics: real is not ideal, Biophysical journal 104 (9) (2013) 1849–1866.

[64] S. Xu, B. Eisenberg, Z. Song, H. Huang, Osmosis through a semi-permeable membrane: a consistent approach to interactions, arXiv preprint arXiv:1806.00646.

[65] L. Wan, S. Xu, M. Liao, C. Liu, P. Sheng, Self-consistent approach to global charge neutrality in electrokinetics: A surface potential trap model, Physical Review X 4 (1) (2014) 011042.

[66] Z. Song, X. Cao, H. Huang, Electroneutral models for dynamic poisson-nernst-planck systems, Physical Review E 97 (1) (2018) 012411.

[67] J. Gao, X. Sun, T. W. White, N. A. Delamere, R. T. Mathias, Feedback regulation of intracellular hydrostatic pressure in surface cells of the lens, Biophysical journal 109 (9) (2015) 1830–1839.

[68] C. Nicholson, Diffusion and related transport mechanisms in brain tissue, Reports on progress in Physics 64 (7) (2001) 815.

[69] J. B. Jonas, E. Berenshtein, L. Holbach, Anatomic relationship between lamina cribrosa, intraocular space, and cerebrospinal fluid space, Investigative ophthalmology & visual science 44 (12) (2003) 5189–5195.

[70] J. J. Feher, Quantitative human physiology: an introduction, Academic press, 2017.

[71] B. Eisenberg, Y. Hyon, C. Liu, Energy variational analysis of ions in water and channels: Field theory for primitive models of complex ionic fluids, The Journal of Chemical Physics 133 (10) (2010) 104104.

[72] M. Pérez-Pinzón, L. Tao, C. Nicholson, Extracellular potassium, volume fraction, and tortuosity in rat hippocampal ca1, ca3, and cortical slices during ischemia, Journal of Neurophysiology 74 (2) (1995) 565–573.

[73] R. E. Norman, J. G. Flanagan, I. A. Sigal, S. M. Rausch, I. Tertinegg, C. R. Ethier, Finite element modeling of the human sclera: influence on optic nerve head biomechanics and connections with glaucoma, Experimental eye research 93 (1) (2011) 4–12.

[74] B. S. Gardiner, D. W. Smith, M. Coote, J. G. Crowston, Computational modeling of fluid flow and intra-ocular pressure following glaucoma surgery, PLoS One 5 (10) (2010) e13178.

[75] N. Wang, Intraocular and Intracranial Pressure Gradient in Glaucoma, Vol. 1, Springer, 2019.

[76] I. A. Sigal, J. G. Flanagan, C. R. Ethier, Factors influencing optic nerve head biomechanics, Investigative ophthalmology & visual science 46 (11) (2005) 4189–4199.

[77] R. Fitzhugh, Thresholds and plateaus in the hodgkin-huxley nerve equations, The Journal of general physiology 43 (5) (1960) 867–896.

[78] A. L. Hodgkin, A. F. Huxley, B. Katz, Measurement of current-voltage relations in the membrane of the giant axon of loligo, The Journal of physiology 116 (4) (1952) 424.

[79] R. Keynes, The ionic movements during nervous activity, The Journal of physiology 114 (1-2) (1951) 119.

[80] I. Dietzel, U. Heinemann, G. Hofmeier, H. Lux, Stimulus-induced changes in extracellular na+ and cl- concentration in relation to changes in the size of the extracellular space, Experimental brain research 46 (1) (1982) 73–84.

[81] J. M. Smith, D. P. Bradley, M. F. James, C. L.-H. Huang, Physiological studies of cortical spreading depression, Biological Reviews 81 (4) (2006) 457–481.

[82] J. P. Dreier, C. Reiffurth, The stroke-migraine depolarization continuum, Neuron 86 (4) (2015) 902–922.

[83] S. Murakami, Y. Kurachi, Mechanisms of astrocytic k+ clearance and swelling under high extracellular k+ concentrations, The Journal of Physiological Sciences 66 (2) (2016) 127–142.

[84] M. J. Sætra, G. Halnes, G. T. Einevoll, An electrodiffusive neuron-extracellular-glia model with somatodendritic interactions, bioRxiv.

[85] D. Stenesen, A. T. Moehlman, J. N. Schellinger, A. R. Rodan, H. Krämer, The glial sodium-potassium-2-chloride cotransporter is required for synaptic transmission in the drosophila visual system, Scientific reports 9 (1) (2019) 1–15.

[86] A. Verkhratsky, A. Butt, Glial physiology and pathophysiology, John Wiley & Sons, 2013.

[87] B. A. Macvicar, D. Feighan, A. Brown, B. Ransom, Intrinsic optical signals in the rat optic nerve: role for k+ uptake via nkcc1 and swelling of astrocytes, Glia 37 (2) (2002) 114–123.

[88] G. Su, D. B. Kintner, M. Flagella, G. E. Shull, D. Sun, Astrocytes from na+-k+-cl-cotransporter-null mice exhibit absence of swelling and decrease in eaa release, American Journal of Physiology-Cell Physiology 282 (5) (2002) C1147–C1160.

[89] P. K. Lauf, N. C. Adragna, K-cl cotransport: properties and molecular mechanism, Cellular Physiology and Biochemistry 10 (5-6) (2000) 341–354.

[90] K. Susuki, Myelin: a specialized membrane for cell communication, Nature Education 3 (9) (2010) 59.

[91] S. Chiu, J. Ritchie, R. Rogart, D. Stagg, A quantitative description of membrane currents in rabbit myelinated nerve., The Journal of physiology 292 (1) (1979) 149–166.

[92] S. Wise, J. Kim, J. Lowengrub, Solving the regularized, strongly anisotropic cahn–hilliard equation by an adaptive nonlinear multigrid method, Journal of Computational Physics 226 (1) (2007) 414–446.

[93] H. Bracho, P. Orkand, R. Orkand, A further study of the fine structure and membrane properties of neuroglia in the optic nerve of necturus, Journal of neurobiology 6 (4) (1975) 395–410.

[94] C. Pilgrim, I. Reisert, D. Grab, Volume densities and specific surfaces of neuronal and glial tissue elements in the rat supraoptic nucleus, Journal of Comparative Neurology 211 (4) (1982) 427–431.

[95] Y.-B. Lu, K. Franze, G. Seifert, C. Steinhäuser, F. Kirchhoff, H. Wolburg, J. Guck, P. Janmey, E.-Q. Wei, J. Käs, et al., Viscoelastic properties of individual glial cells and neurons in the cns, Proceedings of the National Academy of Sciences 103 (47) (2006) 17759–17764.

[96] R. Villegas, G. M. Villegas, Characterization of the membranes in the giant nerve fiber of the squid, The Journal of general physiology 43 (5) (1960) 73.

Appendix A

Supporting information for lens model

A.1 Non-dimensionalization

In this section, we derive the dimensionless model based on the Na/K pump strength on the surface of the lens. Although we restrict ourselves in this particular problem, the following procedure can be applied in a wide range of practical problems in biological syncytia.

Water circulation

In the following, we assume the typical length scale of the lens is R. The fluid system is driven by the osmotic gradient generated by the Na/K pump on the surface membrane of the lens. In Equation (2.7), the strength of the Na/K pump at the surface depends on the ion's concentration, which leads

$$J_p^{Na} = 3\frac{I_p}{e}, \quad J_p^K = -2\frac{I_p}{e}, \quad J_p^{Cl} = 0, \tag{A.1}$$

where

$$I_p = I_{max,1}\left(\frac{c_{in}^{Na}}{c_{in}^{Na}+K_{Na1}}\right)^3\left(\frac{c_o^K}{c_o^K+K_{K1}}\right)^2 + I_{max,2}\left(\frac{c_{in}^{Na}}{c_{in}^{Na}+K_{Na2}}\right)^3\left(\frac{c_o^K}{c_o^K+K_{K2}}\right)^2. \tag{A.2}$$

We assume that the velocity at the surface determines the characteristic velocity scale for the problem. At surface boundary of the intracellular space, due to the Na/K pump in Equation (A.1) and the assumption of conductance at surface such that $G^{Na} = G^{Cl} = 0$ in [1, 3], we have the ion fluxes at intracellular boundary $r = R$ as

$$j_{in}^{Na} = J_p^{Na}, \quad j_{in}^K = J_s^K + J_p^K, \quad j_{in}^{Cl} = 0. \tag{A.3}$$

Since the $g^K = 0$ on the cell membrane inside of the lens, we obtain the following Na^+ flux balance between the ion channel and Na/K pump at steady state as

$$J_s^K + J_p^K = 0. \tag{A.4}$$

This assumption will obviously have to be replaced in applications to other tissues, with a less particular channel protein distribution. By the conservation of fluxes for each ion in Equation (2.4) and non-flux boundary condition at $r = 0$, we get

$$j_{in}^{i} = -\delta_0 j_{ex}^{i}, \quad i = \mathrm{Na}^+, \mathrm{K}^+, \mathrm{Cl}^-, \tag{A.5}$$

where $\delta_0 = \frac{\mathcal{M}_{ex}}{\mathcal{M}_{in}}$. Therefore, Equation (A.3) becomes

$$-\delta_0 j_{ex}^{Na} = J_p^{Na}, \quad -\delta_0 j_{ex}^{K} = 0, \quad -\delta_0 j_{ex}^{Cl} = 0. \tag{A.6}$$

The ion's diffusion coefficient in the extracellular region is approximately at the same level, i.e.

$$D_{ex}^{i} = O\left(D_{ex}\right), \quad i = \mathrm{Na}^+, \mathrm{K}^+, \mathrm{Cl}^-. \tag{A.7}$$

By adding up all three fluxes in Equation (A.6) and Equation (2.10), we get

$$O_{ex} u_{in} + \delta_0 D_{ex} \tau_{ex} \frac{d}{dr} O_{ex} + \delta_0 \frac{D_{ex} \tau_{ex}}{k_B T} \rho_{ex} \frac{d}{dr} \phi_{ex} = J_p^{Na}, \tag{A.8}$$

where $\rho_{ex} = \frac{\mathcal{M}_v C_m}{1-\eta_{in}} \left(\phi_{ex} - \phi_{in}\right)$. In the Equation (A.8), we have used the relation between intracellular and extracellular velocities,

$$u_{in} = -\delta_0 u_{ex}, \tag{A.9}$$

derived from Equation (2.1b) and boundary condition that $u_{ex} = u_{in} = 0$ at $r = 0$. The strength of the ion pump J_p^{Na} depends on the ion concentration in Equation (A.2). In the steady state, we choose the scale of J_p^{Na} is J_p^{Na*} based on an experimental estimation [3]. By using Equation (A.8), we take the scale for u_{in} to be u_{in}^* as

$$u_{in}^* = \frac{J_p^{Na*}}{O^*}. \tag{A.10}$$

where $O^* = 2\left(c_o^{Na} + c_o^{K}\right)$. By mass conservation expressed in Equation (A.9), we naturally get the scale for u_{ex} as

$$u_{ex}^* = \delta_0^{-1} u_{in}^*. \tag{A.11}$$

Furthermore, we choose the scale of electric potential ϕ_{in} and ϕ_{ex} as $\phi^* = \frac{k_B T}{e}$. For the extracellular velocity in Equation (2.2), we have

$$u_{ex}^* \widetilde{u}_{ex} = -\frac{\kappa_{ex}}{\mu R} \tau_{ex} p_{ex}^* \frac{d}{d\widetilde{r}} \widetilde{p}_{ex} - k_e \tau_{ex} \frac{k_B T}{eR} \frac{d}{d\widetilde{r}} \widetilde{\phi}_{ex}, \tag{A.12}$$

In the Equation (A.12), we think the hydrostatic pressure term balances the extracellular velocity u_{ex} and choose the scale for extracellular pressure p_{ex}^* as

$$p_{ex}^* = \frac{\mu R u_{ex}^*}{\kappa_{ex} \tau_{ex}}.$$

Therefore, Equation (A.12) becomes

$$\widetilde{u}_{ex} = -\frac{d}{d\widetilde{r}}\widetilde{p}_{ex} - \delta_1 \frac{d}{d\widetilde{r}}\widetilde{\phi}_{ex}, \tag{A.13}$$

where $\delta_1 = \frac{k_e \tau_{ex} k_B T}{e u^*_{ex} R}$. For the intracellular velocity, we have

$$u^*_{in}\widetilde{u}_{in} = -\frac{\kappa_{in} p^*_{in}}{\mu R}\frac{d}{d\widetilde{r}}\widetilde{p}_{in} + \frac{\kappa_{in}\gamma_m k_B T O^*}{\mu R}\frac{d}{d\widetilde{r}}\widetilde{O}_{in}. \tag{A.14}$$

We choose the intracellular hydrostatic pressure scale (p^*_{ex}) is the same as extracellular one (p^*_{in}), such that

$$p^* = p^*_{in} = p^*_{ex}.$$

In this way, Equation (A.14) becomes

$$\delta_2 \widetilde{u}_{in} = -\delta_3 \frac{d}{d\widetilde{r}}\widetilde{p}_{in} + \frac{d}{d\widetilde{r}}\widetilde{O}_{in}, \tag{A.15}$$

where

$$\delta_2 = \frac{\mu u^*_{in} R}{\kappa_{in}\gamma_m k_B T O^*}, \qquad \delta_3 = \frac{p^*}{\gamma_m k_B T O^*}.$$

In all, the fluid system (2.1) becomes

$$\begin{cases} \widetilde{u}_{ex} = -\widetilde{u}_{in}, \\ \delta_4 \dfrac{1}{\widetilde{r}^2}\dfrac{d}{d\widetilde{r}}\left(\widetilde{r}^2 \widetilde{u}_{in}\right) = \delta_3\left(\widetilde{p}_{ex} - \widetilde{p}_{in}\right) + \left(\widetilde{O}_{in} - \widetilde{O}_{ex}\right), \end{cases} \tag{A.16}$$

with boundary conditions

$$\begin{cases} \widetilde{p}_{ex} = 0, \\ \delta_5 \widetilde{u}_{in} = \delta_3 \widetilde{p}_{in} - \left(\widetilde{O}_{in} - \widetilde{O}_{ex}\right), \end{cases}$$

where

$$\delta_4 = \frac{\mathcal{M}_{in} u^*_{in}}{R\mathcal{M}_v L_m \gamma_m k_B T O^*}, \quad \delta_5 = \frac{u^*_{in}}{L_s \gamma_s k_B T O^*}.$$

Ions circulation

The velocity scales and diffusion coefficients in the extracellular and intracellular spaces are at different levels of approximation in our approach. In the following, we put the characteristic diffusion coefficients in the intracellular and extracellular regions and the scales of concentrations as

$$D^*_{ex} = D^{Cl}_{ex}\tau_{ex}, \quad D^*_{in} = D^{Cl}_{in}, \quad c^* = c^{Na}_o + c^K_o.$$

In this way, we get the Peclet numbers in the extracellular and intracellular as

$$Pe_{in} = \frac{u^*_{in} R}{D^*_{in}}, \quad Pe_{ex} = \frac{u^*_{ex} R}{D^*_{ex}}.$$

We introduce the dimensionless intracellular and extracellular ith specie ion fluxes as

$$\widetilde{j}^i_{in} = Pe_{in} \widetilde{c}^i_{in} \widetilde{u}_{in} - \widetilde{D}^i_{in} \left(\frac{d}{d\widetilde{r}} \widetilde{c}^i_{in} + z^i \widetilde{c}^i_{in} \frac{d}{d\widetilde{r}} \widetilde{\phi}_{in} \right),$$
$$\widetilde{j}^i_{ex} = Pe_{ex} \widetilde{c}^i_{ex} \widetilde{u}_{ex} - \widetilde{D}^i_{ex} \left(\frac{d}{d\widetilde{r}} \widetilde{c}^i_{ex} + z^i \widetilde{c}^i_{ex} \frac{d}{d\widetilde{r}} \widetilde{\phi}_{ex} \right).$$

Since $g^K = 0$ on the cell membrane inside of lens, we have K^+ governing system as in Mathias's model [3],

$$\begin{cases} \dfrac{1}{\widetilde{r}^2} \dfrac{d}{d\widetilde{r}} \left(\widetilde{r}^2 \widetilde{j}^K_{ex} \right) = 0, \\ \dfrac{1}{\widetilde{r}^2} \dfrac{d}{d\widetilde{r}} \left(\widetilde{r}^2 \widetilde{j}^K_{in} \right) = 0, \end{cases} \tag{A.17}$$

with boundary conditions at $r = 1$

$$\begin{cases} \widetilde{c}^K_{ex} = \widetilde{c}^K_o, \\ \widetilde{j}^K_{in} = \dfrac{R_s}{z^K} \left(\widetilde{\phi}_{in} - \widetilde{E}^K \right) + \widetilde{J}^K_p. \end{cases}$$

For the Cl^- governing system, we have

$$\begin{cases} \dfrac{1}{\widetilde{r}^2} \dfrac{d}{d\widetilde{r}} \left(\widetilde{r}^2 \widetilde{j}^{Cl}_{ex} \right) = \dfrac{\widetilde{\mathcal{M}}^{ex}_v}{z^{Cl}} \left(\widetilde{\phi}_{in} - \widetilde{\phi}_{ex} - \widetilde{E}^{Cl} \right), \\ \dfrac{1}{\widetilde{r}^2} \dfrac{d}{d\widetilde{r}} \left(\widetilde{r}^2 \widetilde{j}^{Cl}_{in} \right) = -\delta_8 \dfrac{1}{\widetilde{r}^2} \dfrac{d}{d\widetilde{r}} \left(\widetilde{r}^2 \widetilde{j}^{Cl}_{ex} \right), \end{cases} \tag{A.18}$$

with boundary conditions at $r = 1$

$$\begin{cases} \widetilde{c}^{Cl}_{ex} = \widetilde{c}^{Na}_o + \widetilde{c}^K_o + \delta_7 \left(\widetilde{\phi}_{in} - \widetilde{\phi}_{ex} \right), \\ \widetilde{j}^{Cl}_{in} = 0. \end{cases}$$

where

$$\widetilde{E}^i = \frac{1}{z^i} \log \left(\frac{\widetilde{c}^i_{ex}}{\widetilde{c}^i_{in}} \right), \quad R_s = \frac{G^K k_B T R}{e^2 D^*_{in} c^*}, \quad \widetilde{J}^K_p = \frac{J^K_p R}{D^*_{in} c^*},$$

and

$$\widetilde{\mathcal{M}}^{ex}_v = \frac{\mathcal{M}_v g^{Cl} k_B T R^2}{\mathcal{M}_{ex} e^2 D^*_{ex} c^*}, \quad \delta_8 = \frac{\mathcal{M}_{ex} D^*_{ex}}{\mathcal{M}_{in} D^*_{in}}.$$

The intracellular and extracellular Na^+ concentrations can be solved from the following equations

$$\begin{cases} \sum_i z^i \widetilde{c}^i_{in} + z^{in} \widetilde{A}_{in} = \delta_6 \left(\widetilde{\phi}_{in} - \widetilde{\phi}_{ex} \right), \\ \sum_i z^i \widetilde{c}^i_{ex} = -\delta_7 \left(\widetilde{\phi}_{in} - \widetilde{\phi}_{ex} \right), \end{cases} \tag{A.19}$$

where

$$\delta_6 = \frac{\mathcal{M}_v C_m k_B T}{e^2 c^* \eta_{in}}, \quad \delta_7 = \frac{\mathcal{M}_v C_m k_B T}{e^2 c^* (1 - \eta_{in})}. \tag{A.20}$$

From electric potential governing Equation (2.11), by using the fact $z^{Na} = z^K = 1$ and assumption that $g^{Na} = g^{Cl}$ on the membrane inside of the lens and $G^{Na} = G^{Cl} = 0$ at surface membrane, we have

$$\begin{cases} \frac{1}{\widetilde{r}^2} \frac{d}{d\widetilde{r}} \left(\widetilde{r}^2 \left(Pe_{ex} \widetilde{\rho}_{ex} \widetilde{u}_{ex} - \sum_i \widetilde{D}^i_{ex} z^i \frac{d}{d\widetilde{r}} \widetilde{c}^i_{ex} - \widetilde{\sigma}_{ex} \frac{d}{d\widetilde{r}} \widetilde{\phi}_{ex} \right) \right) \\ \qquad = \widetilde{\mathcal{M}}^{ex}_v \left(2 \left(\widetilde{\phi}_{in} - \widetilde{\phi}_{ex} \right) - \widetilde{E}^{Na} - \widetilde{E}^{Cl} \right), \\ \frac{1}{\widetilde{r}^2} \frac{d}{d\widetilde{r}} \left(\widetilde{r}^2 \left(Pe_{in} \widetilde{\rho}_{in} \widetilde{u}_{in} - \sum_i \widetilde{D}^i_{in} z^i \frac{d}{d\widetilde{r}} \widetilde{c}^i_{in} - \widetilde{\sigma}_{in} \frac{d}{d\widetilde{r}} \widetilde{\phi}_{in} \right) \right) \\ \qquad = -\delta_8 \frac{1}{\widetilde{r}^2} \frac{d}{d\widetilde{r}} \left(\widetilde{r}^2 \left(Pe_{ex} \widetilde{\rho}_{ex} \widetilde{u}_{ex} - \sum_i \widetilde{D}^i_{ex} z^i \frac{d}{d\widetilde{r}} \widetilde{c}^i_{ex} - \widetilde{\sigma}_{ex} \frac{d}{d\widetilde{r}} \widetilde{\phi}_{ex} \right) \right), \end{cases} \tag{A.21}$$

with boundary conditions

$$\begin{cases} \widetilde{\phi}_{ex} = 0, \\ Pe_{in} \widetilde{\rho}_{in} \widetilde{u}_{in} - \sum_i \widetilde{D}^i_{in} z^i \frac{d}{d\widetilde{r}} \widetilde{c}^i_{in} - \widetilde{\sigma}_{in} \frac{d}{d\widetilde{r}} \widetilde{\phi}_{in} = R_s \left(\widetilde{\phi}_{in} - \widetilde{E}^K \right) + \widetilde{I}^{\phi}_p, \end{cases} \tag{A.22}$$

where

$$\widetilde{\rho}_{in} = |z^{in}| \widetilde{A}_{in} + \delta_6 \left(\widetilde{\phi}_{in} - \widetilde{\phi}_{ex} \right), \quad \widetilde{\rho}_{ex} = \delta_7 \left(\widetilde{\phi}_{ex} - \widetilde{\phi}_{in} \right), \quad \widetilde{I}^{\phi}_p = \frac{I_p R}{e D^*_{in} c^*},$$

and

$$\widetilde{\sigma}_{in} = \sum_i \widetilde{D}^i_{in} (z^i)^2 \widetilde{c}^i_{in}, \qquad \widetilde{\sigma}_{ex} = \sum_i \widetilde{D}^i_{ex} (z^i)^2 \widetilde{c}^i_{ex}, \qquad \delta_8 = \frac{\mathcal{M}_{ex} D^*_{ex}}{\mathcal{M}_{in} D^*_{in}}.$$

In the dimensionless system (2.14), we remove the tilde for simplicity.

A.2 A priori estimation

In this section, we first provide the priori estimation of the j_{in}^{Cl} as follows. By using the homogeneous Neumann boundary condition at $r = 0$, the Equation (2.14l) yields

$$\begin{aligned}\frac{d}{dr}\phi_{in} =& \frac{1}{\sigma_{in}}\left(Pe_{in}\rho_{in}u_{in} + \delta_9\frac{d}{dr}c_{in}^{K} + \delta_{10}\frac{d}{dr}c_{in}^{Na}\right) \\ &+ \frac{\delta_8}{\sigma_{in}}\left(Pe_{ex}\rho_{ex}u_{ex} + \delta_9\frac{d}{dr}c_{ex}^{K} + \delta_{10}\frac{d}{dr}c_{ex}^{Na} - \sigma_{ex}\frac{d}{dr}\phi_{ex}\right) + o(\epsilon^2).\end{aligned} \tag{A.23}$$

where

$$\delta_9 = D_l^{Cl} - D_l^{K}, \quad \delta_{10} = D_l^{Cl} - D_l^{Na},$$

and we use the fact that $\{\delta_6, \delta_7\} \subset o(\epsilon^2)$ in Equations (2.14e) and (2.14f) and A_{in} is a constant. Based on Equation (A.23), we obtain that

$$\frac{d}{dr}\phi_{in} = O(\epsilon), \tag{A.24}$$

since $\{Pe_{in}, \delta_8, \delta_{10}\} \subset O(\epsilon)$ and $\delta_9 = O(\epsilon^2)$. At the same time, in Equation (2.14b), we have

$$\frac{d}{dr}O_{in} = O(\epsilon^2), \tag{A.25}$$

since $\delta_2 = o(\epsilon^2)$ and $\delta_3 = O(\epsilon^2)$. In Equation (2.14e), we have

$$\frac{d}{dr}c_{in}^{Cl} = \frac{d}{dr}\left(c_{in}^{Na} + c_{in}^{K}\right) + o(\epsilon^2). \tag{A.26}$$

With Equations (A.25) and (A.26) and the negative charged protein A_{in} is uniformly distributed, we yield that

$$\frac{d}{dr}c_{in}^{Cl} = O(\epsilon^2). \tag{A.27}$$

With Equations (2.14c) and (2.14e) and boundary conditions for c_{ex}^{Cl} in Equation (2.15)

$$c_{in}^{Cl} = c_o^{Na} + c_o^{K} - \frac{1 + |z^{in}|}{2}A_{in} + O(\epsilon^2). \tag{A.28}$$

From the experimental setting of the lens [3, 31], we have

$$c_o^{Na} + c_o^{K} - \frac{1 + |z^{in}|}{2}A_{in} = O(\epsilon). \tag{A.29}$$

In this way, we obtain

$$c_{in}^{Cl} = O(\epsilon). \tag{A.30}$$

In all, based on Equations (A.27) and (A.30), we claim that

$$\begin{aligned} J_{in}^{Cl} &= Pe_{in} c_{in}^{Cl} u_{in} - D_{in}^{Cl} \left(\frac{d}{dr} c_{in}^{Cl} + z^{Cl} c_{in}^{Cl} \frac{d}{dr} \phi_{in} \right) \\ &= O(\epsilon^2). \end{aligned} \tag{A.31}$$

By dropping the terms involving the small parameters (smaller or equal $O(\epsilon^2)$), the leading order of water circulation system (2.14a)-(2.14d) is as follows,

$$u_{ex}^0 = -\frac{d}{dr} p_{ex}^0 - \delta_1 \frac{d}{dr} \phi_{ex}^0, \tag{A.32a}$$

$$\frac{d}{dr} O_{in}^0 = 0, \tag{A.32b}$$

$$O_{in}^0 - O_{ex}^0 = 0, \tag{A.32c}$$

$$u_{ex}^0 = -u_{in}^0, \tag{A.32d}$$

where we use the superscript '0' denotes the leading order approximation. From Equation (A.32), we deduce $O_{ex}^0 = O_{in}^0$ are constants, and the intracellular and extracellular flow are counterflow. The leading order of total charge in both intracellular and extracellular regions are neutral

$$\sum_i z^i c_{in}^{i,0} + z^{in} A_{in} = 0, \tag{A.33a}$$

$$\sum_i z^i c_{ex}^{i,0} = 0. \tag{A.33b}$$

Combining constant osmotic pressure in Equation (A.32) and charge neutrality Equation (A.33) yields

$$O_{ex}^0 = O_{in}^0 = 2 \left(c_0^{Na} + c_0^K \right), \tag{A.34a}$$

$$\frac{dc_{in}^{Cl,0}}{dr} = \frac{dc_{ex}^{Cl,0}}{dr} = 0, \tag{A.34b}$$

the c_0^{Na} and c_0^K are Na^+ and K^+ concentrations at extracellular boundary $r = 1$. Based on Equation (A.34), we have $c_{in}^{Cl,0}$ and $c_{ex}^{Cl,0}$ are constants and

$$\frac{dc_l^{Na,0}}{dr} = -\frac{dc_l^{K,0}}{dr}, \quad l = in, ex. \tag{A.35}$$

The leading order of the K^+ and Cl^- concentrations satisfy

$$\frac{1}{r^2} \frac{d}{dr} \left(r^2 j_{in}^{K,0} \right) = 0, \tag{A.36a}$$

$$\frac{1}{r^2} \frac{d}{dr} \left(r^2 j_{ex}^{K,0} \right) = 0, \tag{A.36b}$$

$$\frac{1}{r^2}\frac{d}{dr}\left(r^2 j_{ex}^{Cl,0}\right) = \frac{\mathcal{M}_v^{ex}}{z^{Cl}}\left(\phi_{in}^0 - \phi_{ex}^0 - E^{Cl,0}\right), \tag{A.36c}$$

$$\frac{1}{r^2}\frac{d}{dr}\left(r^2 j_{in}^{Cl,0}\right) = -\frac{\delta_8}{r^2}\frac{d}{dr}\left(r^2 j_{ex}^{Cl,0}\right), \tag{A.36d}$$

where

$$j_l^{i,0} = Pe_l c_l^{i,0} u_l^0 - D_l^i\left(\frac{d}{dr}c_l^{i,0} + z^i c_l^{i,0}\frac{d}{dr}\phi_l^0\right), \quad i = \mathrm{K}^+, \mathrm{Cl}^-,\ l = in, ex,$$

and

$$E^{i,0} = \frac{1}{z^i}\log\left(\frac{c_{ex}^{i,0}}{c_{in}^{i,0}}\right), \quad i = \mathrm{K}^+, \mathrm{Cl}^-.$$

At the same time, based on Equation (2.14j) for the intracellular K^+ and the homogeneous Neumann boundary condition at $r = 0$,we have

$$D_{in}^K\frac{d}{dr}c_{in}^K = Pe_{in}c_{in}^K u_{in} - D_{in}^K z^K c_{in}^K\frac{d}{dr}\phi_{in}. \tag{A.37}$$

By substituting Equation (A.23) into Equation (A.37), it yields

$$\left(1 - \delta_{10}\frac{z^K c_{in}^K}{\sigma_{in}}\right)D_{in}^K\frac{dc_{in}^K}{dr} = \left(\left(1 - z^K D_{in}^K\frac{\rho_{in}}{\sigma_{in}}\right)Pe_{in}u_{in} + \delta_8\frac{z^K D_{in}^K\sigma_{ex}}{\sigma_{in}}\frac{d\phi_{ex}}{dr}\right)c_{in}^K + O(\epsilon^2), \tag{A.38}$$

where we used that fact that $\rho_{ex} = o(\epsilon^2)$, $\delta_9 = O(\epsilon^2)$ and

$$\frac{dc_{in}^K}{dr} = -\frac{dc_{in}^{Na}}{dr} + O(\epsilon^2).$$

Based on Equation (A.38), we have

$$\frac{dc_{in}^K}{dr} = O(\epsilon), \tag{A.39}$$

since $Pe_{in} = O(\epsilon)$ and $\delta_8 = O(\epsilon)$. By combining Equations (A.23) and (A.39), we obtain the leading order approximation for the intracellular potential

$$\frac{d}{dr}\phi_{in}^0 = \frac{Pe_{in}\rho_0}{\sigma_{in}^0}u_{in}^0 - \frac{\delta_8\sigma_{ex}^0}{\sigma_{in}^0}\frac{d}{dr}\phi_{ex}^0 = O(\epsilon), \tag{A.40}$$

where

$$\sigma_{in}^0 = \sum_i D_{in}^i(z^i)^2 c_{in}^{i,0}, \quad \sigma_{ex}^0 = \sum_i D_{ex}^i(z^i)^2 c_{ex}^{i,0}.$$

In the similar way, the leading order approximation of extracellular potential is

$$-\frac{1}{r^2}\frac{d}{dr}\left(r^2\left(\delta_{10}\frac{d}{dr}c_{ex}^{Na,0} + \sigma_{ex}^0\frac{d}{dr}\phi_{ex}^0\right)\right) = \mathcal{M}_v^{ex}\left(2\left(\phi_{in}^0 - \phi_{ex}^0\right) - E^{Na,0} - E^{Cl,0}\right), \tag{A.41}$$

where $E^{Na,0} = \frac{1}{z^{Na}}\log\left(\frac{c_{ex}^{Na,0}}{c_{in}^{Na,0}}\right)$. In all, we summary the above leading order system in the (2.18).

A.3 Effect of permeability

In this section, we compare the variation of the extracellular variables, by increasing the membrane permeability κ_{in}. In Figure (A.1), we show how the extracellular hydrostatic pressure, osmosis, electrical potential, and velocity changes when κ_{in} equals κ_{in}^{w}, $2\kappa_{in}^{w}$ and $20\kappa_{in}^{w}$.

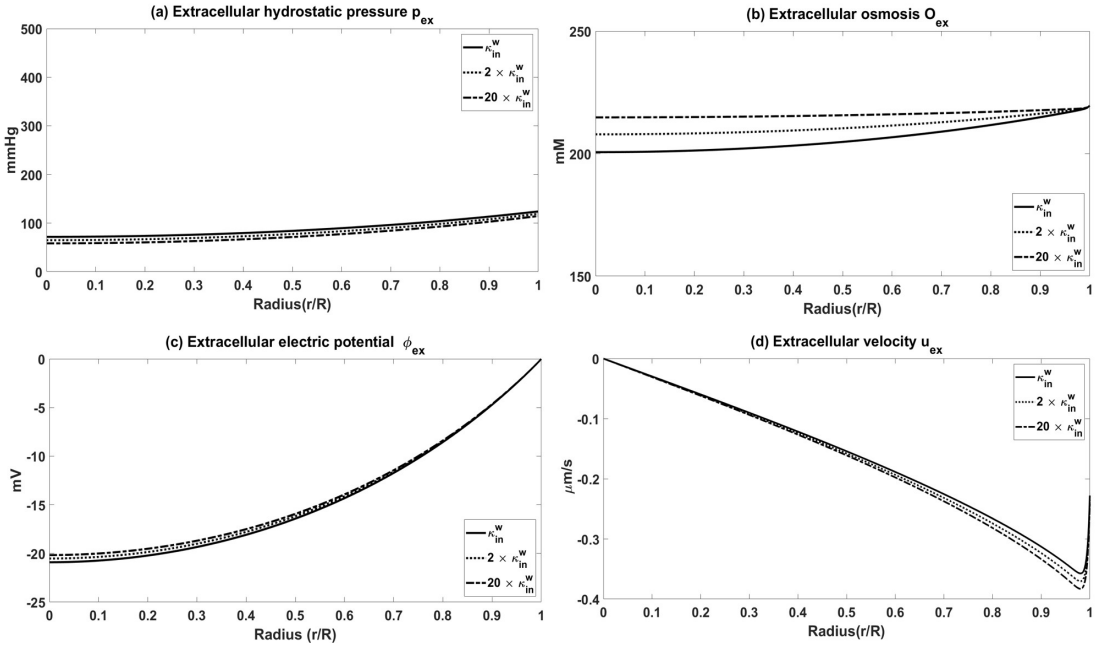

Figure A.1: Comparison between different κ_{in} for extracellular variables.

A.4 Parameters in lens model

The parameters for the lens model are given in Table A.1. We provide the dimensionless parameters' expression and value in Table A.2. The scale calculation based on parameters' value in [31].

Table A.1: Parameters in Lens Model

Parameters	Mathias [3]	Malcolm [31]	Parameters	Mathias [3]	Malcolm [31]
R	1.6×10^{-3} m	1.6×10^{-3} m	L_m	3.75×10^{-13} m/(Pa · s)	1.34×10^{-13} m/(Pa · s)
A_{in}	78 mM	78 mM	L_s	3.75×10^{-13} m/(Pa · s)	8.89×10^{-13} m/(Pa · s)
c_o^{Na}	107 mM	107 mM	$\mathcal{M}_{in}$	0.988	0.99
c_o^K	3 mM	3 mM	$\mathcal{M}_{ex}$	0.012	0.01
C_m	-	1×10^{-2} F/m^2	$\mathcal{M}_v$	6×10^5 /m	5×10^5 /m
D_{ex}^{Na}	-	1.39×10^{-9} m^2/s	T	-	310 K
D_{ex}^K	-	2.04×10^{-9} m^2/s	k_e	1.72×10^{-8} m^2/(V · s)	1.45×10^{-8} m^2/(V · s)
D_{ex}^{Cl}	-	2.12×10^{-9} m^2/s	k_B	1.38×10^{-23} J/K	1.38×10^{-23} J/K
D_{in}^{Na}	-	1.39×10^{-11} m^2/s	K_{K1}	-	1.6154 mM
D_{in}^K	-	2.04×10^{-11} m^2/s	K_{K2}	-	0.1657 mM
D_{in}^{Cl}	-	2.12×10^{-11} m^2/s	$K_{Na1,Na2}$	-	2.3393 mM
e	1.6×10^{-19} $A \cdot s$	1.6×10^{-19} A · s	η_{in}	0.988	0.99
g^{Na}	2.2×10^{-3} S/m^2	2.2×10^{-3} S/m^2	κ_{ex}	1.141×10^{-16} m^2	1.33×10^{-16} m^2
g^{Cl}	2.2×10^{-3} S/m^2	2.2×10^{-3} S/m^2	κ_{in}	-	9.366×10^{-19} m^2
G^K	2.1 S/m^2	2.1 S/m^2	$\gamma_{m,s}$	1	1
I_p	2.3×10^{-2} A/m^2	-	τ_{ex}	0.16	0.16
$I_{max,1}$	-	0.478 A/m^2	μ	7×10^{-4} Pa · s	7×10^{-4} Pa · s
$I_{max,2}$	-	0.065 A/m^2	z^{in}	-1.5	-1.5

Table A.2: Dimensionless Parameters and Scales

Scales/Parameters	Value	Parameters	Value
J_p^{Na*}	6.9×10^{-2}A/m^2	$\delta_0 = \frac{\mathcal{M}_{ex}}{\mathcal{M}_{in}}$	$\frac{1}{99}$
c^*	110 mM	$\delta_1 = \frac{k_e \tau_{ex} k_B T}{e u_{ex}^* R}$	1.2031×10^{-1}
O^*	220 mM	$\delta_2 = \frac{\mu R u_{in}^*}{\kappa_{in} \gamma_m k_B T O^*}$	6.861×10^{-3}
p^*	16.937 KPa	$\delta_3 = \frac{p^*}{\gamma_m k_B T O^*}$	2.9894×10^{-2}
u_{in}^*	3.2506 nm/s	$\delta_4 = \frac{\mathcal{M}_{in} u_{in}^*}{R \mathcal{M}_v L_m \gamma_m k_B T O^*}$	3.5323×10^{-5}
u_{ex}^*	3.2181 μm/s	$\delta_5 = \frac{u_{in}^*}{L_s \gamma_s k_B T O^*}$	4.3022×10^{-3}
ϕ^*	26.7 mV	$\delta_6 = \frac{\mathcal{M}_v C_m k_B T}{e^2 c^* \eta_{in}}$	1.2745×10^{-5}
D_{ex}^*	3.392×10^{10} m^2/s	$\delta_7 = \frac{\mathcal{M}_v C_m k_B T}{e^2 c^* (1-\eta_{in})}$	1.2617×10^{-3}
D_{in}^*	2.12×10^{-11} m^2/s	$\delta_8 = \frac{\mathcal{M}_{ex} D_{ex}^*}{\mathcal{M}_{in} D_{in}^*}$	1.6162×10^{-1}
$Pe_{ex} = \frac{u_{ex}^* R}{D_{ex}^*}$	1.5180	$\delta_9 = \widetilde{D}_l^{Cl} - \widetilde{D}_l^K$	3.77×10^{-2}
$Pe_{in} = \frac{u_{in}^* R}{D_{in}^*}$	2.4533×10^{-1}	$\delta_{10} = \widetilde{D}_l^{Cl} - \widetilde{D}_l^{Na}$	3.443×10^{-1}
$\widetilde{D}_l^{Na}$	0.6557	$\delta_{11} = \frac{c_{in}^{Cl,0}}{c_{ex}^{Cl,0}}$	$\frac{12.5}{110}$
$\widetilde{D}_l^K$	0.9623	ρ_0	$\frac{117}{110}$
$\widetilde{D}_l^{Cl}$	1	$\widetilde{\mathcal{M}}_v^{in}$	3.3859×10^{-1}
$R_s = \frac{G^K k_B T R}{e^2 D_{in}^* c^*}$	4.00×10^{-1}	$\widetilde{\mathcal{M}}_v^{ex}$	2.095

Note: the subscript 'l' presents either 'in' or 'ex'.

Appendix B

Propagation of action potential in the optic nerve

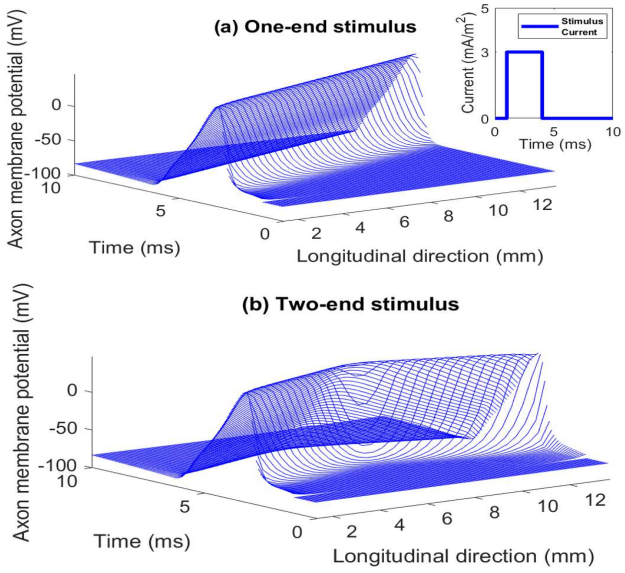

Figure B.1: a: Axon membrane potential profile when eye-end axon stimulated at radius center of the optic nerve. b: Axon membrane potential profile when two-end axon simulated at radius center of the optic nerve.

Figure B.1 shows the propagation of the axon action potential. The membrane potential from axons at the center of the optic nerve bundle is shown when different locations of the axon had been stimulated. In both eye-end and two-end cases, the stimulus current was applied at $t = 1$ ms. In Figure B.1a, the stimulus was applied near to the optic nerve near the eye-end ($z = 1.875$ mm). At $t = 10$ ms, the action potential completely has propagated and left the location near far-eye-end (13.125 mm). The axon in the optic nerve of the mud puppy is unmyelinated. This speed of action potential propagation in the model

lies in the range of the action potential speeds typical of unmyelinated axons, i.e., between 0.5 m/s and 2.0 m/s [90]. In the Figure B.1b, when the two-ends of the axon stimulated, the axon membrane potential has is more uniform spatially at each time point in compare to the single side stimulus case. Presumably, Orkand et al used the dual stimulation to more closely approximate a 'space clamp'.

Appendix C

Analysis in optic nerve model

C.1 Comparison between axon membrane potential and Nernst potential

The classical Hodgkin Huxley analysis of a single action potential [91] assumes that changes in ions concentration are much less critical than current flow in determining the shape of the action potential. In other words, the change in the Nernst potential is much less than the change in the membrane potential. In this section, based on our model, we show that the variation of the Nernst potential for Na^+, K^+ and Cl^- on the axon membrane is much smaller than the axon membrane potential changes during action potentials,

$$\delta E_{ax}^{i} = o\left(\delta V_{ax}^{*}\right), \quad i = \mathrm{Na}^+, \mathrm{K}^+, \mathrm{Cl}^-.$$

During action potentials, the scale of the δV_{ax} can be approximated by the Na^+ and K^+ Nernst potential difference at the resting state,

$$\delta V_{\mathrm{ax}}^{*} = O\left(E_{ax}^{Na,re} - E_{ax}^{K,re}\right). \tag{C.1}$$

We take the Cl^- Nernst potential for example. By the charge neutrality condition in Equation (3.1), we have

$$\delta c_{ax}^{Cl} \approx -\frac{\eta_{ex}}{\eta_{ax}} \delta c_{ex}^{Cl}. \tag{C.2}$$

Therefore, the variation of Cl^- Nernst potential on axon membrane yields

$$\begin{aligned} \delta E_{ax}^{Cl} &= V^* \left(\log\left(\frac{c_{ex}^{Cl,re} + \delta c_{ex}^{Cl}}{c_{ax}^{Cl,re} + \delta c_{ax}^{Cl}} \right) - \log\left(\frac{c_{ex}^{Cl,re}}{c_{ax}^{Cl,re}} \right) \right) \\ &\approx V^* \left(\log\left(1 + \frac{\delta c_{ex}^{Cl}}{c_{ex}^{Cl,re}} \right) - \log\left(1 - \frac{\eta_{ex} \delta c_{ex}^{Cl}}{\eta_{ax} c_{ax}^{Cl,re}} \right) \right), \end{aligned} \tag{C.3}$$

where

$$V^* = \frac{k_B T}{e}, \quad \frac{1}{c_{ex}^{Cl,re}} = O\left(10^{-2}\right), \quad \frac{\eta_{ex}}{\eta_{ax} c_{ax}^{Cl,re}} = O\left(10^{-2}\right).$$

In addition, the characteristic time for a single action potential T_{ax}^* is in millisecond level ($O\left(10^{-3}\right)$), so the scale of δc_{ex}^{Cl} in the stimulated region is

$$\delta c_{ex}^{Cl,*} = \delta c_{ex}^{Na,*} + \delta c_{ex}^{K,*} < O\left(\frac{T_{ax}^* \mathcal{M}_{ax} \bar{g}^{Na} \delta V_{ax}^*}{e\eta_{ex}}\right) = O(1), \tag{C.4}$$

where we use charge neutrality condition and maximum conductance of the voltage-gated Na^+ channel. Therefore, Equation (C.3) yields

$$\delta E_{ax}^{Cl} \approx V^* \left(\frac{1}{c_{ex}^{Cl,re}} + \frac{\eta_{ex}}{\eta_{ax} c_{ax}^{Cl,re}}\right) \delta c_{ex}^{Cl}, \tag{C.5}$$

Based on Equations (C.1), (C.5) and (C.4), and the fact that $\frac{V^*}{\delta V_{ax}^*} = o(1)$, we have $\delta E_{ax}^{Cl} = o\left(\delta V_{ax}^*\right)$. In a similar way, we can get

$$\delta E_{ax}^{i} = o\left(\delta V_{ax}^*\right), \quad i = \mathrm{Na}^+, \mathrm{K}^+. \tag{C.6}$$

C.2 Estimations of t_{m1} and t_{m2}

In this section, we provide estimations on t_{m1} and t_{m2}. For the first time interval parameter t_{m1}, by substituting Equation (4.3), Equation (4.5) into Equation (4.4), we obtain

$$\begin{aligned} m^{dy}(t_{m1}) = m_0 \exp\Bigg(&\frac{18 t_{m1}}{35}\left(\exp\left(\frac{-70}{9}\right) - 1\right) \\ &+ \frac{t_{m1}}{14}\left[\mathrm{Li}_2\left(\exp(x)\right) + x\ln\left(1-\exp(x)\right) - \frac{1}{2}x^2\right]\Big|_{2.5}^{-11.5}\Bigg) \\ &- \frac{t_{m1}}{14}\int_{2.5}^{-11.5} \frac{s}{\exp(s)-1} \exp\left(\frac{18 t_{m1}}{35}\left(\exp\left(-\frac{70}{9}\right) - \exp\left(-\frac{25-10s}{18}\right)\right)\right) \\ &+ \frac{t_{m1}}{14}\left[\mathrm{Li}_2(\exp(x)) + x\ln(1-\exp(x)) - \frac{1}{2}x^2\right]\Big|_{s}^{-11.5}\Bigg) ds, \end{aligned} \tag{C.7}$$

where we use $E_{ax}^{Na,re} - V_{ax}^{re} \approx 1.4 \times 10^2$ mV.
Base on Equation (C.7), we present the estimations of t_{m1} by choosing different open probabilities value for $m^{dy}(t_{m1})$ in Table C.1 below,

Table C.1: Estimation of t_{m1}

$m^{dy}\left(t_{m1}\right)$	0.93	0.95	0.97
t_{m1}	0.57 ms	0.67 ms	0.92 ms

The table above shows that the estimation of t_{m1} through Equation (C.7) has consistent

results. In the similar way, for the second time interval parameter t_{m2}, by substituting Equation (4.3), Equation (4.7) into Equation (4.4), we obtain

$$\begin{aligned} m^{dy}(t_{m2}) =& m_0 \exp\left(\frac{36t_{m2}}{75}\left(\exp\left(\frac{-70}{9}\right)-\exp\left(\frac{5}{9}\right)\right)\right. \\ &\left.+\frac{t_{m2}}{15}\left[\mathrm{Li}_2(\exp(x))+x\ln(1-\exp(x))-\frac{1}{2}x^2\right]\Big|_{3.5}^{-11.5}\right) \\ &+\frac{t_{m2}}{15}\int_{-11.5}^{3.5}\frac{s}{\exp(s)-1}\exp\left(\frac{36t_{m2}}{75}\left(\exp\left(\frac{-(35-10s)}{18}\right)-\exp\left(\frac{5}{9}\right)\right)\right. \\ &\left.+\frac{t_{m2}}{15}\left[\mathrm{Li}_2(\exp(x))+x\ln(1-\exp(x))-\frac{1}{2}x^2\right]\Big|_{3.5}^{s}\right)ds. \end{aligned} \tag{C.8}$$

where we use $E_{ax}^{Na,re} - E_{ax}^{K,re} \approx 1.5 \times 10^2$ mV.
In the second time interval, we choose $m^{dy}(t_{m1}) = 0.95$ as the initial value m_0 in Equation (C.8). Table C.2 shows consistent estimation of the t_{m2} when different value for $m^{dy}(t_{m2})$ has been chosen.

Table C.2: Estimation of t_{m2}

$m^{dy}(t_{m2})$	0.15	0.1	0.05
t_{m2}	2.44 ms	3.00 ms	4.01 ms

In sum, based on the results in Table C.1-C.2, we confirm that by using Equation (C.7) and Equation (C.8) to estimate the time parameter t_{m1} and t_{m2} for δV_{ax} have robust results.

C.3 Approximation of transmembrane currents

After the axon stop firing, we assume that voltage-gated Na^+ and K^+ channel's conductance on axon membrane have returned to their resting state in the stimulated region,

$$g_{ax}^{i,dy} \approx g_{ax}^{i,re},\ i = \mathrm{Na}^+, \mathrm{K}^+.$$

At this stage, we have ion channel conductance on the glial and axon membrane as

$$\{g_{ax}^{Na,re},\ g_{ax}^{K,re},\ g_{ax}^{Cl},\ g_{gl}^{Cl},\ g_{gl}^{Na}\} \subset o\left(g_{gl}^{K}\right). \tag{C.9}$$

Similar to Equation (4.19), we claim in the stimulated region

$$\delta E_k^i = o\left(\delta E_{gl}^K\right), \quad i = \mathrm{Na}^+, \mathrm{Cl}^-, \quad k = gl, ax, \tag{C.10}$$

since Equation (4.24) and

$$c_{ex}^{K,re} = o\left(c_{ex}^{i,re}\right), \quad i = \mathrm{Na}^+, \mathrm{Cl}^-.$$

In addition, for the increase current through Na/K pump in Equation (4.20), we have

$$z^{Na}e\delta J^{Na}_{p,k} + z^{K}e\delta J^{K}_{p,k} = \delta I_k, \quad k = gl, ax.$$

By the Taylor expansion, we approximate the increase current through the Na/K pump due to the extracellular K^+ concentration changes as

$$\delta I_k \approx 2\left(\frac{K_{K1}I^{re,1}_k}{c^{K,re}_{ex}(c^{K,re}_{ex}+K_{K1})} + \frac{K_{K2}I^{re,2}_k}{c^{K,re}_{ex}(c^{K,re}_{ex}+K_{K2})}\right)\delta c^K_{ex}, \tag{C.11}$$

where $I^{re,1}_k$ and $I^{re,2}_k$ are the resting state current through α_1- and α_2- isoform of the Na/K pump on glial membrane ($k = gl$) or axon membrane ($k = ax$).
By comparison between Equation (4.19) and Equation (C.11), we have

$$\delta I_k = o\left(g^K_{gl}\delta E^K_{gl}\right), \qquad k = gl, ax. \tag{C.12}$$

In all, based on the estimations in (C.9), (C.10) and (C.12), we claim the dominated term in the right-hand side of Equation (4.20) is

$$\sum_i z^i e\mathcal{M}_{gl}\left(J^i_{p,gl} + J^i_{c,gl}\right) + \sum_i z^i e\mathcal{M}_{ax}\left(J^i_{p,ax} + J^i_{c,ax}\right) \approx \mathcal{M}_{gl}g^K_{gl}\left(\delta V_{gl} - \delta E^K_{gl}\right),$$

where we use the fact that at the resting state, the transmembrane currents in both axon membrane and glial membrane are negligible in compare to the source term $g^K_{gl}\delta E^K_{gl}$.

C.4 Comparison between $\delta\phi_{gl}$ and $\delta\phi_{ex}$

In this section, we show that the scale of the glial electric potential variation $\delta\phi_{gl}$ is much larger than the scale of the extracellular electric variation $\delta\phi_{ex}$ in the stimulated region. Based on Equation (4.30), we know

$$O\left(\frac{\eta_{gl}\sigma_{gl}}{\eta_{ex}\sigma_{ex}}\right) = 10^{-2}, \qquad O\left(\frac{\tau_{ex}eD^{\text{diff}}_{ex}}{\sigma_{ex}}\delta c_{sti}\right) = 10^{-6}. \tag{C.13}$$

If the $\delta\phi_{ex} \neq o(\delta\phi_{gl})$, then based on Equation (4.30) and (C.13), we should have

$$O\left(\delta\phi_{gl}\right) < 10^{-5}.$$

Therefore, the right-hand side of Equation (4.29) becomes

$$\left|\frac{g^K_{gl}}{e}\left(\delta V_{gl} - \delta E^K_{gl}\right)\right| \approx \left|\frac{g^K_{gl}}{e}\delta E^K_{gl}\right| = O\left(10^{-8}\right). \tag{C.14}$$

where we use the estimation of δE^K_{gl} $(= O\left(10^{-3}\right))$ in Equations (4.19) and (4.17), and

$$O\left(\delta V_{gl}\right) = O\left(\delta\phi_{gl} - \delta\phi_{ex}\right) < 10^{-5}.$$

At the same time, the left-hand side of Equation (4.29) gives

$$\left| \frac{2}{r_{sti}} \frac{\eta_{gl}\sigma_{gl}}{\mathcal{M}_{gl}} \frac{\delta\phi_{gl}}{r^*} \right| < O\left(10^{-11}\right). \tag{C.15}$$

In Equation (4.29), based on Equations (C.15) and (C.14), the order of right-hand side does not match with the order of left-hand side. Therefore, we claim that

$$\delta\phi_{ex} = o(\delta\phi_{gl}).$$

C.5 Estimation of extracellular Na^+ and K^+ transport

For the K^+ clearance in the stimulated extracellular region in Equation (4.39), based on Equations (4.19) and (4.34), the effect of average glial transmembrane K^+ flux in the stimulated region is

$$\lambda_{gl}^{m,K} = \frac{\mathcal{M}_{gl} g_{gl}^K h_\epsilon k_B T}{z^K \left(1 + h_\epsilon\right) e^2 c_{ex}^{K,re}}. \tag{C.16}$$

For K^+ flux through the extracellular pathway, we only consider the effects from diffusion and electric drift terms in the radial K^+ flux. The effect of convection flux in the extracellular space is a cumulative result due to osmotic pressure $k_B T \delta O_{ex}$. The fluid flows in the extracellular space from the non-stimulated region to the stimulated region dominated by the glial transmembrane water flow. So, the convection flux in the extracellular is a consequence of the osmosis and flattens the variation of osmotic pressure in the stimulated region.

The scale of the radial diffusive K^+ flux in the extracellular space can be approximated as

$$O\left(-D_{ex}^K \tau_{ex} \frac{dc_{ex}^K}{dr}\right) = \frac{D_{ex}^K \tau_{ex}}{r^*} \delta c_{ex}^K. \tag{C.17}$$

The scale of the radial electric drift K^+ flux in the extracellular space is

$$\begin{aligned} O\left(-\frac{D_{ex}^K \tau_{ex} e}{k_B T} c_{ex}^K \frac{d\phi_{ex}}{dr}\right) &= \frac{D_{ex}^K \tau_{ex} e}{k_B T} c_{ex}^K \frac{\delta\phi_{ex}}{r^*} \\ &\approx -\frac{\eta_{gl}\sigma_{gl} D_{ex}^K \tau_{ex}}{\eta_{ex}\sigma_{ex}\left(1 + h_\epsilon\right) r^*} \delta c_{ex}^K, \end{aligned} \tag{C.18}$$

where $\delta\phi_{ex}$ used the estimation from Equation (4.35).
Based on Equations (C.17) and (C.18), we note that the electric drift K^+ flux is in the opposite radial direction to the diffusive K^+ flux in the extracellular space. At the same time, the electric drift K^+ flux has a much smaller magnitude than the diffusive K^+ flux because the ratio R_{ex}^K between the electric drift and diffusion term is

$$R_{ex}^K = \frac{\eta_{gl}\sigma_{gl}}{\eta_{ex}\sigma_{ex}(1 + h_\epsilon)} = o(1). \tag{C.19}$$

Therefore, in Equation (4.39), the average effect of the K^+ transport through extracellular pathway can be approximated as

$$\lambda_{ex}^{K} = \frac{2\eta_{ex} D_{ex}^{K} \tau_{ex}}{r_{sti} r^*}, \tag{C.20}$$

where we used the ratio between volume V_S and the effective radial surface.

In Equation (4.40), we first look for the effect of Na^+ fluxes through the extracellular pathway. Similar to Equation (C.17), the scale of the radial diffusive Na^+ flux in the extracellular space is

$$O\left(-D_{ex}^{Na}\tau_{ex}\frac{dc_{ex}^{Na}}{dr}\right) = \frac{D_{ex}^{Na}\tau_{ex}}{r^*}\delta c_{ex}^{Na}. \tag{C.21}$$

The scale of the radial electric drift flux for Na^+ in in the extracellular space is

$$\begin{aligned} O\left(-\frac{D_{ex}^{Na}\tau_{ex}e}{k_B T}c_{ex}^{Na}\frac{d\phi_{ex}}{dr}\right) &= \frac{D_{ex}^{Na}\tau_{ex}e}{k_B T}c_{ex}^{Na}\frac{\delta\phi_{ex}}{r^*} \\ &\approx -\frac{\eta_{gl}\sigma_{gl}D_{ex}^{Na}\tau_{ex}}{\eta_{ex}\sigma_{ex}\left(1+h_\epsilon\right)r^*}\frac{c_{ex}^{Na,re}}{c_{ex}^{K,re}}\delta c_{ex}^{K} \end{aligned} \tag{C.22}$$

where we use the resting state concentration ratio $\frac{c_{ex}^{Na,re}}{c_{ex}^{K,re}}$ for the approximation. For Na^+ in the extracellular space, the radial electric drift Na^+ flux is in the same direction as the radial diffusive K^+ flux since δc_{ex}^{Na} is negative in the stimulated region.
The scale of the radial diffusive Na^+ flux is at same level as the radial electric drift Na^+ flux in the extracellular space. From Equations (C.21) and (C.22), the ratio R_{ex}^{Na} is

$$R_{ex}^{Na} = \frac{\eta_{gl}\sigma_{gl}}{\eta_{ex}\sigma_{ex}\left(1+h_\epsilon\right)}\frac{c_{ex}^{Na,re}}{c_{ex}^{K,re}} = O(1), \tag{C.23}$$

since δc_{ex}^{Na} and δc_{ex}^{K} is at the same level as the estimation before. The Na^+ flux through glial transmembrane is much smaller than the K^+ flux through glial transmembrane in the stimulated region

$$\lambda_{gl}^{m,Na} = o\left(\lambda_{gl}^{m,K}\right). \tag{C.24}$$

This is because the conductance on the glial membrane $g_{gl}^{Na} = o\left(g_{gl}^{K}\right)$. The effect of Na^+ flux through glial transmembrane can be neglected in Equation (4.40), since Equation (C.24), and the diffusive fluxes in Equations (C.21) and (C.17) are in the same magnitude. In sum, for Equation (4.40), we get

$$\lambda_{ex}^{Na,1} = \frac{2\eta_{ex}D_{ex}^{Na}\tau_{ex}}{r_{sti}r^*}, \quad \lambda_{ex}^{Na,2} = \frac{2\eta_{gl}\sigma_{gl}D_{ex}^{Na}\tau_{ex}c_{ex}^{Na,re}}{r_{sti}\sigma_{ex}\left(1+h_\epsilon\right)r^* c_{ex}^{K,re}}.$$

where we used the ratio between volume V_S and the effective radial surface.

In the end of this section, we consider the solution for the coupled dynamical system of (4.39) and (4.40)

$$\frac{d}{dt}\begin{pmatrix}\delta c_{ex}^{K}\\ \delta c_{ex}^{Na}\end{pmatrix} = A\begin{pmatrix}\delta c_{ex}^{K}\\ \delta c_{ex}^{Na}\end{pmatrix}, \tag{C.25}$$

where

$$A = \begin{bmatrix} A_{11} & 0\\ A_{21} & A_{22}\end{bmatrix} = \begin{bmatrix} -\left(\lambda_{gl}^{m,K}+\lambda_{ex}^{K}\right)/\eta_{ex}^{re} & 0\\ \lambda_{ex}^{Na,2}/\eta_{ex}^{re} & -\lambda_{ex}^{Na,1}/\eta_{ex}^{re}\end{bmatrix}. \tag{C.26}$$

In the system (C.25), we assume that η_{ex} keeps at its resting state (η_{ex}^{re}) and the initial condition is

$$\begin{pmatrix}\delta c_{ex}^{K,0}\\ \delta c_{ex}^{Na,0}\end{pmatrix} = \begin{pmatrix}\delta c_{sti}\\ -\delta c_{sti}\end{pmatrix}. \tag{C.27}$$

The solution for System (C.25) in the time interval $t \in [0, T]$ is

$$\begin{cases}\delta c_{ex}^{K}(t) = \delta c_{sti}\exp\left(A_{11}t\right),\\ \delta c_{ex}^{Na}(t) = \dfrac{A_{21}\delta c_{sti}}{A_{11}-A_{22}}\left(\exp\left(A_{11}t\right)-\exp\left(A_{22}t\right)\right) - \delta c_{sti}\exp\left(A_{22}t\right),\end{cases} \tag{C.28}$$

where T is the time interval between each single action potential in the axon compartment. There are n ($= \frac{T_{sti}}{f_m}$) stimuli in the time interval $[0, T_{sti} = nT]$, we have

$$\delta c_{ex}^{K}(iT) = \delta c_{ex}^{K}(iT) + \delta c_{sti},\quad \delta c_{ex}^{Na}(iT) = \delta c_{ex}^{Na}(iT) - \delta c_{sti},\quad i = 1\ldots n-1,$$

In the above, we view the extracellular K^+ and Na^+ concentration immediately changes due to axon firing. By using Equation (C.28), we have

$$\delta c_{ex}^{K}(nT) = \delta c_{sti}\frac{\exp\left(A_{11}T\right)-\exp\left((n+1)A_{11}T\right)}{1-\exp\left(A_{11}T\right)}, \tag{C.29}$$

and

$$\begin{aligned}\delta c_{ex}^{Na}(nT) =& \sum_{i=1}^{n}\frac{A_{21}\delta c_{ex}^{K}((i-1)T)}{4}\left(\exp\left(A_{11}T\right)-\exp\left(A_{22}T\right)\right)\exp\left((n-i)A_{22}T\right)\\ &- \delta c_{sti}\sum_{i=1}^{n}\exp\left(iA_{22}T\right),\end{aligned} \tag{C.30}$$

where

$$\delta c_{ex}^{K}(jT) = \delta c_{sti}\frac{1-\exp\left((j+1)A_{11}T\right)}{1-\exp\left(A_{11}T\right)},\quad j = 0, 1, \ldots n-1.$$

C.6 Spatial Distribution of velocity and osmotic pressure

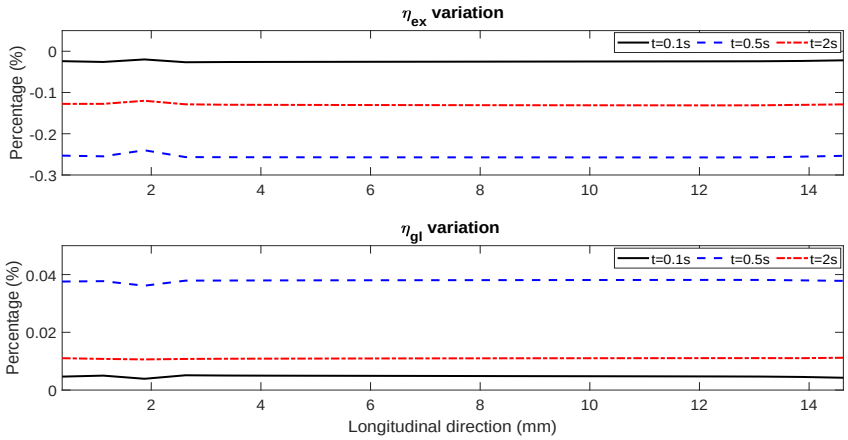

Figure C.1: Longitudinal direction changes of η_{ex} and η_{gl} at $r = 1.5\mu$m $t = 0.1$s, 0.5s, 2s.

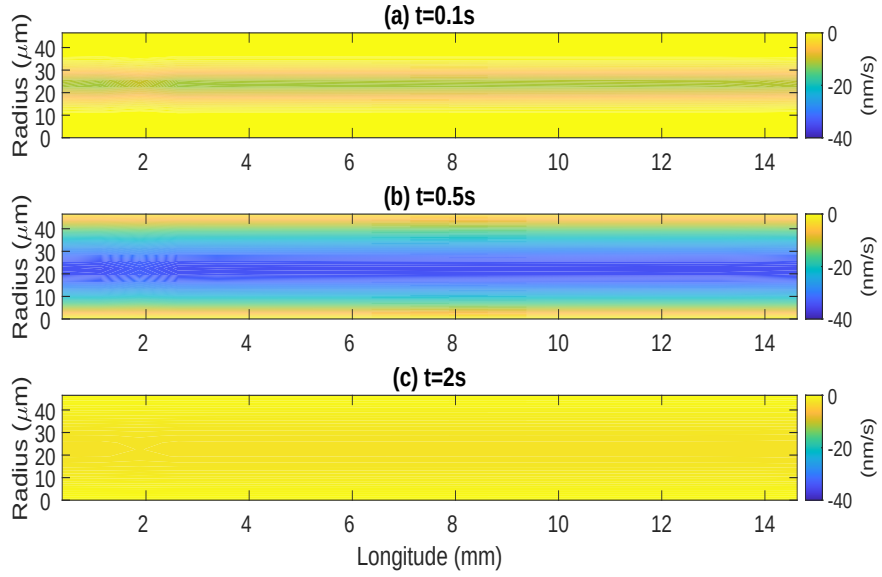

Figure C.2: Spatial distribution of velocity in radius direction during and after a train of stimuli.

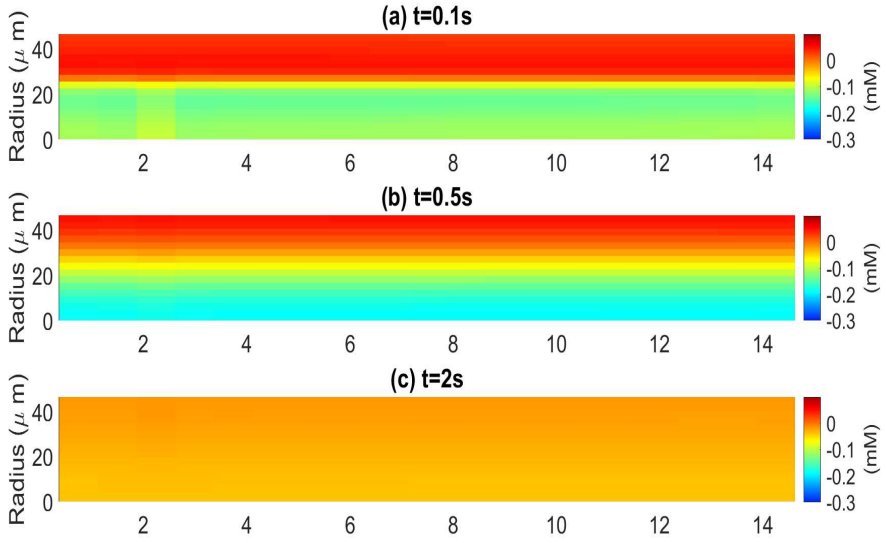

Figure C.3: Spatial distribution of osmotic pressure changes from resting state during and after a train of stimuli.

Appendix D

Supporting information for optic nerve model

D.1 Convergence rate test

In this section, we conduct the convergence test by using the uniform mesh, namely we use the mesh size $N_x = N_y = N$. The Cauchy error [92] is used to test the convergence rate. In this test method, error between two different spacial mesh sizes h and $\frac{h}{2}$ is calculated by $||e_\zeta|| = ||\zeta_h - \zeta_{\frac{h}{2}}||$, where ζ is the function to be solved. The mesh sizes are set to be $h = 1/10, 1/20, 1/40, 1/80$ and time step is fixed as $\delta t = 10^{-4}$.

Testing on Ion Equations and Hydrostatic Pressure Equations

The ion's governing equations (3.9) are in the form of NernstPlanck equation. To test uncoupled ion equations $c_l^i, i = \mathrm{Na}^+, \mathrm{K}^+, l = ax, gl, ex$ respectively, we set the initial condition as

$$c_l^i = c_l^{i,re} + 5\sin(\pi r)\sin(\pi z), i = \mathrm{Na}^+, \mathrm{K}^+, l = ax, gl, ex.$$

The L^∞ numerical errors and convergence rate at chosen time $t = 0.1$s are displayed in Table (D.1),

Table D.1: The discrete L^∞ error and convergence rate for ion

Grid Size	ER(c_{ax}^{Na})	Rate	ER(c_{ax}^{K})	Rate	ER(c_{gl}^{Na})	Rate	ER(c_{gl}^{K})	Rate	ER(c_{ex}^{Na})	Rate	ER(c_{ex}^{K})	Rate
10×10	2.63e-4	-	2.63e-4	-	4.89e-4	-	3.35e-4	-	8.70e-4	-	1.11e-4	-
20×20	6.72e-5	1.97	6.72e-5	1.97	1.25e-4	1.98	8.54e-5	1.97	2.41e-4	1.85	2.93e-5	1.93
40×40	1.68e-5	1.99	1.69e-5	1.99	3.13e-5	1.99	2.14e-5	1.99	6.05e-5	1.99	7.38e-6	1.99
80×80	4.22e-6	2.00	4.23e-6	2.00	7.32e-6	2.00	5.37e-6	2.00	1.51e-5	2.00	1.85e-6	2.00

For the pressure's equation (3.2), the following initial condition are set.

$$p_{ex} = p_{ex}^{re} + 5\sin(\pi r)\sin(\pi z).$$

The L^∞ numerical errors and convergence rate are displayed in the Table (D.2)

Table D.2: The discrete L^∞ error and convergence rate for hydrostatic pressure

Grid Size	ER(p_{ax})	Rate	ER(p_{gl})	Rate	ER(p_{ex})	Rate
10×10	9.84e-6	-	1.07e-5	-	1.05e-5	-
20×20	2.28e-6	2.11	2.74e-6	1.97	2.71e-6	1.97
40×40	5.62e-7	2.02	6.86e-7	2.00	6.83e-7	1.99
80×80	1.40e-7	2.00	1.72e-7	2.00	1.71e-7	1.99

D.2 Randomly stimulated cases

In this section, we provide the K^+ decay time comparison between spatially uniform radial (inner and outer) cases and spatially randomly stimulated cases in Table D.3 below. The stimulated volume ratio presents the fraction of stimulated region volume over total region volume. We calculate how much time it takes in each case for the K^+ concentration in the stimulated extracellular region to decay the certain percentage (50%, 70%, and 90%) from its maximum value.

Table D.3: Potassium Decay Time

	Stimulated Volume Ratio	50% decay	70% decay	90% decay
Inner case	0.25	0.2 s	1.0 s	4.5 s
Outer case	0.75	1.7 s	3.4 s	7.5 s
Random case 1	0.55	2.0 s	3.6 s	7.8 s
Random case 2	0.30	1.5 s	3.1 s	6.9 s
Random case 3	0.73	2.0 s	3.7 s	7.9 s
Random case 4	0.70	2.0 s	3.7 s	7.6 s

In Figure D.1-D.3, we present the K^+ fluxes through M_S, E_T, M_{NS} and G_T in spatially randomly stimulated cases. It shows a similar pattern of periodic oscillation of the K^+ flux during a train of stimuli, and the oscillation magnitude is larger than the inner stimulated one.

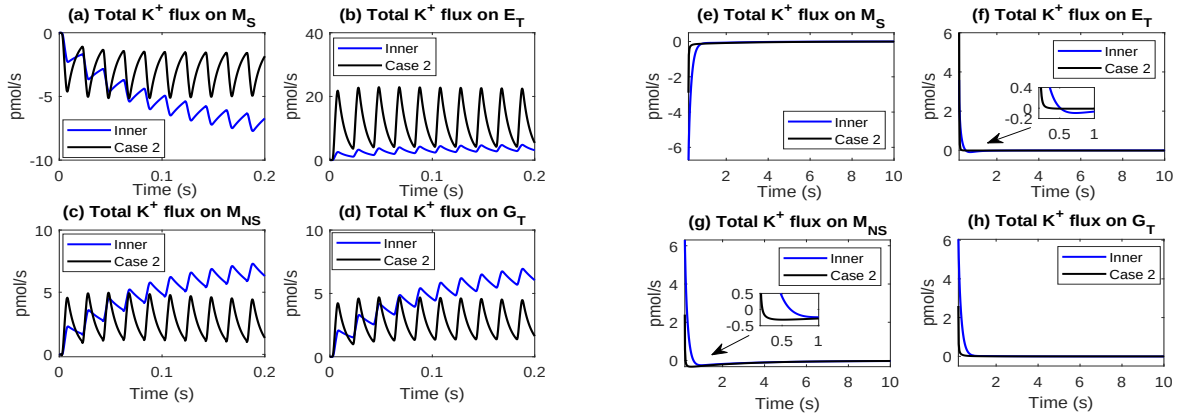

Figure D.1: Comparison between spatially randomly stimulated case 2 with the spatially uniform (inner) case.

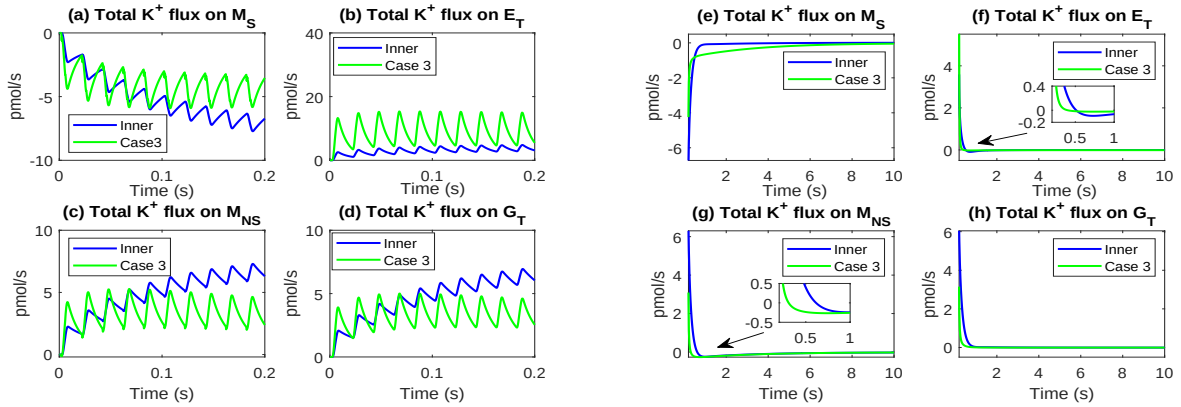

Figure D.2: Comparison between spatially randomly stimulated case 3 with the spatially uniform (inner) case.

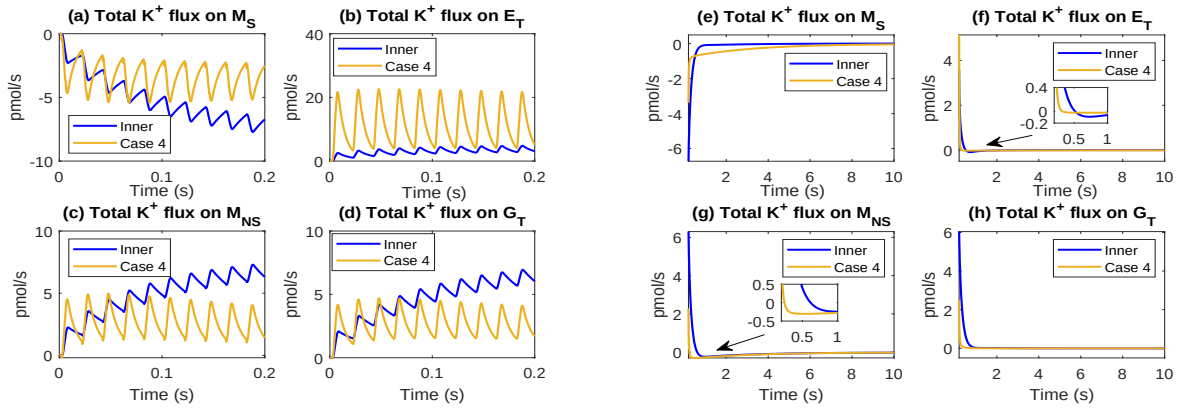

Figure D.3: Comparison between spatially randomly stimulated case 4 with the spatially uniform (inner) case.

D.3 NKCC parameters

Table D.4 below shows parameters on the glial membrane when the NKCC channel is introduced. For each case, we keep K^+ and Na^+ concentrations and electric potentials in the glial compartment and the extracellular space are the same at the resting state.

Table D.4: NKCC Parameters

	$I_{\max}^{NKCC}$	g_{gl}^{K}	g_{gl}^{Na}	$I_{gl,1}$	A_{gl}
Baseline	0 A/m^2	2.1 S/m^2	2.2×10^{-3} S/m^2	4.78×10^{-4} A/m^2	105mM
NKCCa	2×10^{-3} A/m^2	2.88 S/m^2	1.65×10^{-3} S/m^2	4.78×10^{-4} A/m^2	34.7mM
NKCCb	2×10^{-3} A/m^2	2.1 S/m^2	8.36×10^{-4} S/m^2	2.49×10^{-4} A/m^2	34.7mM

In Table D.5, we provide the K^+ concentration decay time in the stimulated extracellular region under models with/without NKCC. It shows that the model with NKCC on the glial membrane produces a faster decay of the K^+ concentration in the stimulated extracellular region.

Table D.5: Potassium Concentration Decay Time with/without NKCC

	50% decay	70% decay	90% decay
Baseline	1.95 s	3.58 s	7.83 s
NKCCa	0.60 s	1.11 s	2.41 s
NKCCb	0.63 s	1.17 s	2.66 s

D.4 Parameters in optic nerve model

Parameters	Value	Parameters	Value
R_a	4.8×10^{-5} m (Ref.[13, 93])	μ	7×10^{-4} Pa $\cdot$ s (Ref.[3])
R_b	6×10^{-5}m (Ref.[75])	$c^{Na}_{csf,eye}$	111 mM (Ref.[13])
L	1.5×10^{-2} m (Ref.[13])	$c^{\mathrm{K}}_{\mathrm{csf,eye}}$	3 mM (Ref.[13])
e	1.69×10^{-19} A $\cdot$ s	$c^{\mathrm{Na,re}}_{gl}$	7.57 mM (*)
k_B	1.38×10^{-23} J/K	$c^{K,re}_{gl}$	100.84 mM (*,Ref.[13])
T	296.15 K (Ref.[13])	$c^{\mathrm{Na,re}}_{ax}$	10.17 mM (*)
η^{re}_{ax}	5×10^{-1} (Ref.[13])	$c^{K,re}_{ax}$	100.04 mM (*)
η^{re}_{gl}	4×10^{-1} (Ref.[13])	$A^{re}_{ax,gl}$	105 mM (*)
η^{re}_{ex}	1×10^{-1} (Ref.[13])	τ^{OP}_{ex}	0.16 (Ref.[3, 31])
$\mathcal{M}_{ax}$	5.9×10^{6} m^{-1} (Ref.[94])	τ^{SAS}_{ex}	1 (*)
$\mathcal{M}_{gl}$	1.25×10^{7} m^{-1} (Ref.[94])	τ_{gl}	0.5 (*)
$z^{Na,K}$	1	p_{CSF}	1.3×10^{3} Pa (Ref.[46])
z^{Cl}	-1	p_{ICP}	4×10^{3} Pa (Ref.[46])
$z^{ax,gl}$	-1 (*)	p_{OBP}	0 Pa (Ref.[46])
$\gamma_{\mathrm{ax,gl}}$	1 (Ref.[3, 31])	$D^{Na}_{ex,ax}$	1.39×10^{-9} m^2/s (Ref.[3])
γ_{pia}	1 (Ref.[3, 31])	$D^{K}_{ex,ax}$	2.04×10^{-9} m^2/s (Ref.[3])
$K_{\mathrm{Na1,Na2}}$	2.3393mM (Ref.[58])	$D^{Cl}_{ex,ax}$	2.12×10^{-9} m^2/s (Ref.[3])
K_{K1}	1.6154mM (Ref.[58])	D^{Na}_{gl}	1.39×10^{-11} m^2/s (Ref.[3])
K_{K2}	0.1657mM (Ref.[58])	D^{K}_{gl}	2.04×10^{-11} m^2/s (Ref.[3])
$I_{gl,1}$	4.78×10^{-4} A/m^2 (**,Ref.[58])	D^{Cl}_{gl}	2.12×10^{-11} m^2/s (Ref.[3])
$I_{gl,2}$	6.5×10^{-5} A/m^2 (**,Ref.[58])	k^{OP}_{ex}	1.3729×10^{-8} m^2/ $\cdot$ s (Ref.[31])
$I_{ax,1}$	9.56×10^{-4} A/m^2 (**,Ref.[58])	k^{SAS}_{ex}	0 m^2/V $\cdot$ s (*)
$I_{ax,2}$	1.3×10^{-4} A/m^2 (**,Ref.[58])	K_{ax}	1.67×10^{6} Pa (Ref.[17, 95])
g^{Na}_{gl}	2.2×10^{-3} S/m^2 (Ref.[3])	K_{gl}	8.33×10^{5} Pa (Ref.[17, 95])
g^{K}_{gl}	2.1 S/m^2 (Ref.[3])	L^{m}_{dr}	8.89×10^{-13} m/Pa $\cdot$ s (Ref.[31, 58])
g^{Cl}_{gl}	2.2×10^{-3} S/m^2 (Ref.[3])	L^{m}_{pia}	8.89×10^{-13} m/Pa $\cdot$ s (Ref.[31, 58])
g^{Na}_{leak}	4.8×10^{-3} S/m^2 (**,Ref.[66])	L^{m}_{gl}	1.34×10^{-13} m/Pa $\cdot$ s (Ref.[31, 58])
g^{K}_{leak}	2.2×10^{-2} S/m^2 (**,Ref.[66])	L^{m}_{ax}	7.954×10^{-14} m/Pa $\cdot$ s (Ref.[96])
$\bar{g}^{Na}$	1.357×10^{1} S/m^2 (**,Ref.[66])	κ_{gl}	9.366×10^{-19} m^2 (Ref.[31, 58])
$\bar{g}^{K}$	2.945 S/m^2 (**,Ref.[66])	κ_{ax}	1.33×10^{-16} m^2 (Ref.[31, 58])
g^{Cl}_{ax}	1.5×10^{-1} S/m^2 (*)	κ^{OP}_{ex}	3.99×10^{-16} m^2 (**,Ref.[31, 58])
$G^{Na,K,Cl}_{pia}$	3 S/m^2 (*)	κ^{SAS}_{ex}	1.33×10^{-14} m^2 (**,Ref.[31, 58])

Note: the '*' estimated or induced from the concentration balance.
Note: the '**' deducted proportional from reference.